On the prediction of three-phase relative permeabilities using two-phase constitutive relationships

Gerhard Schafer, Raphael Di Chiara Roupert, Amir H. Alizadeh, Mohammad Piri

Version of Record: https://www.sciencedirect.com/science/article/pii/S0309170820302037
Manuscript_7c6420122e38657cfb54c9fc36487f69

On the prediction of three-phase relative permeabilities using two-phase constitutive relationships

Gerhard Schäfer[1], Raphaël di Chiara Roupert[1], Amir H. Alizadeh[2], Mohammad Piri[3]

[1] Université de Strasbourg, CNRS, LHyGeS UMR 7517, Strasbourg, France.
[2] Nalco Champion, an Ecolab Company, Sugar Land, Texas, USA.
[3] Center of Innovation for Flow through Porous Media, Department of Petroleum Engineering, University of Wyoming, Laramie, Wyoming, USA.

Abstract

The predictions of two recent and two classical mathematical models are compared with experimentally measured three-phase relative permeabilities. Experimentally determined constitutive relationships in two-phase systems were used as model input parameters to numerically predict relative permeabilities (k_r) in three-phase systems. Then the estimated results were compared with experimental three-phase permeabilities measured along decreasing water saturation/decreasing oil saturation/increasing gas saturation (DDI) paths. The results of the individual models to each of the three fluids involved (water, oil, and gas) were analyzed in detail. The simulated results showed that the Total Differential (TD) compatible model overestimates significantly both the global mobilities as well as the relative phase permeabilities in the three-phase system. There was improvement in the prediction with the TD compatible model when experimental data were used to locally impose the global mobility and fractional water and gas fluxes in the ternary diagram. Globally, the best prediction of the measured k_r values was obtained with the so-called mechanistic model. However, its numerical implementation requires a preliminary calibration of the relative phase permeabilities in a three-phase system against experimental data along one DDI path to quantify the required six characteristic coefficients. In contrast to the TD compatible model, which by construction does not exhibit any numerical instabilities, elliptic zones in the water-oil (NAPL)-gas ternary diagram were identified in the mechanistic model.

Keywords:
relative permeability; three-phase system; mathematical model; global mobility; ternary diagram

1. Introduction

Since the 1950s, the number of sites contaminated by halogenated solvents has increased significantly in industrialized countries. Solvents are used in a wide range of industrial processes and in everyday products (e.g. paints, oils, varnishes, and dry cleaning liquids) and may be released into the environment in industrial effluents or by improper disposal by users. Among all solvents, aliphatic chlorinated solvents (including chloromethane, chloroethane, and chloroethene) have been the most frequently encountered group of compounds. Therefore, characterization and modeling of the fate of chlorinated solvents in porous aquifers has gained significant attention in recent years to protect groundwater resources (Fried et al., 1979; Cohen and Mercer, 1993; Pankow and Cherry, 1996; Jellali et al., 2001; Bohy et al., 2006; Dridi et al., 2009; Cotel et al., 2011, Portois et al., 2018; Qian et al., 2020). These liquid compounds are immiscible in water, and because they are usually denser than water (except vinyl chloride, chloromethane, and chloroethane), they are called dense nonaqueous phase liquids (DNAPL). In the subsurface, chlorinated solvents migrate vertically depending on the gravity and capillary forces through the unsaturated zone, where a large vapour plume appears due to their high volatility. After rainfall, a vapour lixiviation due to vapour precipitation may occur and dissolved chlorinated solvents can reach the groundwater table and contaminate the groundwater (Mendoza and Frind, 1990; Sleep and Sykes, 1992; Jellali et al., 2003). If the amount of solvents released is large, the DNAPL reaches and penetrates the groundwater table due to its high density, dissolves and forms a solute plume. Within the aquifer, a certain amount of solvents becomes trapped as blobs or forms pools over low permeability geological structures. This constitutes a long-term source of contamination of drinkable groundwater

resources, given the low solubilities of the solvents (Schwille, 1988; Brusseau, 1992; Kennedy and Lennox, 1997; Eberhardt and Grathwohl, 2002, Seyedabbasi et al., 2012).

Multiphase flow may occur in a porous aquifer in the form of three-phase water-NAPL-gas flow in the unsaturated zone and two-phase water-NAPL flow in the saturated zone (Fig. 1). Gravity-driven infiltration of NAPLs in soil containing one or more chlorinated solvents leaves behind a zone of residual saturation. This process results in a small size NAPL source zone within the porous medium with respect to the characteristic dimensions of the aquifer.

The main difference between the two- and three-phase flow is the formation of NAPL layers sandwiched between gas and water (Blunt et al., 1995) and the double displacement where the gas displaces the disconnected NAPL ganglia which displaces water (Øren and Pinczewski, 1995). These mechanisms can reduce residual NAPL saturation, even in capillary-dominated flow (Helland and Jettestuen, 2016), whereas in two-phase capillary-dominated flow, isolated ganglia are trapped (Chatzis and Morrow, 1984).

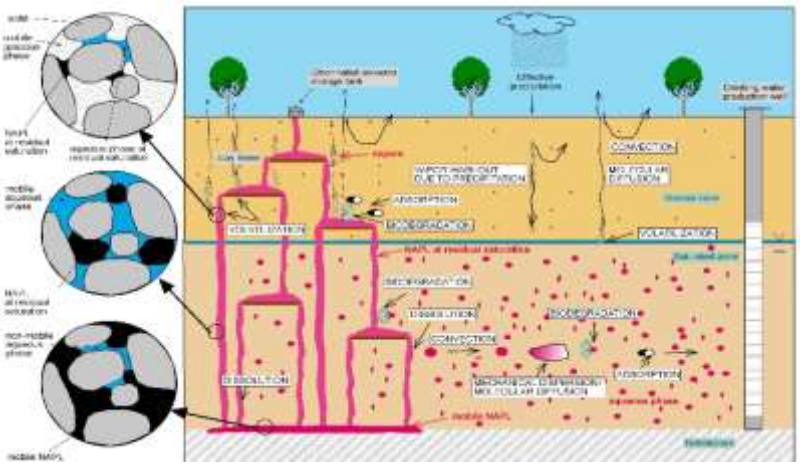

Fig. 1. Physico-chemical processes involved in the fate of chlorinated solvents in the subsurface (Côme et al., 2008).

Numerical simulation of multiphase flow has become a crucial method for solving water-resource management and other environmental problems such as CO_2 sequestration in saline aquifers and coupled geomechanical processes in the subsurface (Helmig et al., 2013; Celia et al., 2015; Benisch et al., 2020). While multiphase flow models for water, NAPL, and gas phases were initially adopted in petroleum research for reservoir simulation, they were later successfully exploited for hydrosystem monitoring or remediation. Pressure and saturation of fluids are the key variables in the analysis of multiphase flow in porous media. Furthermore, secondary variables such as relative permeabilities and capillary pressures, which are functions of fluid saturations, are needed for the simulation of displacement processes in porous media.

Forecasting the behavior of chlorinated solvents in aquifers presents at least two difficulties: characterization of the source zone (i.e., locating the source zone and evaluating the NAPL volume and composition) and modeling of the fate of pollution downstream of the source zone (i.e., how to choose physical models, mathematical tools, and numerical methods). Multiphase flow modeling is a major tool for assessing groundwater pollution caused by non-aqueous phase liquids (NAPL), such as chlorinated solvents. To quantify and characterize groundwater pollution by NAPLs, numerical codes that include multicomponent transport equations require a fast and accurate resolution of the primary and secondary variables of three-phase flow.

The relative permeability of a fluid depends on the wetting properties of the porous medium (van Dijke and Sorbie, 2002), but it may also depend on the saturation history, as the pore-scale fluid configurations are history-dependent. Relative permeability can be measured either in the laboratory by performing coreflood experiments or estimated using empirical correlations. The earliest three-phase relative permeability measurements found in the literature date back to the work of Leverett and Lewis (1941), and since then, a variety of studies have been conducted to investigate the effects of various parameters, such as saturation history, wettability, spreading, and layer drainage, on three-phase relative permeability (Alizadeh and Piri, 2014a). Nonetheless, experimental measurement of three-phase relative permeabilities is far more complex and time-consuming than two-phase relative permeabilities, and thus several correlations and mathematical

models have been proposed over the years to predict three-phase relative permeabilities using two-phase relative permeability data (e.g., Corey et al., 1956; Stone, 1970, 1973; Baker, 1988; Delshad and Pope, 1989; Blunt et al., 1995; Blunt, 2000; Ranaee et al., 2015; Shahverdi and Sohrabi, 2017). A detailed review of existing three-phase relative permeability models is given by Shahverdi and Sohrabi (2017).

The present study addresses, from both physical and numerical points of view, specific questions related to mathematical modeling of three-phase multiphase flow in porous media. As regards the physical aspect, the research questions relate directly to the use and implementation of three-phase (water, NAPL, gas) flow codes to predict, for example, the formation of a NAPL source zone after infiltration of NAPLs into the subsurface. These numerical tools require as input parameters, inter alia, constitutive relationships, such as relative permeabilities, which are functions of saturations of different fluids present in the porous medium. In connection with the implementation of relative permeabilities in numerical three-phase flow codes, model developers and users are faced with a range of basic questions: how is one able to predict the relative permeability of the NAPL phase as a function of water and gas saturation levels? Are the relative permeability models that have traditionally been developed for NAPLs, such as Stone models (Stone, 1970; Stone, 1973), appropriate for representing the governing displacement physics, and if not, what are the shortcomings?

Regarding the numerical aspect, the questions that arise for modelers are often related to the possible instability of numerical models. Relative permeability models for the NAPL phase in three-phase flow systems can be the origin of numerical instabilities (Trangenstein, 1989). While conventionally assumed that three-phase permeability models only generate hyperbolic systems, Bell et al. (1986) using synthetic k_r models showed that the system of saturation equations is not purely hyperbolic in all respects and may produce unstable results for certain saturation values called elliptic regions. Jahanbakhshi et al. (2013) demonstrated by linearization that the system is unstable in elliptic regions, i.e., for conjugate complex eigenvalues of the Jacobian matrix of the system of two saturation equations using the fractional flow theory of displacement. For example, using Stone's Model I (Stone, 1970), in cases of flow configurations that do not include gravity and capillary effects, the occurrence of elliptic zones leads to significant oscillations of fluid saturations (Schneider, 2015) and exhibits complex wave speeds that result in non-unique solutions (Jackson and Blunt, 2002).

In the absence of three-phase experimental data, a new class of Total Differential (TD) interpolations was designed to simplify the numerical simulations of compressible three-phase flows by using a global pressure formulation (Chavent et al., 2008; Chavent, 2009; Amaziane et al., 2012). This formulation requires that the three-phase relative permeabilities and capillary pressures satisfy the so-called Total Differential (TD) condition (Chavent, 2009) which guarantees the strict hyperbolicity of the reformulated system (Chavent, 1986). The TD-interpolation of a collection of three-phase data sets is then realized by constructing two functions over the ternary diagram, one global capillary pressure and one global mobility, which satisfy the boundary conditions determined by the three given two-phase data sets.

The resultant relative permeabilities that comply with the condition of Total Differential defined by di Chiara Roupert (2009) do not yield elliptic zones and will therefore be used in our comparison of the predictions of different mathematical models with experimentally tested three-phase relative permeability results. The TD compatible model described by di Chiara Roupert et al. (2010a) will be extended by integrating experimental based residual fluid saturations in two-phase systems. To compare the TD compatible model with the commonly used three-phase relative permeability models, we included three other models in our study. First, the recently developed model for the prediction of three-phase relative permeabilities, the so-called mechanistic model proposed by Shahverdi and Sohrabi (2017) will be evaluated. This model presumably takes into account the interaction between various fluids as well as fluid saturation distributions using an arithmetic averaging relationship between two-phase and three-phase permeabilities. Our numerical study will then be completed by applying the classical Parker-Lenhard model (Parker and Lenhard, 1990) that was traditionally introduced as one of the first permeability models in three-phase flow and transport numerical simulators to describe and predict the fate of contamination by NAPLs in the subsurface, and the historical Stone model I (Stone, 1970) commonly implemented in industrial oil reservoir codes will be used to model the oil relative permeability in three-phase systems.

In our numerical simulations, we used experimentally determined constitutive relationships of two-phase systems as input parameters to numerically predict the relative permeabilities in three-phase systems. Then we compared the estimated results with experimental three-phase permeabilities measured by Oak (Oak, 1990) and Alizadeh (Alizadeh, 2013; Alizadeh and Piri, 2014b) along decreasing water saturation/decreasing oil (NAPL) saturation/increasing gas saturation (DDI) paths. The overall objective of the present work was to quantify the differences between the measured and the predicted relative permeabilities for water, oil, and gas in a three-phase fluid system. The occurrence of elliptic regions is also analyzed for the mechanistic model, Parker-Lenhard model, and Stone's model I in the framework of the classical fractional flow theory of displacement.

Our study is organized as follows. Section 2 outlines the main features of the three-phase relative permeability models evaluated. The experimental data employed for the evaluation and comparison of the different mathematical models to describe relative permeabilities in three-phase flow systems are concisely described in Section 3. Key results of our numerical studies are presented in Section 4. Finally, Section 5 presents the outcome of our individual model analysis to each of the three fluids involved (water, oil, and gas) and discusses the existence and importance of elliptic zones in a water-oil (NAPL)-gas ternary diagram when using the mechanistic model.

2. Mathematical models

Here we describe the main features of two recent and two classical models evaluated against experimentally measured three-phase permeabilities:

- Mechanistic model of Shahverdi & Sohrabi (Shahverdi and Sohrabi, 2017)
- Total Differential compatible model introduced by di Chiara Roupert et al. (2010a, 2010b) – extended by integrating experimental based residual fluid saturations in two-phase systems
- Parker-Lenhard model (Parker and Lenhard, 1990)
- Stone's Model I (Stone, 1970)

The constitutive relationships (capillary pressure-saturation (pc-S) and relative permeability-saturation (k_r-S) functions) in two-phase systems used in our study are summarized in Appendix A.

2.1 Mechanistic model of Shahverdi & Sohrabi

To predict three-phase relative permeabilities of oil, water, and gas, the so-called mechanistic model proposed by Shahverdi and Sohrabi (2017) takes into account the interactions between the fluids and fluid saturation distributions. For this purpose, an arithmetic averaging relationship between two-phase and three-phase permeability is used. Six new parameters named characteristic coefficients, A_{ij}, (having a value between zero and one) are introduced in their model to express the linear relationship between two-phase and three-phase saturations for each of the three fluids present in the system. These coefficients reflect the contribution of each fluid in controlling the flow of the other fluids. It should be noted that at least one set of experimental three-phase relative permeability data (for one saturation path) is required to tune the characteristic coefficients. The estimated characteristic coefficients can then be employed to predict three-phase relative permeabilities for any other saturation path.

In this model, the three-phase relative permeability of the oil phase (k_{ro}) is expressed by

$$k_{ro} = \frac{S_{wo}}{S_{wo}+S_{go}} k_{row}(S_{ow}) + \frac{S_{go}}{S_{wo}+S_{go}} k_{rog}(S_{og}) \qquad (1)$$

where k_{row} is the two-phase oil relative permeability in the oil-water system, k_{rog} is the two-phase oil relative permeability in the gas-oil system, S_{ow} and S_{og} are the oil saturation in the two-phase oil-water and gas-oil system, and S_{wo} and S_{go} represent the water saturation in a two-phase water-oil system and gas saturation in the two-phase gas-oil system. The model proposes a linear relationship between two-phase and three-phase saturations as follows:

$$S_{ow} = A_{ow} S_o \,, \qquad (1a)$$
$$S_{og} = A_{og} S_o \,, \qquad (1b)$$
$$S_{wo} = A_{wo} S_w \,, \qquad (1c)$$
$$S_{go} = A_{go} S_g \,, \qquad (1d)$$

where S_w, S_o, and S_g are the three-phase saturations of water, oil and gas, respectively.

Similar expressions can be developed for three-phase water relative permeability (k_{rw}) and gas relative permeability (k_{rg}):

$$k_{rw} = \frac{S_{ow}}{S_{ow}+S_{gw}} k_{rwo}(S_{wo}) + \frac{S_{gw}}{S_{ow}+S_{gw}} k_{rwg}(S_{wg}) \qquad (2)$$

where S_{gw} and S_{wg} are the gas saturation and water saturation in the two-phase gas-water system. The two-phase saturations are linked to the given three-phase saturations by the following linear relationships:

$$S_{gw} = A_{gw} S_g \,, \qquad (2a)$$
$$S_{wg} = A_{wg} S_w \,. \qquad (2b)$$

The gas relative permeability is expressed as:

$$k_{rg} = \frac{S_{wg}}{S_{og}+S_{wg}} k_{rgw}(S_{gw}) + \frac{S_{og}}{S_{og}+S_{wg}} k_{rgo}(S_{go}) \qquad (3)$$

Eqs. (1), (2) and (3) represent a coupled nonlinear system of equations. In our study, the six two-phase relative permeabilities in Eqs. (1), (2) and (3) are expressed using the Mualem-Van Genuchten model (Appendix B). To quantify the characteristic coefficients A_{ij}, we used the NLFiT tool of Origin 2019 with the Levenberg-Marquardt iteration algorithm and user-defined fitting functions with multiple variables.

2.2 Total Differential (TD) compatible model

In a three-phase fluid (water-wet) system, there generally exist two fluid interfaces: oil-water and gas-oil. At both interfaces, there is a change in pressure, called capillary pressure, when moving from one fluid to the other. Moreover, the individual phase pressures can be singular in the case where the derivative of capillary pressure becomes infinite at residual saturations. Hence phase pressures cannot be regular across a two-phase interface. The Total Differential condition allows the two gradients of two-phase capillary pressures to be rewritten as a single gradient of a mathematical function called the global capillary pressure function P_c^g (Chavent and Jaffré, 1986; Chavent, 2009; di Chiara Roupert et al., 2010a). The resulting new pressure variable called global pressure p is written as the sum of the pressure of one of the three fluid phases and the global capillary pressure P_c^g . In our modeling approach, we used the gas pressure to define the global pressure. This is required when dealing with compressible three-phase flow. Note, the global pressure is smooth compared to the individual phase pressures and exhibits a global volumetric flow vector without any capillary gradients. This global pressure formalism specifically allows the decoupling of the pressure equation and the two saturation equations. The numerical analysis of the problem is thus simplified, and the efficiency of the calculation is improved. Note, the global pressure approach in a two and three-phase flow system exists only for data of relative permeabilities and capillary pressures that satisfy the Total Differential (TD) condition. The TD compatible model introduced by di Chiara Roupert et al. (2010a) uses continuous mathematical functions to describe the two-phase relative permeabilities and capillary pressures on the edges of the ternary diagram (Fig. 2). In the present study, we integrated experimental based residual fluid saturations in two-phase systems to quantify the mobility and global capillary pressure on the three boundaries. The way the integration was done is described in Section 4.2.

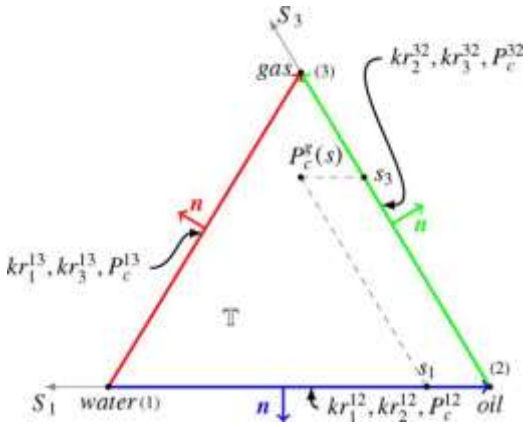

Fig. 2. Illustration of the ternary diagram $\mathbb{T}$ and the location of required two-phase data used in the TD compatible model (di Chiara Roupert et al. 2010b). s_j, p_j denote the saturation and pressure levels of phase j=1 (water), 2 (oil) and 3 (gas), and S_j, P_j their distribution (function of space and time variables). The ternary diagram is denoted by $\mathbb{T}$ and its boundary by $\partial\mathbb{T}$. A three-phase saturation distribution is denoted by $S=(S_1,S_3)$, and a point of the ternary diagram by $s=(s_1,s_3)$.

The input parameters required for the TD compatible model are two-phase relative permeabilities (kr_j^{kl}) and two-phase capillary pressures (P_c^{kl}) on the three edges of the ternary diagram (Fig. 2), where j=1, 2 or 3 and k≠l =1, 2 or 3. The independent variables are the water saturation (S_1) and gas saturation (S_3). Two-phase constitutive relationships used in the TD compatible model are described in Appendix A. The required model input parameters are obtained by considering primary drainage of a single phase fluid system. Further physical properties of the fluids taken into account are equilibrium interfacial tensions in the gas-water system (σ_{gw}), oil-water system (σ_{ow}), and gas-oil system (σ_{go}), water, gas, and oil densities and viscosities, molecular weight of the gas, gas constant, temperature, and reference density of gas.

The data available in the literature on Bentheimer and Berea sandstones were used as input parameters for the interpolation module (using finite elements) that was developed by di Chiara Roupert (2009). Then, for each rock sample, the three-phase data that are TD-compatible will be determined from a global capillary pressure function and a global mobility function, which depend on the saturation and overall global pressure level p. Note that the boundary conditions (of the ternary diagram) for the global capillary pressure and global mobility must be consistent with the three sets of two-phase data ("step 2" and "step 3" in Table 1) (di Chiara Roupert et al., 2010a). Note, in "step 2", one has to respect the so-called TD-compatibility condition. The three sets of two-phase data built up on the edges of the ternary diagram have to satisfy this condition. The global capillary pressure calculated independently on the oil/gas and water/gas side must be the same at the gas summit. The TD-compatibility condition is a nonlinear constraint on weighted means of the given two-phase relative permeability data set. It presents a certain weakness of this model in contrast to its strength of being free of elliptic zones in the saturation space. The two-phase data known on the limits of the ternary diagram will then be extended to the whole diagram and thus determine the relative permeabilities in a three-phase system by respecting the "Total Differential" condition. The numerical construction of the global mobility and global capillary pressure will then be performed by finite elements C0 ("step 4" in Table 1) and C1 ("step 5" in Table 1) using Laplacian and bi-Laplacian interpolation.

Relative permeabilities in three-phase systems will then be derived from global mobilities (d) ("step 4"), fluid fractional flows (f_i) ("step 5") using the derivatives of the global capillary pressures (p_c^g), the capillary pressure curves in a water-gas system (p_c^{12}) and gas-oil system (p_c^{32}) with respect to s_1 and s_3, individual mobilities (d_i) ("step 5") by

$$k_{r1}(s,p) = \frac{f_1(s,p)}{d_1} d(s,p)$$
$$k_{r2}(s,p) = \frac{f_2(s,p)}{d_2} d(s,p) \qquad (4)$$
$$k_{r3}(s,p) = \frac{f_3(s,p)}{d_3(p - P_c^g(s,p) + P_c^{32}(s_3))} d(s,p)$$

The relative permeabilities (k_{rj}) for the three fluid phases (with j: 1 = water, 2 = NAPL, 3 = gas) that will be quantified will then be compared with the three-phase experimental data.

Table 1. Partial Differential Equation-Total Differential (PDE-TD) interpolation algorithm for two-phase data (di Chiara Roupert et al. 2010a).

PDE-TD-interpolation algorithm

Require: p, k_{rk}^{ij} for k=i,j. $P_c^{12}(s_1)$, $P_c^{32}(s_3)$ for all s_1,s_3 in [0,1], M_3, R, T_3, ρ_3^0, μ_i

Ensure: $k_{rj}(s,p)$, $f_j(s,p)$, $\partial P_c^g / \partial p(s,p)$ for all s in $\mathbb{T}$

step 1: Solve non-linear Ordinary Differential Equations to obtain $(P_c^g)^{data}$ on $\partial\mathbb{T}$

step 2: Correct two-phase data for TD Compatibility

step 3: Compute d on $\partial\mathbb{T}$

step 4: Solve harmonic problem

$$\begin{cases} -\Delta d = 0 \ in \ \mathbb{T} \\ d = d^{data} \ on \ \partial\mathbb{T} \end{cases}$$

step 5: Solve biharmonic problem

$$\begin{cases} \Delta^2 P_c^g = 0 \ in \ \mathbb{T} \\ P_c^g = \left(P_c^g\right)^{data} \ on \ \partial\mathbb{T} \\ \frac{\partial P_c^g}{\partial n} = \left(\frac{\partial P_c^g}{\partial n}\right)^{data} \ on \ \partial\mathbb{T}_{12}, \partial\mathbb{T}_{23} \ and \ \partial\mathbb{T}_{13} \\ \frac{\partial P_c^g}{\partial \tau} = \left(\frac{\partial P_c^g}{\partial \tau}\right)^{data} \ on \ \partial\mathbb{T}_{12}, \partial\mathbb{T}_{23} \ and \ \partial\mathbb{T}_{13} \end{cases} \Longrightarrow Compute \ f_j, d_j$$

where n and τ are normal and tangential unit vectors on $\partial\mathbb{T}$

step 6: Compute $\frac{\partial P_c^g}{\partial p}(s,p), k_{ri}(s,p)$

2.3 Parker-Lenhard model

Based on the Van Genuchten parameter (m) (Appendix A), obtained from the capillary pressure-saturation (p_c-S) relationship in the two-phase gas-water system, and the irreducible wetting fluid saturation (S_{wi}), water, oil, and gas relative permeabilities in a three-phase fluid system can be predicted. The water relative permeability k_{rw} is described by

$$k_{rw} = \overline{S_w}^{1/2} \left\{ 1 - \left[1 - \overline{S_w}^{1/m} \right]^m \right\}^2 \qquad (5)$$

with: $\overline{S_w} = \frac{S_w - S_{wi}}{S_{max} - S_{wi}}$,

where S_{wi} is the irreducible saturation of the wetting fluid phase (here water) and S_m is the maximum saturation of the wetting fluid phase. During drainage of the porous medium, water is displaced for example by gas, the maximum saturation S_{max} is equal to 1. Note that the maximum saturation of the wetting fluid phase S_{max} is considered to be independent of fluid properties or saturation history. In the present work, we focused our attention to monotonic wetting phase drainage from (complete) saturation.

The oil relative permeability k_{ro} is expressed as

$$k_{ro} = \left(\overline{S_t} - \overline{S_w}\right)^{1/2} \left\{\left[1 - \overline{S_w}^{1/m}\right]^m - \left[1 - \overline{S_t}^{1/m}\right]^m\right\}^2 \qquad (6)$$

where: $\overline{S_t} = \frac{S_w + S_o - S_{wi}}{1 - S_{wi}}$.

The gas relative permeability k_{rg} is described by

$$k_{rg} = \left(1 - \overline{S_t}\right)^{1/2} \left\{1 - \overline{S_t}^{1/m}\right\}^{2m} \qquad (7)$$

where: $\overline{S_t} = \frac{S_w + S_o - S_{wi}}{1 - S_{wi}} = \frac{1 - S_g - S_{wi}}{1 - S_{wi}}$

2.4 Stone's model I

To quantify the oil relative permeability in a three-phase system, the first model proposed by Stone in 1970 uses a geometric averaging between the oil relative permeability k_{rog} in the two-phase gas-oil system and the oil relative permeability k_{row} in the two-phase oil-water system:

$$k_{ro} = \frac{S_o^*}{(1 - S_g^*)(1 - S_w^*)} k_{rog}(S_g) k_{row}(S_w) \qquad (8)$$

In this equation, S_o^*, S_g^* and S_w^* are the normalized oil, gas, and water saturations, respectively, and are defined as:

$$S_o^* = \frac{S_o - S_{or}}{1 - S_{wi} - S_{or}}, \qquad (8a)$$

$$S_g^* = \frac{S_g}{1 - S_{wi} - S_{or}}, \qquad (8b)$$

$$S_w^* = \frac{S_w - S_{wi}}{1 - S_{wi} - S_{or}}, \qquad (8c)$$

where S_{wi} and S_{or} are irreducible water saturation and residual oil saturation, respectively.

In our study, two-phase oil relative permeability in the gas-oil system is expressed by the Mualem-Van Genuchten (MVG) model (Mualem, 1976; van Genuchten, 1980):

$$k_{rog}(S_g) = \sqrt{\frac{S_o - S_{or}}{1 - S_{or}}} \left[1 - \left(1 - \left(\frac{S_o - S_{or}}{1 - S_{or}}\right)^{1/m_{og}}\right)^{m_{og}}\right]^2 = \sqrt{\frac{1 - S_g - S_{or}}{1 - S_{or}}} \left[1 - \left(1 - \left(\frac{1 - S_g - S_{or}}{1 - S_{or}}\right)^{1/m_{og}}\right)^{m_{og}}\right]^2 \qquad (8d)$$

and two-phase oil relative permeability in the oil-water system is expresses by the modified Mualem-Van Genuchten model:

$$k_{row}(S_w) = k_{row,max} \sqrt{\left(1 - \frac{S_w - S_{wi}}{1 - S_{wi}}\right)} \left[1 - \left(\frac{S_w - S_{wi}}{1 - S_{wi}}\right)^{1/m_{ow}}\right]^{2m_{ow}} \qquad (8e)$$

where $k_{row,max}$ is the maximum relative oil permeability achieved at irreducible water saturation S_{wi} in the oil-water system. m_{og} and m_{ow} correspond to the MVG parameter in a gas-oil system and oil-water system, respectively.

3. Experimental data

To evaluate and compare the four mathematical models explained earlier, experimental data generated on two different water-wet sandstones were selected from the literature.

3.1 Data on Bentheimer sandstone

Alizadeh (2013) performed a series of steady-state flow experiments on water-wet Bentheimer sandstone to obtain two-phase and three-phase relative permeabilities. The absolute brine permeability and porosity of the core sample whose data were used in our study were 2.66 D and 0.24, respectively (Alizadeh and Piri, 2014b). The physical properties of the fluids used in the flow experiments are provided in Table 2.

Table 2. Fluid properties of experiments on Bentheimer sandstone (Alizadeh, 2013; Alizadeh and Piri, 2014b)

	Nitrogen-Brine	Oil-Brine	Nitrogen-Oil
Interfacial tension [mN/m]	61.714	40.766	20.957
Fluid phase	Gas (Nitrogen)	Oil	Water (Brine)
Densities [kg/m^3]	62.84	802.13	1138.12
Dynamic viscosities [cP] at 21.1°C, 800 psig	0.0187 (#)	2.526	1.144

(#) *Oak, 1990*

The two-phase relative permeabilities obtained during primary drainage in oil-water, gas-water, and gas-oil systems are plotted in Fig. 3 and compared to the simulated two-phase relative permeabilities using the MVG model. To quantify the input parameter for the MVG model, we used the experimentally determined end-point wetting-phase saturations and the associated nonwetting-phase relative permeability as known. irreducible water saturations (S_{wi}) in the oil-water and gas-water systems, remaining oil saturation (S_{or}) in the gas-oil system, and maximum relative permeability of the nonwetting fluid ($kr_{nw,max}$). The only remaining model parameter, MVG parameter m, was then obtained by a nonlinear fit of the theoretical k_r-S against the experimentally observed permeability curve using the NLFiT tool of Origin 2019 with the Levenberg-Marquardt iteration algorithm.

The capillary pressure-saturation curve measured by Alizadeh (2013) for a gas-water system was analysed numerically with the Van Genuchten model (Fig. 3). The optimal calibration of the experimental p_c-S data was obtained using the fit of the three model parameters: S_{wi}, m, α. All fit parameters and characteristics of the optimization process are listed in Table C1 (Appendix C). It is worthwhile to mention that the irreducible water saturation or residual oil saturation quantified from capillary pressure curves is systematically smaller than that observed experimentally in the two-phase flow experiment. From the theoretical point of view, the numerical value of parameter m derived from the MVG model should be equal to that of parameter m appearing in the Van Genuchten (Pc-S) model. As the aim of our study is to represent as close as possible the experimental constitutive relationships, we preferred to keep fitted the parameter m in both relationships.

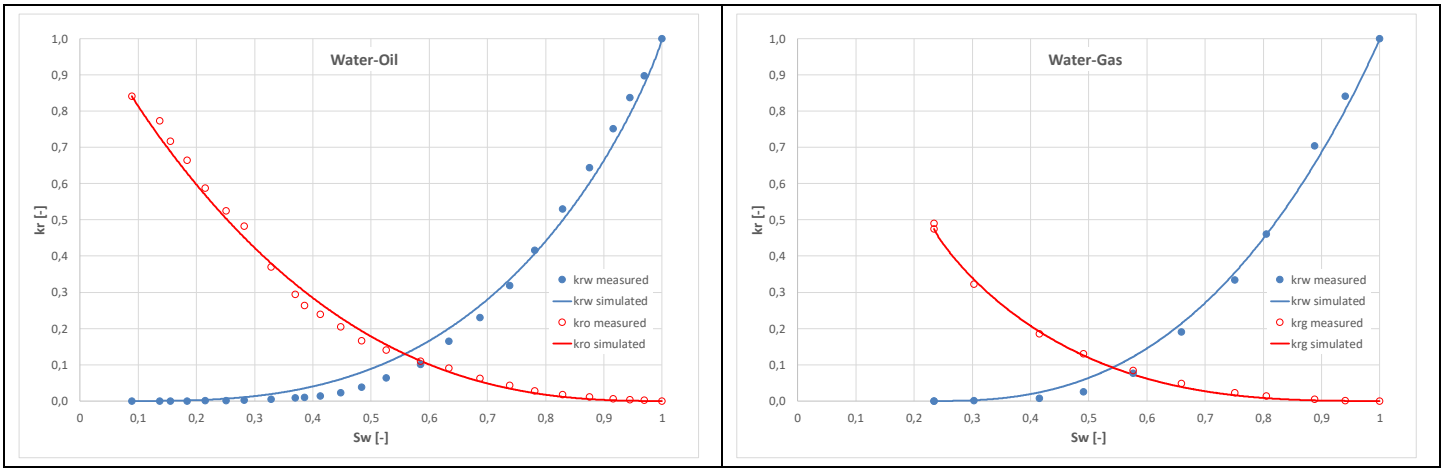

(a)

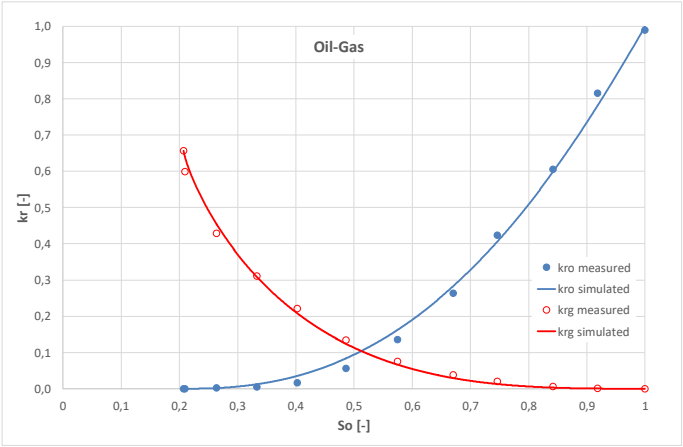

(b)

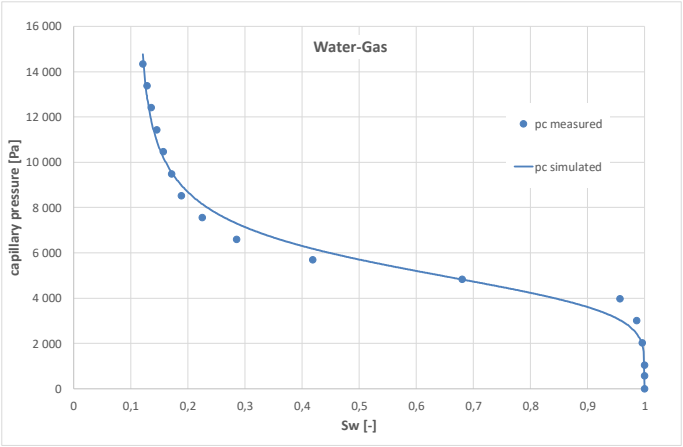

(c)

(d)

Fig. 3. Measured and simulated two-phase constitutive relationships for Bentheimer sandstone: (a) water-oil relative permeability versus water saturation, (b) water-gas relative permeability versus water saturation, (c) oil-gas relative permeability versus oil saturation, and (d) water-gas capillary pressure as a function of water saturation (Alizadeh, 2013; Alizadeh and Piri, 2014b).

3.2 Data on Berea sandstone

Oak (1990) performed a series of steady-state flow experiments on water-wet Berea sandstone to obtain two-phase and three-phase relative permeabilities. The absolute permeability and porosity of the core sample whose data were used here were 0.2 D and 0.22. The physical properties of the fluids used in his experiments are provided in Table 3.

The two-phase relative permeabilities obtained in Experiments 2, 8, and 13 were conducted in oil-water, gas-water and oil-gas systems. The measured and numerically simulated two-phase relationships are presented in Fig. 4. The capillary pressure-saturation curves determined in Oak's experiments in a gas-water, water-oil and oil-gas system were analysed numerically with the Van Genuchten model (Fig. 4). All fit parameters and characteristics of the optimization process are summarized in Table C2 (Appendix C).

Table 3. Fluid properties of flow experiments on Berea sandstone (0ak, 1990)

	Nitrogen-Brine	Oil-Brine	Nitrogen-Oil
Interfacial tension [mN/m]	72	53	25 (#)
Fluid phase	Gas (Nitrogen)	Oil	Water (Brine)
Densities [kg/m^3], at 800 psig	62.84	752	1000
Dynamic viscosities [cP] at 21 °C	0.0187	1.77	1.06

(#) *Oak et al. (1990)*

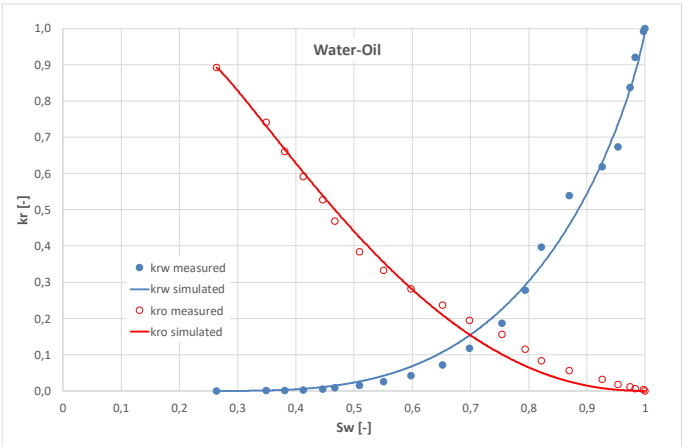

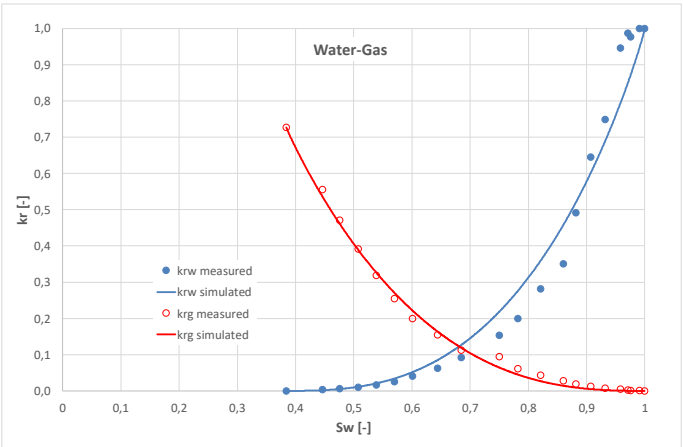

(a)

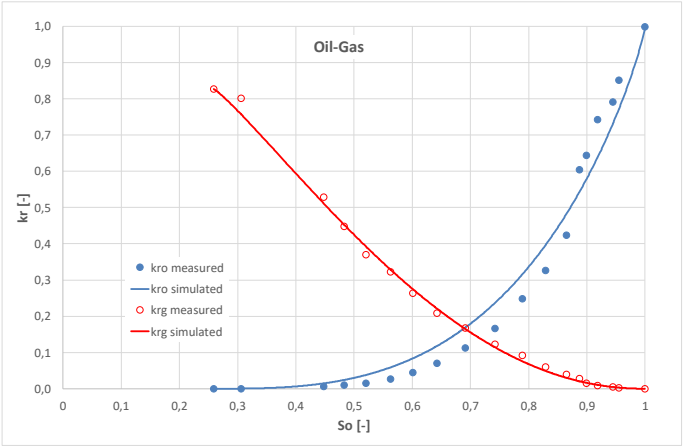

(b)

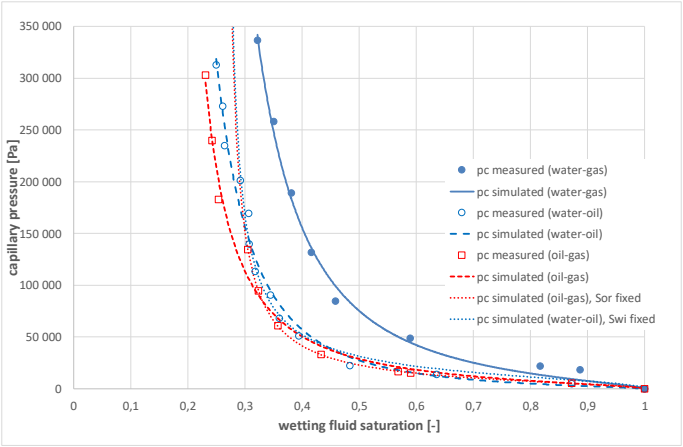

(c)

(d) *NB: pc-S data digitized from Oak et al. (1990)*

Fig. 4. Measured and simulated two-phase constitutive relationships for Berea sandstone: (a) water-oil relative permeability versus water saturation, (b) water-gas relative permeability versus water saturation, (c) oil-gas relative permeability versus oil saturation, and (d) water-gas, water-oil, and oil-gas capillary pressure curves as functions of wetting-phase saturation (Oak, 1990).

3.3 Comparison of measured and predicted three-phase k_r values

The saturation path of three decreasing water saturation/decreasing oil saturation/increasing gas saturation (DDI) experiments performed on Bentheimer sandstone by Alizadeh and Piri (2014b) and 7 DDI experiments performed on Berea sandstone by Oak (1990) are shown in Fig. 5. The experimental two- and three-phase relative permeabilities obtained on the Bentheimer and Berea sandstones were used to predict three-phase flow in porous media using the four mathematical models described earlier in section 2.

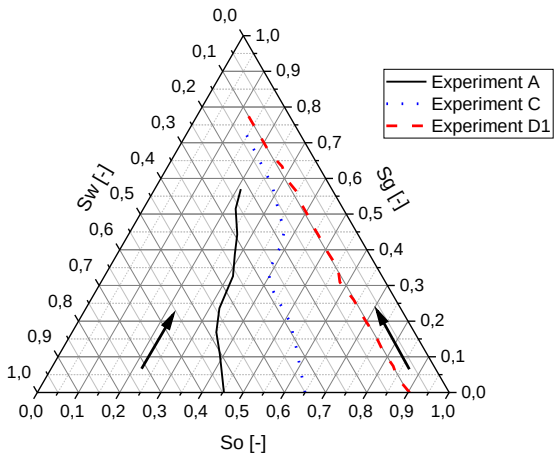

(a)

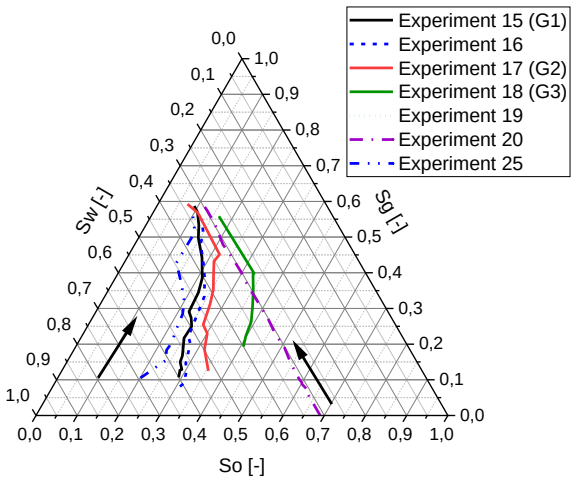

(b)

Fig. 5. Saturation path of DDI experiments conducted on (a) Bentheimer sandstone (Alizadeh and Piri, 2014b) and (b) on Berea sandstone (Oak, 1990). Arrows indicate the direction of saturation path chosen.

In our numerical study, the model performance was evaluated by quantitative and qualitative methods. In the qualitative approach, the response of each model was first visually analyzed by plotting the measured and simulated values of relative permeabilities as functions of the saturation of the corresponding fluid phase. To quantify the goodness of the prediction of the measured k_r values, we used the root mean square error (RMSE)

$$RMSE = \sqrt{\frac{1}{n}\sum_{i=1}^{n}(M_i - P_i)^2} \quad (9)$$

the coefficient of residual mass (CRM)

$$CRM = \frac{\sum_{i=1}^{n} M_i - \sum_{i=1}^{n} P_i}{\sum_{i=1}^{n} M_i} \quad (10)$$

the relative error (RE) defined as

$$RE = \frac{P_i - M_i}{M_i} \quad (11)$$

and the maximum relative error (MRE) expressed by

$$MRE = \frac{max|P_i - M_i|_{i=1}^{n}}{max M_i} \quad (12)$$

where M_i and P_i represent the measured and predicted k_r values, and n is the number of experimental data.

The RMSE is an accuracy index and expresses the average model prediction error in units of the variable of interest. It can range from 0 to ∞, is indifferent to the direction of errors, and represents negatively oriented scores. The CRM illustrates the tendency of a model to overestimate or underestimate the measurements (positive values for CRM indicate that the model underestimates the measurements and negative values for CRM indicate a tendency to overestimate).

To analyze globally the response and goodness of the different models to predict the three-phase relative permeabilities of water, oil, and gas, we plotted the simulated k_r values against the measured k_r values and analyzed the scatter plot by linear regression (using OriginLab 2019). The quantified coefficient of determination (R-squared) is expressed by:

$$R^2 = \frac{1}{n}\frac{\sum_{i=1}^{n}\left[(M_i - \overline{M})(P_i - \overline{P})\right]^2}{\sigma_M \times \sigma_P} \quad \text{, with } \overline{M} = \frac{1}{n}\sum_{i=1}^{n} M_i \text{ and } \overline{P} = \frac{1}{n}\sum_{i=1}^{n} P_i \quad , \quad (13)$$

where σ_M qnd σ_P are the standard deviation of M_i and P_i, respectively. R-squared is a statistical measure of how close the data are to the fitted regression line and demonstrates thus the ratio between the scatter of predicted values to the measured values.

4. Results of the numerical modeling

4.1 Mechanistic model of Shahverdi & Sohrabi

4.1.1 Implementation of the model

To test the implementation of the mechanistic model developed by Shahverdi and Sohrabi (2017), we used Oak's Experiment 15 (or named G1 in Shahverdi and Sohrabi (2017)). The six two-phase relative permeabilities are expressed by the Mualem-Van Genuchten model (see Appendix B). The used model parameters are reported in Table 4. To quantify the characteristic coefficients, A_{ij}, shown in Table 5, we used the NLFiT tool of Origin 2019 with the Levenberg-Marquardt iteration algorithm and user-defined fitting functions with multiple variables.

Table 4. Model input parameter used to describe the experimental two-phase relative permeabilities from the Oak experiment on Berea sandstone

Oil-Water system		Gas-Water system		Gas-Oil system	
m_{wo}	m_{ow}	m_{wg}	m_{gw}	m_{og}	m_{go}
0.80594	0.84696	0.91241	1.05023	0.84498	0.81252
S_{wi}^{wo}	S_{wi}^{ow}	S_{wi}^{wg}	S_{wi}^{gw}	S_{or}^{og}	S_{or}^{go}
0.264	0.264	0.384	0.384	0.259	0.259
	$k_{row,max}$		$k_{rgw,max}$		$k_{rgo,max}$
	0.892		0.727		0.827

Table 5. Quantified characteristic coefficients A_{ij} and uncertainty intervals (standard errors) associated with model parameter estimates by fitting the three-phase k_r of Experiment 15 (R-squared=0.99)

A_{ow}	A_{og}	A_{wo}	A_{wg}	A_{go}	A_{gw}
0.6178 ± 0.051	1 ± 38.569	0.9894 ± 0.029	0.3269 ± 12.579	0.6942 ± 0.042	1 ± 0.109

The fit of Oak's experimental data (originating from Experiment 15 on soil sample 6 (which corresponds to Experiment G1 named by Shahverdi and Sohrabi (2017)) was achieved in our runs after 420 iterations with a Chi-square tolerance value of 1×10^{-9}, giving a fit result with R-squared of 0.99. It is worth noting that the uncertainty intervals obtained for the characteristic coefficients A_{og} and A_{wg} (Table 5) are extremely high compared to their numerical values, which were bounded in the fitting procedure between 0 and 1. The predicted k_r values of Oak's DDI experiments shown in the following are obtained using the model parameter estimates given in Table 5. We did not yet consider them in our modeling approach to predict the level of uncertainty associated with these parameter estimates through i.e. an assessment of the covariance matrix. However, the estimated coefficients A_{ij} are quite different from the numerical values published by Shahverdi and Sohrabi (2017), who used the Genetic algorithm as described in Shahverdi et al. (2011), in their nonlinear fitting procedure for estimation of relative permeability. The relative permeabilities for the corresponding two-phase systems similar to ours, the way of implementing the two-phase relative permeabilities (in our case by using the analytical function of MVG model; in their case spline functions), and the automatic fitting procedure itself seem to significantly impact the numerical values of estimated coefficients A_{ij}. The main differences can be summarized as follows: In our work, (1) A_{og} is greater than A_{ow}, hence the oil phase is more dominated by the gas phase than the water phase, and (2) the comparison between A_{go} and A_{gw} indicates that more fraction of gas saturation is governed by water. However, as shown in Fig. 6, the detailed comparison of fitted k_r values against the experimental data indicates that our fitted k_r values have RMSEs values that are comparable with the tuned k_r values found by Shahverdi and Sohrabi (2017). It is certainly not surprising that the estimation of these characteristic coefficients does not allow a unique solution. This is related not only to the nature of the inverse problem but also to the approach employed to the minimization of a given objective function.

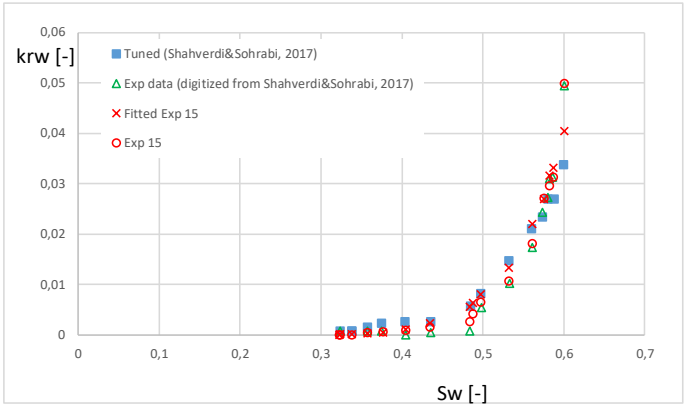

(a)

Tuned (Shahverdi&Sohrabi,2017)		RMSE= 0.0041	CRM= 0.139
Fitted Exp 15	(MRE=0.188)	RMSE= 0.0029	CRM=-0.044

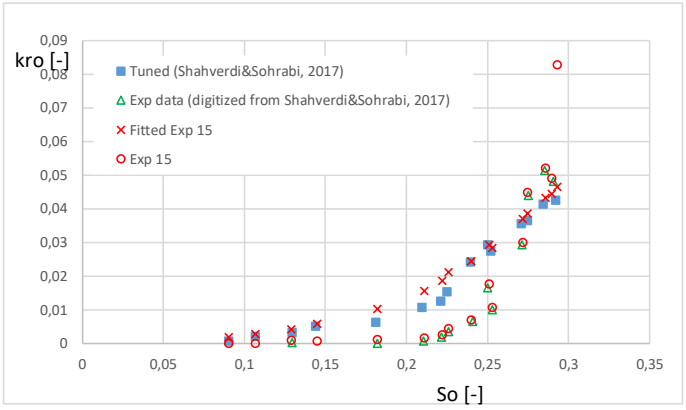

(b)

Tuned (Shahverdi&Sohrabi,2017)		RMSE= 0.0099	CRM= -0.399
Fitted Exp 15	(MRE=0.438)	RMSE= 0.0109	CRM= -0.215

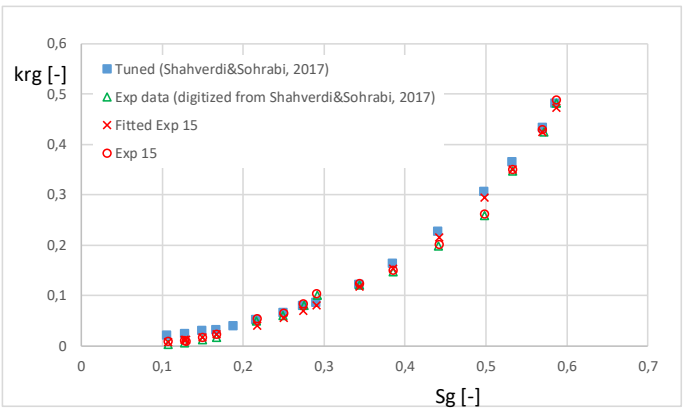

(c)

Tuned (Shahverdi&Sohrabi,2017)		RMSE= 0.0191	CRM= -0.010
Fitted Exp 15	(MRE=0,065)	RMSE= 0.0123	CRM= 0.014

Fig. 6. Comparison of relative permeabilities measured from Oak's DDI Experiment 15 (G1) and those

obtained from the mechanistic model by fitting the characteristic coefficients A_{ij}: (a) water relative permeability versus water saturation, (b) oil relative permeability versus oil saturation, and (c) gas relative permeability versus gas saturation.

To further explain the observed differences, a profile likehood analysis could be carried out for each given DDI path (Ranaee, 2015) in order to investigate for some given upper and lower limits of confidence intervals, if the model displays a unique minimum (identifiability case) or, on the contrary, if the case is not structurally identifiable. One can therefore make “a priori” choice on the path to be chosen in order to guarantee an exploitable fitted model. In our study, we have chosen to use automatic nonlinear minimization of the objective function using the NLFiT tool implemented in Origin 2019 with the Levenberg-Marquardt iteration algorithm, whereas the coefficients generated by Shahverdi and Sohrabi (2017) were determined with a genetic algorithm. To build up the objective function we used a continuous description of data sets using the constitutive analytical MVG relationship whereas the genetic algorithm approach implemented by Shaverdi and Sohrabi (2017) was based on k_r values represented by quadratic B-Spline functions. Note also that the quantified coefficient of residual mass (CRM) do not always exhibit similar tendencies: for example, the water relative permeability is underestimated by Shahverdi and Sohrabi (2017) and only slightly overestimated in our study whereas the estimates of gas relative permeabilities show contrary trend.

Concerning the prediction of k_r -values, globally, our results obtained for Experiments 17 ("G2") and 18 ("G3") are similar to those obtained by Shahverdi and Sohrabi. The detailed comparison of predicted k_r values (water, oil, gas) for Experiments 17 and 18 with those of Shahverdi and Sohrabi (2017) is documented in Appendix D.

4.1.2 Prediction of Oak’s DDI Experiments 16, 19, 20 and 25

Figs. 7-10 show the predicted three-phase relative permeabilities along the DDI saturation paths of Experiment 16, 19, 20 and 25. Not surprisingly, the relative permeabilities predicted for Experiment 16 by the mechanistic model clearly represent the measured k_r values. Its DDI saturation path is close to that of Experiment 15 used in the calibration process of the characteristic coefficients A_{ij} (Fig. 3) and therefore the numerical values of CRM and MRE are quite similar. The relative permeabilities predicted in Experiment 19 and 25 for water and gas also perfectly fits the observed experimental data expressed by low RMSEs and low MREs, ranging between 1 and 17%. However, the oil relative permeabilities are strongly overestimated as shown by the high negative values of CRM. In the case of Experiment 20, which corresponds to a saturation path at irreducible water saturation, the water relative permeability is predicted as very close to zero (Fig. 9). Surprisingly, in this case, the predicted oil relative permeabilities as well as the gas relative permeabilities are highly underestimating the observed values. The MRE value attains about 64 and 28% for the predicted oil and gas permeability, respectively.

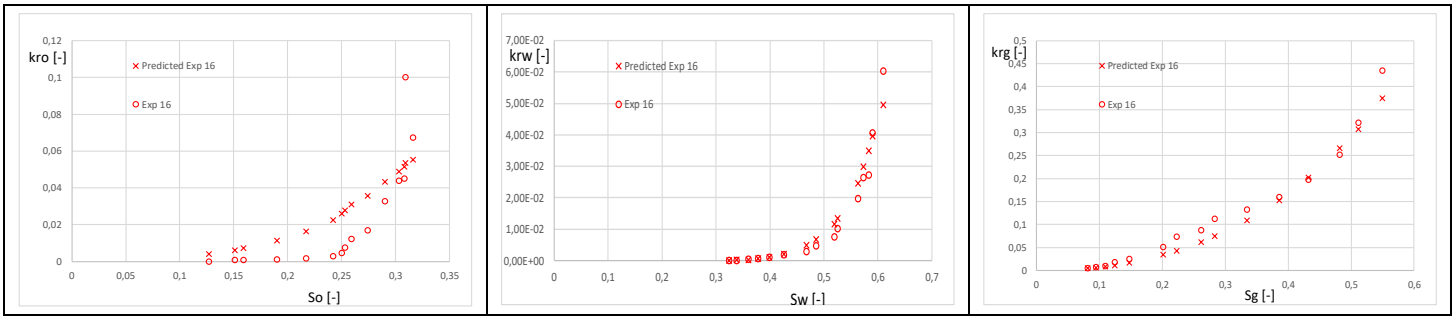

(a) RMSE=0.01792 ; CRM=-0.304 ; MRE=0.464 | (b) RMSE=0.00407 ; CRM=-0.077; MRE=0.008 | (c) RMSE= 0.02318 ; CRM=0.113 ; MRE=0.138

Fig. 7. Relative permeabilities measured from Oak’s DDI Experiment 16 compared to those obtained from the mechanistic model: (a) oil relative permeability versus oil saturation, (b) water relative permeability versus water saturation, and (c) gas relative permeability versus gas saturation

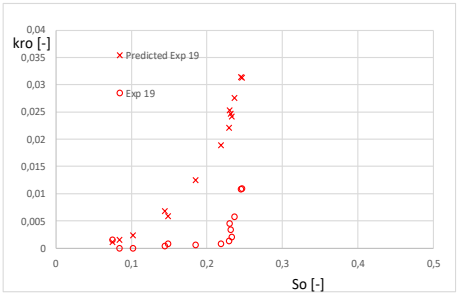

(a) RMSE=0.01617 ; CRM=-4.489 ; MRE=2.028

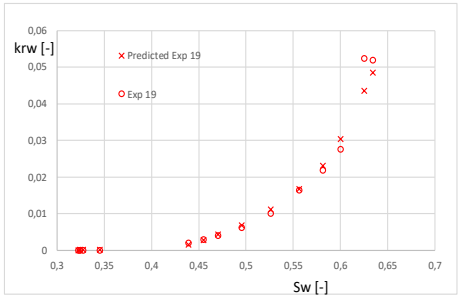

(b) RMSE=0.00270 ; CRM=0.033 ; MRE=0.169

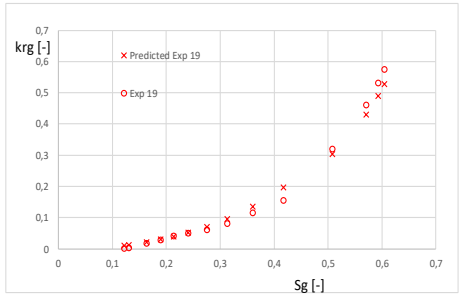

(c) RMSE= 0.02386 ; CRM=0.013 ; MRE=0.084

Fig. 8. Relative permeabilities measured from Oak's DDI Experiment 19 compared to those obtained from the mechanistic model: (a) oil relative permeability versus oil saturation, (b) water relative permeability versus water saturation, and (c) gas relative permeability versus gas saturation.

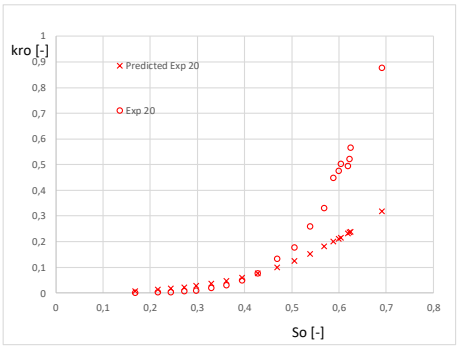

(a) RMSE=0.19314 ; CRM=0.494 ; MRE=0.637

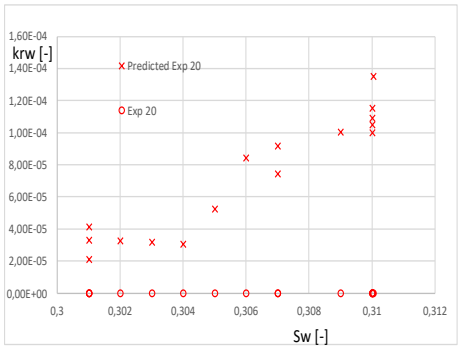

(b) RMSE= 7×10^{-05} ; CRM= undef. ; RE=undef.

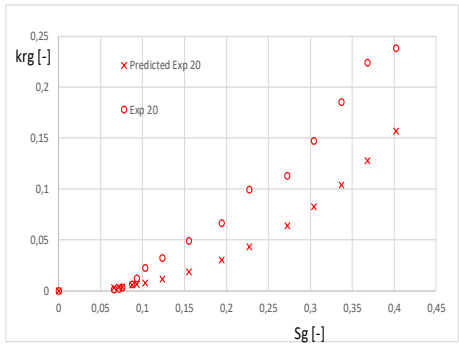

(c) RMSE= 0.06246; CRM=0.290; MRE=0.280

Fig. 9. Relative permeabilities measured from Oak's DDI Experiment 20 compared to those obtained from the mechanistic model: (a) oil relative permeability versus oil saturation, (b) water relative permeability versus water saturation, and (c) gas relative permeability versus gas saturation.

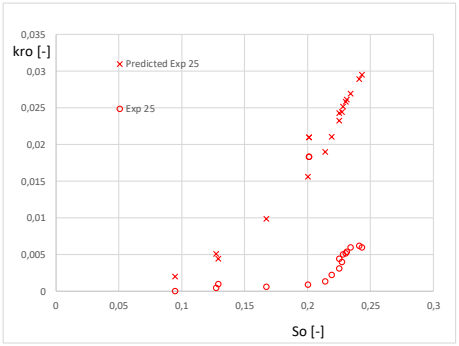

(a) RMSE=0.01668 ; CRM=-2.996 ; MRE=1.284

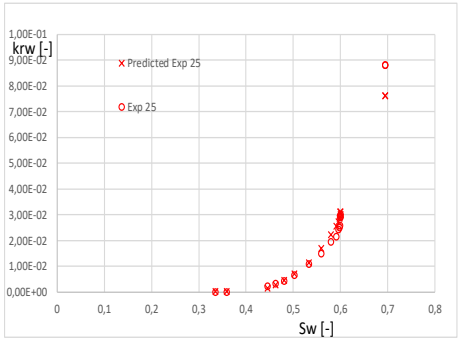

(b) RMSE=0.00446 ; CRM=0.0004; MRE=0.136

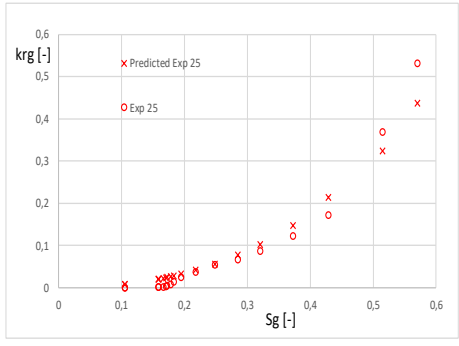

(c) RMSE= 0.02998 ; CRM=0.030 ; MRE=0.018

Fig. 10. Relative permeabilities measured from Oak's DDI Experiment 25 compared to those obtained from the mechanistic model: (a) oil relative permeability versus oil saturation, (b) water relative permeability versus water saturation, and (c) gas relative permeability versus gas saturation.

4.1.3 Prediction of Alizadeh's experiments on Bentheimer sandstone

The required input parameters used for the description of the experimental two-phase relative permeabilities in the mechanistic model (see Appendix B) are summarized in Table 6. To test the influence of the characteristic coefficients Aij on the prediction of the three-phase relative permeabilities along the three DDI saturation paths, we decided to apply three options: to quantify the coefficients A_{ij} by nonlinear fit we used (1) in option A the measured k_r values of Experiment A, (2) in option C the experimental results of Experiment C, and (3) in option AC both data sets of results. The quantified characteristic coefficients A_{ij} for each of the three options are reported in Table 7. It is worth noting that the uncertainty intervals obtained for the characteristic coefficient A_{wg} are high compared to their numerical values, which were bounded in the fitting procedure between 0 and 1. Especially in modelling option A, the standard error of A_{wg} is extremely high and underlines that the model parameter obtained is rather uncertain. The predicted k_r values of Alizadeh's DDI experiments

shown in the following are obtained using the model parameter estimates given in Table 7. We did not yet consider them in our modeling approach to predict the level of uncertainty associated with these parameter estimates through i.e. an assessment of the covariance matrix. Comparing the resulting coefficients from option A with those quantified from option C, unlike the numerical value of A_{ow}, the differences are quite significant. A_{og}, for example, which characterizes the relation between the oil saturation in the two-phase oil-gas system and oil saturation in the three-phase fluid system, is found to be zero in option A, while in option C it takes the maximum value of 1. A similar fact can be stated for coefficient A_{wg}. In option AC, the quantified characteristic coefficients are situated between either option A and option C, or closer to the coefficients of option C. The latter can be attributed to the fact that the data set of Experiment C contains more values than the data set of Experiment A.

Table 6. Model input parameter to describe the experimental two-phase relative permeabilities

Oil-Water system		Gas-Water system		Gas-Oil system	
m_{wo}	m_{ow}	m_{wg}	m_{gw}	m_{og}	m_{go}
0.87578	1.0207	0.9718	1.1499	1.0359	1.2618
S_{wi}^{wo}	S_{wi}^{ow}	S_{wi}^{wg}	S_{wi}^{gw}	S_{or}^{og}	S_{or}^{go}
0.089	0.089	0.234	0.234	0.207	0.207
	$k_{row,max}$		$k_{rgw,max}$		$k_{rgo,max}$
	0.841		0.475		0.657

Table 7. Quantified characteristic coefficients A_{ij} and uncertainty intervals (standard errors) associated with model parameter estimates by fitting the three-phase k_r of (1) Experiment A - called option A (R-Squared=0.86), (2) Experiment C - called option C (R-squared = 0.94) and (3) Experiments A and C – called option AC (R-squared = 0.93).

A_{ow}	A_{og}	A_{wo}	A_{wg}	A_{go}	A_{gw}
(1) Option A					
0.9848 ± 0.056	0 ± 0.174	0.9179 ± 0.046	$0.0956 \pm 3.5\times10^{8}$	1 ± 0.810	0.9054 ± 0.16
(2) Option C					
1 ± 0.031	1 ± 0.133	0.8050 ± 0.528	1 ± 3.695	0.8574 ± 0.272	1 ± 0.186
(3) Option AC					
1 ± 0.024	1 ± 0.096	0.9228 ± 0.057	0.506 ± 2.210	0.8891 ± 0.114	1 ± 0.275

Figs. 11-13 show the fitted and predicted three-phase relative permeabilities along the DDI saturation paths of Experiment A, C and D1. To qualify the goodness of each of the numerical simulations, we specified the corresponding RMSE, CRM and MRE. The simulated water relative permeabilities of Experiment A and C globally overestimates the experimental values. Note that Experiment D1 corresponds to the case where water is at irreducible saturation and thus immobile. However, the oil relative and gas relative permeability measured in Experiment C and D1 are both underestimated by all three model options.

The detailed comparison of all predicted/fitted k_r values with the measured values show that the numerical results obtained with coefficients of option C and AC are overly closer to the experimental data than those quantified with coefficients of option A. One reason for this may be the higher number of data points considered during the optimization procedure of the characteristic coefficients A_{ij}, but also the more central location of DDI saturation path of Experiment C in the ternary diagram. The use of two experimental data sets (option AC) for tuning of the characteristic coefficients, as suggested by Shahverdi and Sohrabi (2017), to reduce the degree of uncertainty by employing more measured data of three-phase relative permeabilities, slightly improves only the goodness of predicted k_r values. Therefore, in the following global analysis we will only consider the simulated results obtained with model option C.

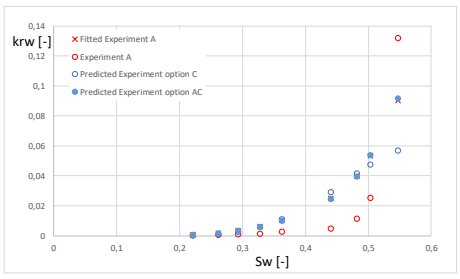

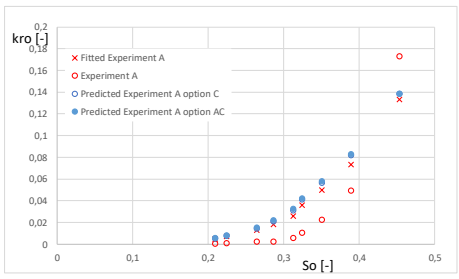

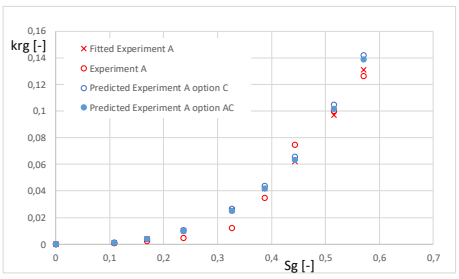

(a)	(b)	(c)
Fitted Experiment A		
RMSE=0.02067 ; CRM=-0.284 ; MRE=0.318	RMSE=0.01759 ; CRM=-0.352 ; MRE=0.231	RMSE=0.00724 ; CRM=-0.052 ; MRE=0.109
Predicted Experiment A using coefficients Aij of option C		
RMSE=0.02936 ; CRM=-0.093 ; MRE=0.570	RMSE=0.02211 ; CRM=-0.492 ; MRE=0.200	RMSE=0.00881 ; CRM=-0.124 ; MRE=0.127
Predicted Experiment A using coefficients Aij of option AC		
RMSE=0.02020 ; CRM=-0.287 ; MRE=0.305	RMSE=0.02294 ; CRM=-0.518 ; MRE=0.203	RMSE=0.00786 ; CRM=-0.085 ; MRE=0.103

Fig. 11. Relative permeabilities measured from Alizadeh's DDI Experiment A compared to those fitted and predicted (using option C and option AC): (a) water relative permeability versus water saturation, (b) oil relative permeability versus oil saturation, and (c) gas relative permeability versus gas saturation.

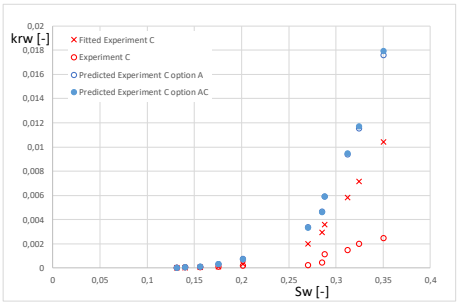

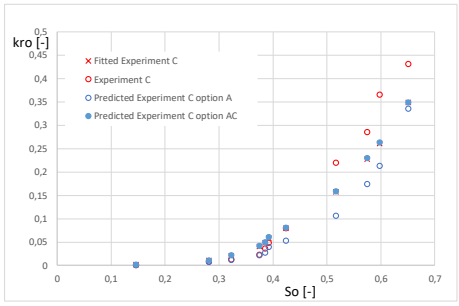

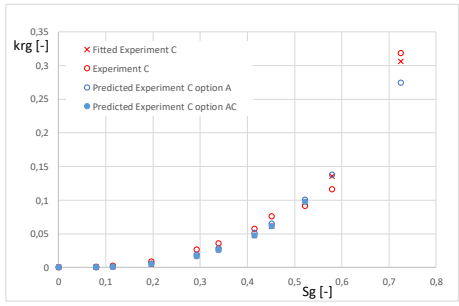

(a)	(b)	(c)
Fitted Experiment C		
RMSE=0.00335 ; CRM=-2.972 ; MRE=3.245	RMSE=0.04111 ; CRM=0.170 ; MRE=0.241	RMSE=0.00979 ; CRM=0.048 ; MRE=0.061
Predicted Experiment C using coefficients Aij of option A		
RMSE=0.00628 ; CRM=-5.600 ; MRE=6.171	RMSE=0.06675 ; CRM=0.344 ; MRE=0.352	RMSE=0.01584 ; CRM=0.069 ; MRE=0.138
Predicted Experiment C using coefficients Aij of option AC		
RMSE=0.00638 ; CRM=-5.658 ; MRE=6.322	RMSE=0.04040 ; CRM=0.162 ; MRE=0.237	RMSE=0.01035 ; CRM=0.049 ; MRE=0.066

Fig. 12. Relative permeabilities measured from Alizadeh's DDI Experiment C compared to those fitted and predicted (using option A and option AC): (a) water relative permeability versus water saturation, (b) oil relative permeability versus oil saturation, and (c) gas relative permeability versus gas saturation.

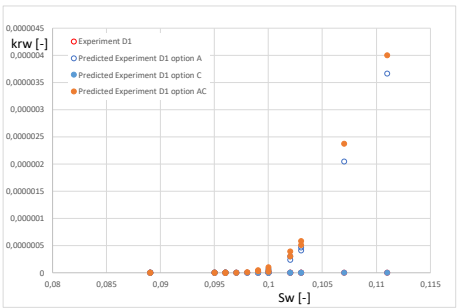

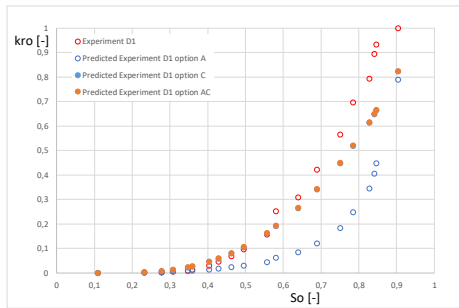

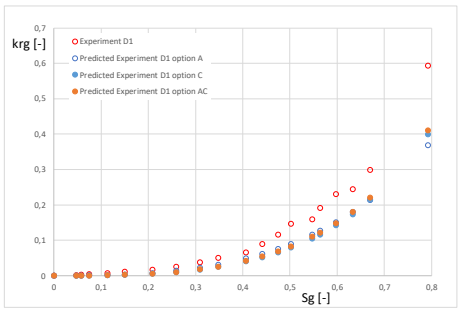

(a)	(b)	(c)
Predicted Experiment using coefficients Aij of option A		
RMSE=9.52×10^{-07} ; CRM=undef ; MRE=undef	RMSE=0.25118 ; CRM=0.5467 ; MRE=0.489	RMSE=0.06373 ; CRM=0.340 ; MRE=0.379
Predicted Experiment using coefficients Aij of option C		
RMSE=3.62×10^{-11} ; CRM=undef ; MRE=undef	RMSE=0.11295 ; CRM=0.200 ; MRE=0.269	RMSE=0.06208 ; CRM=0.368 ; MRE=0.327
Predicted Experiment using coefficients Aij of option AC		
RMSE=1.06×10^{-06} ; CRM=undef ; MRE=undef	RMSE=0.11195 ; CRM=0.196 ; MRE=0.267	RMSE=0.05835 ; CRM=0.346 ; MRE=0.310

Fig. 13. Relative permeabilities measured from Alizadeh's DDI Experiment D1 compared to those predicted using option A, C and option AC: (a) water relative permeability versus water saturation, (b) oil relative permeability versus oil saturation, and (c) gas relative permeability versus gas saturation.

4.1.4 Global analysis of predicted three-phase relative permeabilities

For further investigation of the accuracy of the model, the three-phase relative permeabilities predicted by the model for each fluid phase are plotted against the measured relative permeabilities obtained for Berea and Bentheimer sandstone (Figs. 14-16). Each figure also contains a description of the quantified relative error as a function of the measured relative permeability in the three-phase system.

In the case of Berea sandstone, as shown by the cross-plot (Fig. 14), the water relative permeability is reasonably well predicted by the mechanistic model. Globally, it slightly overestimates the measured k_r values characterized by a relative error of about 0.13±0.53. However, for the Bentheimer sandstone, the predicted water relative permeabilities deviate strongly from the experimental measurements. In this case, the scatter of the predicted values to the measured values is strongly disordered and cannot be reasonably described by the

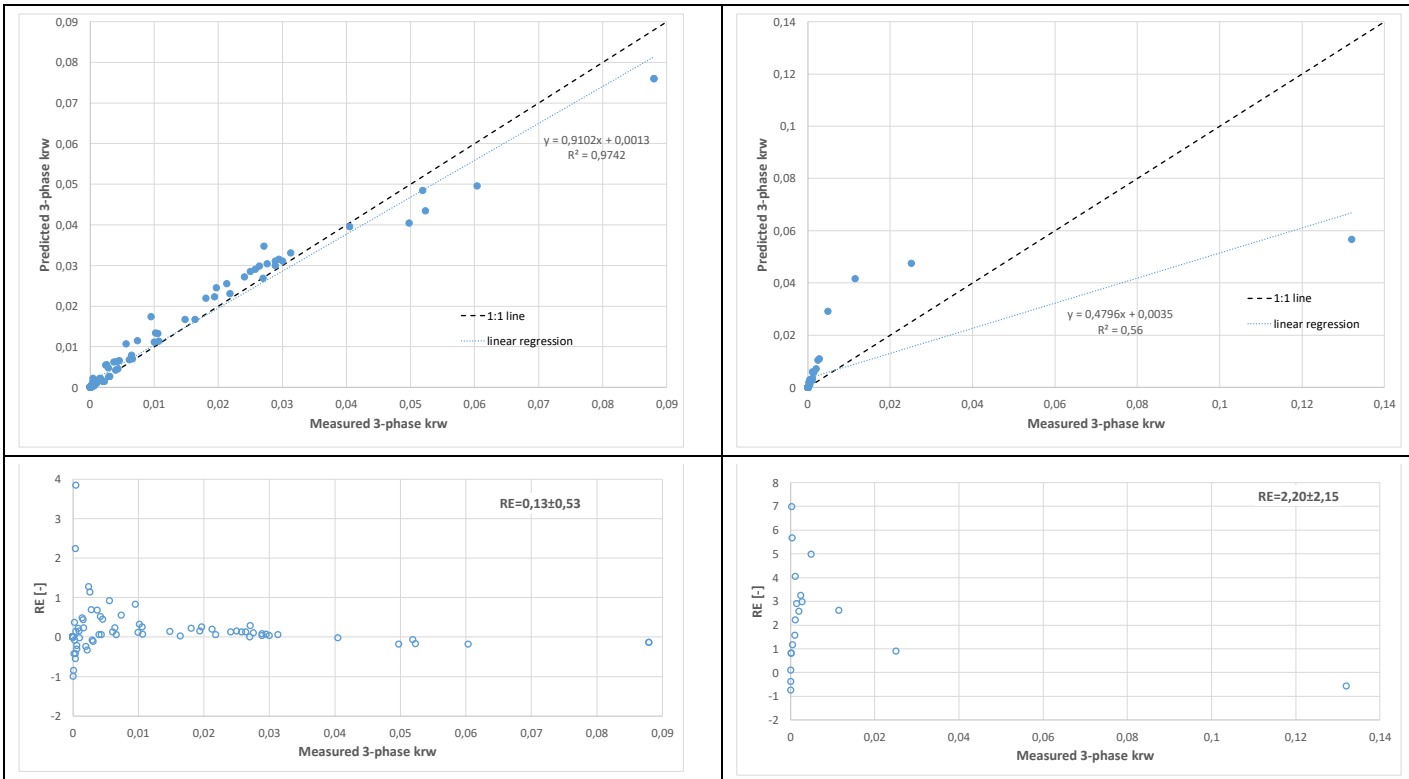

(a) (b)

Fig. 14. Cross-plot of the calculated three-phase water relative permeability against the measured three-phase water relative permeability and the associated relative error as function of measured water relative permeability: (a) Berea sandstone, (b) Bentheimer sandstone.

fitted regression line (R-squared=0.56). Except for a high measured water relative permeability, the mechanistic model largely overestimates the experimental data, up to a factor of 7 for low relative permeabilities. The average relative error is about 2.2 and the standard deviation of the relative error is 2.15.

For both sandstones, the cross-plot of calculated oil relative permeability against the measured oil relative permeability can be represented by the fitted regression line (Fig. 15), with a R-squared of 0.95 and 0.99.

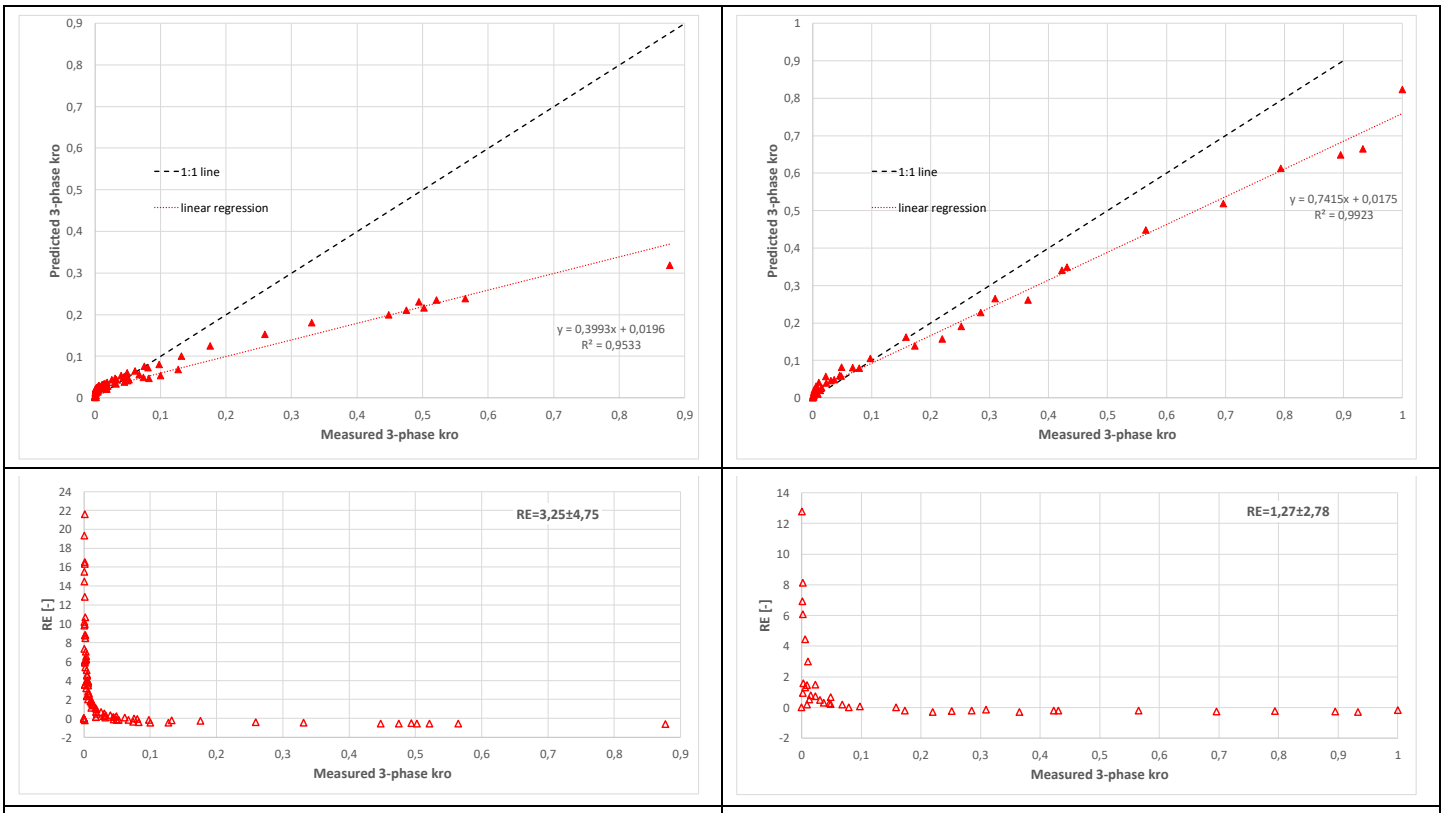

(a) (b)

Fig. 15. Cross-plot of the calculated three-phase oil relative permeability against the measured three-phase oil relative permeability and the associated relative error as function of measured oil relative permeability: (a) Berea sandstone, (b) Bentheimer sandstone.

The cross-plot for the three-phase oil relative permeability is characterized by two regions. For measured oil relative permeability below 0.1, the predicted permeabilities are significantly higher than those observed, attaining k_r values 10 times or more. For measured oil relative permeabilities higher than 0.1, the oil relative permeabilities predicted by the mechanistic model are about 60 and 25% lower than the measured k_r values in the case of Berea sandstone and Bentheimer sandstone, respectively. However, the average relative errors were quantified to 3.25 (±4.75) for Berea sandstone and 1.27 (±2.78) for Bentheimer sandstone, respectively. The obtained global overestimate of measured oil relative permeabilities is clearly attributed to the weight of the large number of experimental data with oil relative permeabilities lower than 0.1.

Analyzing the fitted regression line of the cross-plot shown in Fig. 16, one could again conclude that the predicted gas relative permeabilities underestimated the measured data of the Berea sandstone and Bentheimer sandstone by about 10 and 30%, respectively; but the average relative error of about 1.69 (±6.71) quantified for the experimental data of Berea sandstone does not give the same conclusion. Apparently, the mechanistic model overestimates the low relative permeabilities measured in the experiment, even by factor of 10 and more. The large number of data close to the origin does not strongly influence the slope of the regression line but have a strong impact on the average relative error. In the case of Bentheimer sandstone, the maximum relative errors observed for the predicted gas relative permeability do not exceed 1.5 for the extremely low gas relative permeabilities measured in the experiment.

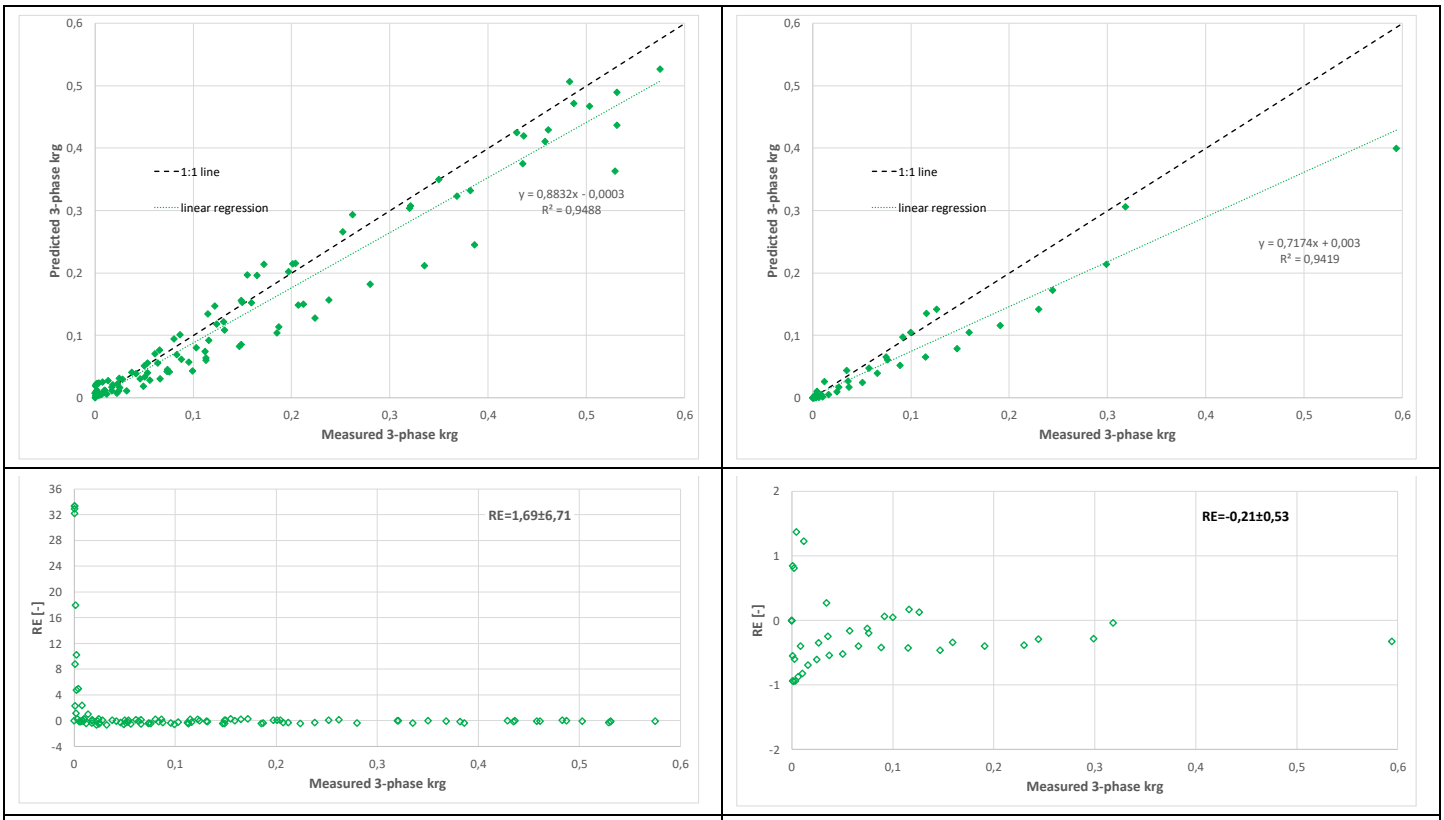

(a) (b)

Fig. 16. Cross-plot of the calculated three-phase gas relative permeability against the measured three-phase gas relative permeability and the associated relative error as function of measured gas relative permeability: (a) Berea sandstone, (b) Bentheimer sandstone.

4.2 Total Differential (TD) compatible model

4.2.1 Prediction of global mobilities

The TD compatible model introduced by di Chiara Roupert et al. (2010a, 2010b) quantifies in the first major step the global mobilities in the ternary diagram by numerical resolution of the Laplace equation. Note that on the three edges of the ternary diagram, the global mobilities are prescribed using the known individual phase mobilities in the two-phase systems. In the TD compatible model, the global mobility at saturation level s (s_1,s_3) and global pressure p are defined as follows:

$$d(s) = k_{r1}(s)d_1 + k_{r2}(s)d_2 + k_{r3}(s)d_3 \quad , \qquad (14)$$

where d_j and k_{rj} denote the mobility and relative permeability of phase j=1 (water), 2 (oil) and 3 (gas). Water and oil are supposed to be incompressible fluids, while the dynamic viscosities of the fluid phases (μ_j) are supposed to be constant and independent of the pressure level. Variation of gas density (ρ_3) with gas pressure (p_3) is taken into account in the computation of gas mobility. The phase mobilities are expressed by:

$$\begin{aligned} d_1 &= \frac{1}{\mu_1} \\ d_2 &= \frac{1}{\mu_2} \\ d_3 &= \frac{1}{\mu_3}\frac{\rho_3(p_3)}{\rho_3^{\circ}} \equiv \frac{1}{\mu_3}B_3 \end{aligned} \quad , \qquad (15)$$

Where ρ_3° is the gas density at reference pressure and B_3 is the volume factor.

In our study, we extended the original TD compatible model by integrating experimentally based residual saturations of the wetting fluid into two-phase systems. To numerically integrate the relative permeabilities of the non-wetting fluids into the three edges required for complete computation of the global mobilities on the edges, we linearly extrapolated the k_r values between the experimentally quantified maximum relative

permeability of the non-wetting fluid ($k_{rnw,max}$) and 1. An illustrative example of the modifications is shown in Fig. 17 for the oil-gas edge of Bentheimer sandstone.

In the following, we first discuss the application of the TD compatible model to the Bentheimer sandstone, then use the experimental data available for the Berea sandstone to test the prediction of global mobilities using the TD compatible model.

4.2.1.1 Bentheimer sandstone

Based on the model input parameter outlined in Appendix C1 and the fluid properties and experimental conditions of the DDI flow tests performed on Bentheimer sandstone (see section 3.2), the two-phase relative permeabilities and global mobilities on the three sides of the ternary diagram were quantified as shown in Fig. 17. To parameterize the required capillary pressure curves in a water-oil and oil-gas system, we used both the model parameters of the water retention curve in the water-gas system described in Appendix C1 and the scaling factors β_{ij} for the fluid system oil/water and gas/oil based on the measured interfacial tensions (fluid couples gas/water, oil/water and gas/oil) (see Table 2). To model the global mobilities on the ternary diagram, we used a spatial discretization of 0.01 saturation intervals. The simulated global mobilities are shown in Fig. 17 in form of iso-values ranging from 144 to 53650 mskg^{-1}.

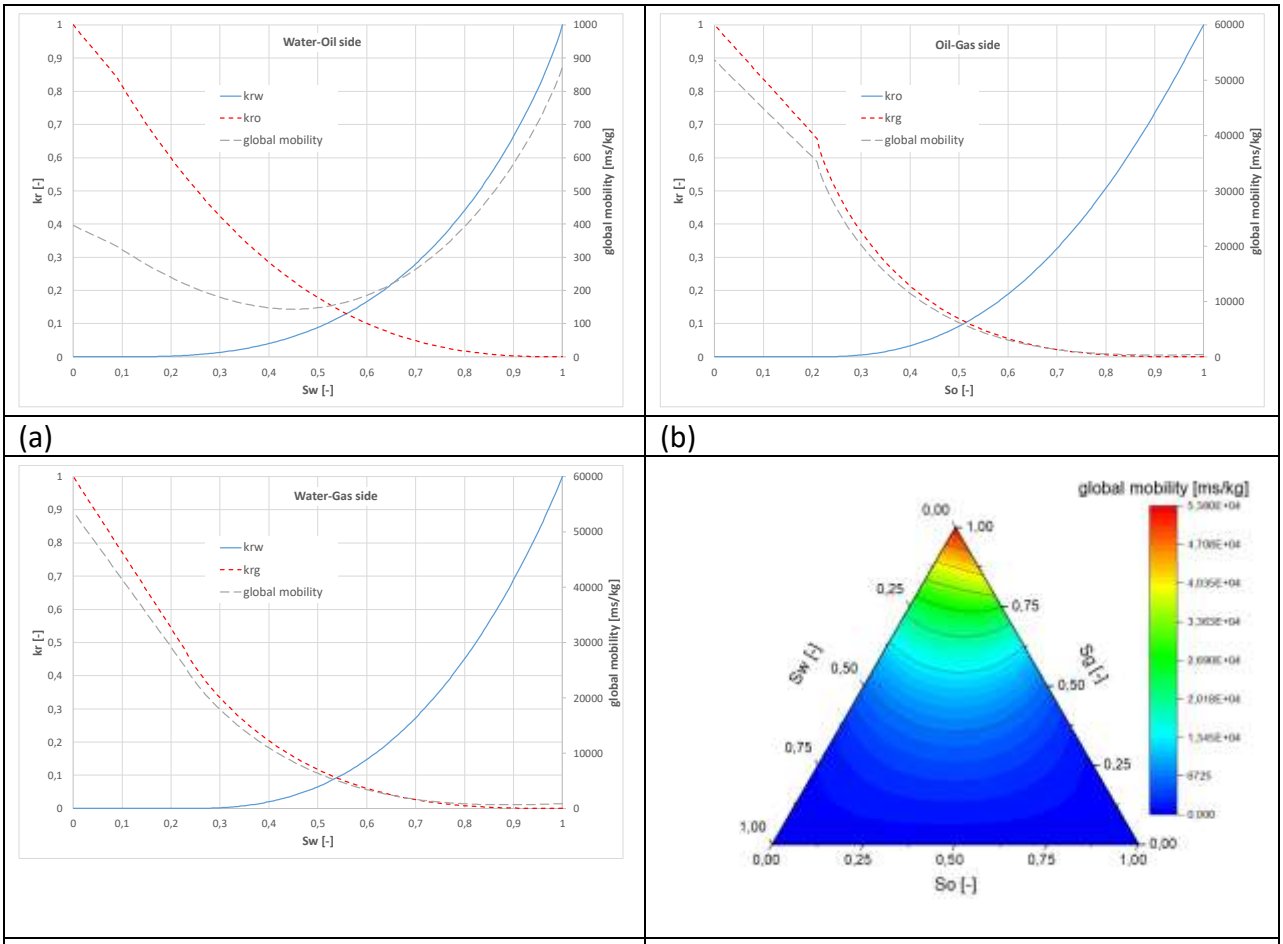

Fig. 17. Two-phase relative permeabilities and global mobilities applied to the water-oil (a), oil-gas (b) and water-gas (c) edge of the ternary diagram and global mobilities (d) quantified for the Bentheimer sandstone.

To compare the simulated global mobilities with the experimental data of the three DDI flow Experiments (A, C, and D1), we first extracted from our numerical results the global mobilities for the corresponding experimental saturations (S_1, S_2 and S_3). The experimental phase mobilities were then determined from Eq. 15 using the dynamic viscosities (Table 2). The variation of the volume factor B3 with gas pressure could be considered negligible. Nevertheless, we can infer from the resolution of the global capillary pressure on the

ternary diagram that the difference in gas pressure (p3) compared to the reference gas pressure of 55.157 atm is very small. The minimum gas pressure (water summit) was approximately 55.161 atm, while the maximum gas pressure (gas summit) was approximately 55.205 atm. Thus, the resulting volume factor of the gas B_3 (Eq. 15) varied between 0.99999 and 1.00082.

Fig. 18 shows the comparison of global mobilities predicted by the model and those experimentally determined from DDI Experiments A, C and D1. Apart from DDI Experiment D1, the simulated global mobilities strongly overestimate the experimental data. The relative error in DDI Experiment A is highest, with an approximate value of 8.26±9.16 (in Experiment C, RE=2.35±1.91). Its maximum relative error of 24 is observed for a gas saturation of 0.11. When approaching the gas summit, at $S_g = 0.57$, the relative error decreases to 1.2. Model predictions, however, are reasonably good in the area where water is under irreducible saturation. (DDI Experiment D1). The TD compatible model just slightly overestimates the experimental global mobilities. In this case, the relative error does not significantly decrease with increasing gas saturation and is quantified to be approximately 0.34±0.18.

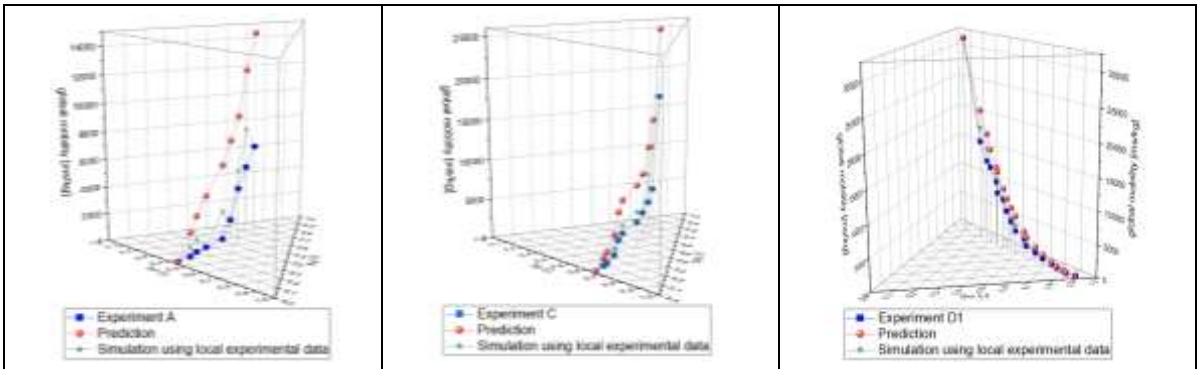

(a) (b) (c)

Fig. 18. Global mobilities predicted for the Bentheimer sandstone and compared to the experimental data of DDI Experiments A (a), C (b) and D1 (c)

4.2.1.2 Berea sandstone

Based on the model input parameter outlined in Appendix C.2 and the fluid properties and experimental conditions of the DDI flow tests performed on Berea sandstone (see section 3.2), the two-phase relative permeabilities and global mobilities on the three sides of the ternary diagram were quantified as shown in Fig. 19. To model the global mobilities on the ternary diagram, we used a spatial discretization of 0.01 saturation intervals. To parameterize the required capillary pressure curves for the water-oil and oil-gas system, we used the model parameters of the capillary pressure curve measured in the water-oil system. As the irreducible water saturation (S_{wi}) obtained in the two-phase flow experiments was higher than that obtained from the capillary pressure curve, we used the fit parameters obtained when S_{wi} was set to 0.26. We derived the scaling factor β_{go} required for the fluid system gas/oil from the ratio of parameters α quantified in the water-oil and oil-gas system which was about 1.67.

The simulated global mobilities are shown in Fig. 19 in form of iso-values ranging from 144 to 57112 $mskg^{-1}$. The maximum global mobilities determined at the gas summit are about 7% higher than those quantified for the Bentheimer sandstone. This is due to the maximum capillary pressures measured for Berea sandstone at irreducible wetting fluid saturation, which are approximately 10 times higher than those of Bentheimer sandstone. For the same reference pressure of 55.157 atm applied on the rock samples, the maximum gas pressures is achieved at the gas summit to 58.908 atm whereas at the water and oil summits the

corresponding gas pressures were calculated by the TD compatible model to about 55.157 and 55.329 atm, respectively. Thus the compressibility of the gas phase results in a volume factor B3 whose maximum value at the gas summit is about 1.068. However, for gas saturations below 0.6, the quantified volume factor B3 was below 1.003. The maximum gas saturation achieved in Oak's DDI experiment is below 60%, and its effect on the computation of experimental global mobilities (see Eq. 15) can be ignored.

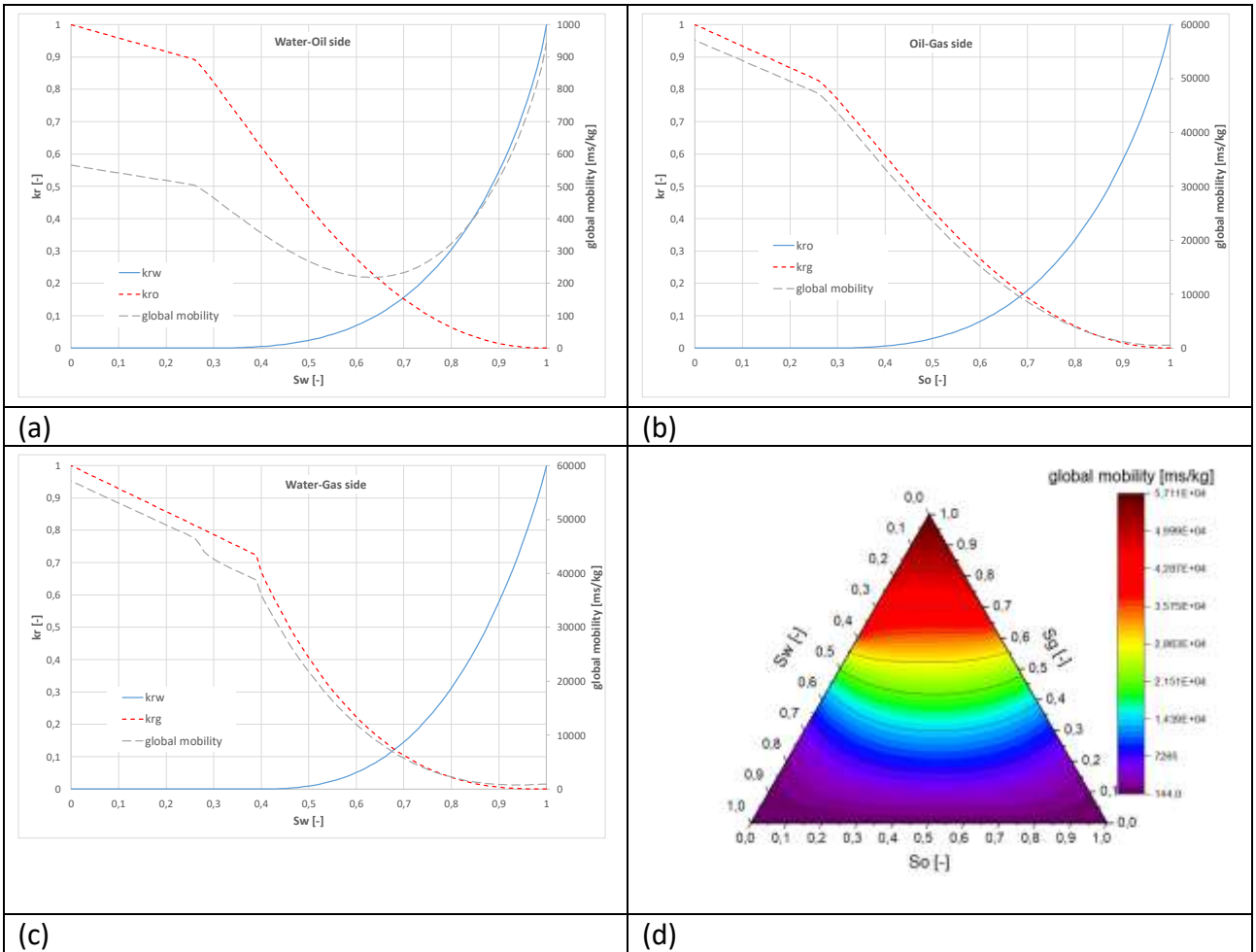

Fig. 19. Two-phase relative permeabilities and global mobilities applied to the water-oil (a), oil-gas (b) and water-gas (c) edge of the ternary diagram and global mobilities (d) quantified for the Berea sandstone.

After extracting the global mobilities corresponding to the experimental data of the seven DDI flow experiments, the numerical results were compared with the experimentally determined global mobilities (Fig. 20). The same general trend was observed for Bentheimer sandstone: the predictions overestimate the observations, and with increasing gas saturations, the differences become acceptable. For low gas saturations, up to 30 or 35%, the simulated global mobilities strongly overestimate the experimental data by a factor of 2 and more. For example, in the case of DDI Experiment 15, the maximum relative error was quantified to about 8.3 for a measured gas saturation of about 13%, whereas for a gas saturation of 59% the relative error decreased to about 0.3. The highest average relative error was quantified for the prediction of global mobilities of Experiment 25 (RE=24.07±31.89).

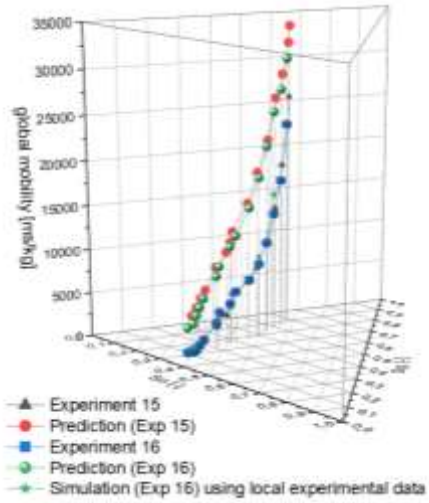

(a)

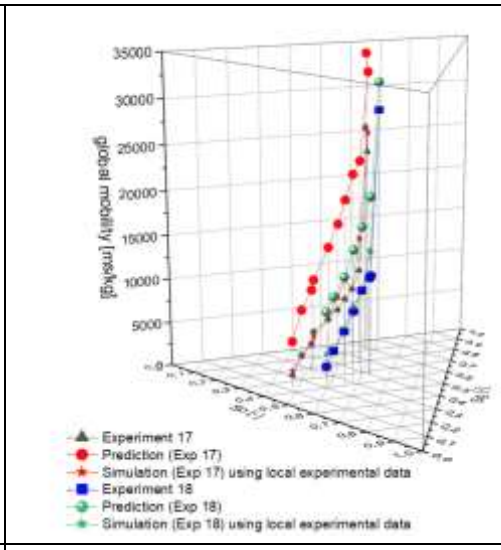

(b)

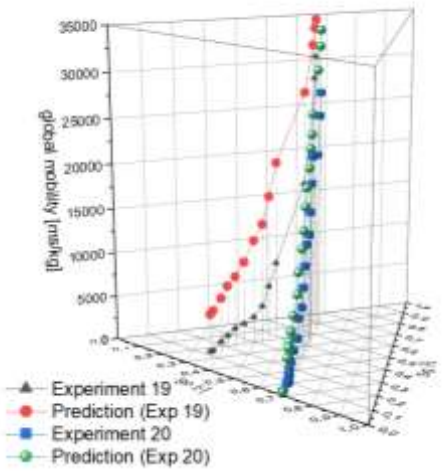

(c)

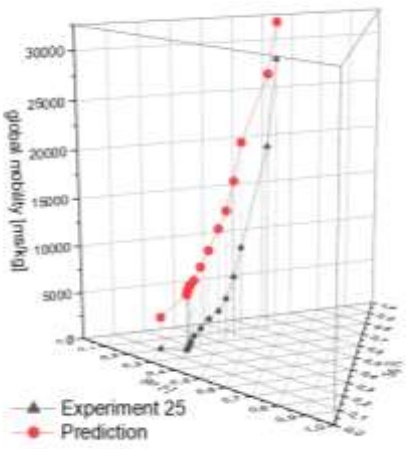

(d)

Fig. 20. Global mobilities predicted for the Berea sandstone and those obtained from the experimental data of DDI Experiments 15 and 16 (a), 17 and 18 (b), 19 and 20 (c) and 25 (d)

4.2.2 Prediction of global mobilities using local experimental data

In both test cases, the predicted global mobility overestimates the actual physical values. To obtain values close to the experimental global mobilities, we partially "constrained" the model of three-phase permeabilities, respecting the condition of Total Differential with regard to measurements. Therefore, we implemented the possibility of imposing locally, inside the ternary diagram, global mobilities derived from experimental data in the interpolation by finite elements C0. The use of other two-dimensional interpolation models of global mobilities between the numerical values given at the edges of the ternary diagram, such as the Lagrange interpolation polynomials, was not considered as a very promising improvement over the current interpolation method, since the predictions are well above the experimental data.

In order to constrain our interpolation method, we used one third of the experimental data available for the Bentheimer and Berea sandstone DDI experiments to measure local global mobility uniformly distributed within the ternary diagram. The resulting “improved” global mobilities will then be used, based on Equation 4, to predict the three-phase relative permeabilities (water, oil, gas) for Bentheimer sandstone and Berea sandstone (Section 4.2.3).

4.2.2.1 Bentheimer sandstone

The improved global mobilities obtained for Experiments A, C and D1 are shown in Fig. 18. Using locally prescribed mobilities derived from 13 measuring points, the relative errors of the simulated mobilities

obtained for Experiment A, C and D1 are significantly reduced but still overestimate the experimental data. In the case of Experiment A and C, the relative error is now approximately 2.30±3.67 and 0.49±0.58, respectively, whereas the relative error for the predicted mobilities of Experiment D1 becomes very low (RE=0.07±0.09). Note that Experiment D1 corresponds to a saturation path where water is at irreducible saturation, and thus parallel to the gas-oil edge of the ternary diagram.

4.2.2.2 Berea sandstone

The improved global mobilities obtained for Experiments 16, 17 and 18 are shown in Fig. 20. Using locally prescribed mobilities derived from 34 measuring points, the relative errors of the simulated mobilities obtained for Experiments 15-20 and 25 are reduced but still largely overestimate the experimental data. For example in the case of Experiment 16, the relative error is now approximately 0.12 ±0.30 instead of 2.74±2.67 whereas the average relative error for the predicted mobilities of Experiment 20 is also reduced from RE=1.94±2.39 to RE=0.15±0.32. Note that the highest average relative error of simulated global mobilities is still observed in Experiment 25, which is however significantly reduced by a factor of approximately 16 (RE=1.49±3.90).

4.2.3 Prediction of relative permeabilities in a three-phase system

The numerical construction of the global capillary pressure P_c^g is performed by finite elements C1 ("step 5" described in Table 1) using bi-Laplacian interpolation of the global capillary pressure prescribed on edges *ij* of the ternary diagram; where tangential and normal derivatives of P_c^g are, respectively fixed as Dirichlet and Neuman boundary conditions (Appendix E). To quantify the global capillary pressure on the ternary diagram, we used a spatial discretization of 0.01 saturation intervals.

Based on the TD compatibility condition introduced by Chavent (2009), two inequalities have to be respected (di Chiara Roupert et al., 2010):

$$\begin{gathered} \beta^{13}(t) - (P_c^{12}(1-t) - P_c^{12}(0) \le \beta^{23}(t) \le \beta^{13}(t) \quad (a) \\ \beta^{13}(t) - P_c^{32}(t) \le \beta^{12}(t) \le \beta^{13}(t) \qquad (b) \end{gathered} \tag{16}$$

where β^{ij} is the global capillary pressure on edges ij of the ternary diagram, P_c^{12} and P_c^{32} are the capillary pressure in a two phase water-oil and gas-oil system, respectively, and t is the saturation parameter varying between zero and one.

The water fractional flow (f_1) and gas fractional flow (f_3) are obtained from the derivatives of the global capillary pressure function (p_c^g) and the derivatives of capillary functions P_c^{12} and P_c^{32} (di Chiara Roupert et al., 2010a):

$$\begin{aligned} f_1(s,p) &= \frac{\partial P_c^g}{\partial s_1}(s,p) \cdot \left(\frac{dP_c^{12}(s_1)}{ds_1}\right)^{-1} \\ f_3(s,p) &= \frac{\partial P_c^g}{\partial s_3}(s,p) \cdot \left(\frac{dP_c^{32}(s_3)}{ds_3}\right)^{-1} \end{aligned} \tag{17}$$

The oil fractional flow (f_2) is then quantified using the expression:

$$f_2(s,p) = 1 - f_1(s,p) - f_3(s,p)\,. \tag{18}$$

Using the phase mobilities (d_j), global mobility (d) and fluid fractional flows (f_j), calculated for a given water saturation (s_1) and gas saturation (s_3), the relative permeabilities to water, oil and gas are then derived from Equation 4.

4.2.3.1 Bentheimer sandstone

The analyses of the two inequalities described by Equation 16 are presented in Appendix E. Both conditions are evaluated as functions of t and shown in form of a comparison of three curves (Fig. E2, Appendix E). While

condition (b) is respected for all saturation parameters t, condition (a) is only satisfied for t≤0.78. For t values higher than 0.78, $\beta^{23}(t)$ is higher than $\beta^{13}(t)$. Note that the irreducible water saturation (S_{wir}) in the two-phase water-gas system was quantified to 0.22. Here, the TD compatible model is not applicable for gas saturations higher than ($1-S_{wir}$). We therefore modified the numerical approach originally introduced by di Chiara Roupert et al. (2010a). Instead of solving the biharmonic problem over the entire ternary diagram, in our computation, we omitted the immobile water zone near the gas summit. Along this new border, the limit value of β^{13} (t=0.78) on each node of the mesh is fixed as known Dirichlet boundary value of the global capillary pressure and its corresponding normal derivative belonging to the border. The biharmonic problem of step 5 (Table 1) is solved using HCT finite elements at the given experimental global pressure level of p=55.16 atm (corresponding to 800 psig). In our simulations, we used small saturation intervals of 0.005 to produce a sufficiently smooth map of the global capillary pressure function P_c^g and its two derivatives with respect to s_1 and s_3 (Equation 17). Once the three maps are calculated, the water and gas fractional flows (f_1 and f_3) are then derived using Equation 17. Fig. 21 shows the results of two numerical studies performed: (a) the so-called "predicted" distribution of the global capillary pressure and the derived fractional flows of water and gas, (b) the corresponding "simulated" distributions when using 13 local experiments based on water and gas fractional flows. The 13 local points selected are the same points as in the previous global mobilities studies. While on the three edges of the ternary diagram and their neighborhood, the water and gas fractional flows reflect the prescribed physical values of the two-phase systems. In the ternary diagram, however, they appear as zones of unphysical values. When approaching the water summit, the water fractional flows exceeds locally the maximum value of 1 and, simultaneously, the gas fractional flow is below 0. A similar effect, but more pronounced in form of an elongated bump is observed for the distribution of the gas fractional flow when approaching the gas summit: the gas fractional flows largely exceed the physical upper limit of 1, while the water gas fractional flow become locally negative.

It is worth noting here that the distribution of P_c^g is not significantly modified when using locally prescribed water and gas fractional flows. Observing closely, P_c^g differs only locally, in the neighborhood of the 13 "fitting" points, at maximum by about 35 Pa and is thus not visible in the chosen colormap of P_c^g. However, the maps of f_1 and f_3 are locally adjusted to the physical conditions of the DDI experiments, which is visible in Fig. 21b. This helped to locally reduce the height of the "bump of f_3". Therefore, and to be consistent with the improvement achieved in the case of global mobilities, the numerical results obtained with modeling approach (b) were further considered.

The relative permeabilities to water, oil, and gas are then obtained from the TD compatible model using Equation 4. Fig. 22 shows the comparison of relative permeabilities measured from Experiment C with those predicted by the TD compatible model. The detailed comparison of predicted k_r values (water, oil, gas) for Experiments A and D1 with those experimentally measured is documented in Appendix E (Figs. E3 and E4).

In view of the fact that f_2 is derived from f_1 and f_3 according to equation 18, it is not surprising that the majority of the predicted relative permeabilities of oil is not physical. The high positive value of CRM also indicates that the TD compatible model largely underestimates the measurements. As the water and gas fractional flows predicted for DDI Experiment C are mostly positive, we can use both global mobilities and fractional flows, to compare the measured water relative permeabilities and gas relative permeabilities with those predicted. The predicted water relative permeabilities largely overestimate the measured values. In addition, in the case of Experiment C, the tendency of decreasing water relative permeabilities with increasing water saturation is not consistent with the laws of physics. However, in the case of Experiment A (Fig. E3), the predicted "positive" water relative permeability increases with water saturation. The prediction of gas relative permeabilities is rather acceptable with the TD compatible model. As shown in Figs. 22, E3 and E4, the predicted gas relative permeabilities increase with gas saturation but still overestimate the experimentally measured values by a factor of approximately 1.5 to 2.

Global capillary pressure	Water fractional flow	Gas fractional flow
(a)		
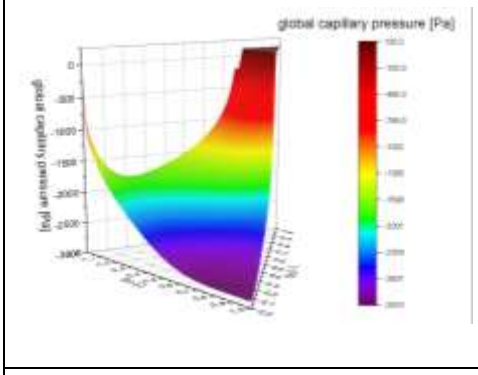	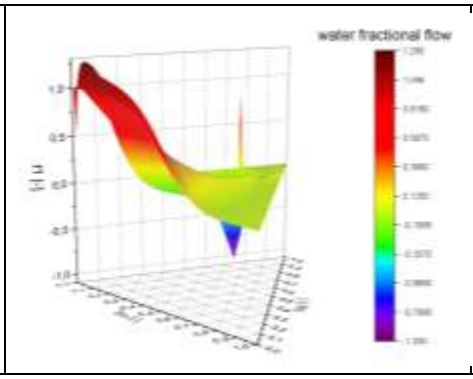	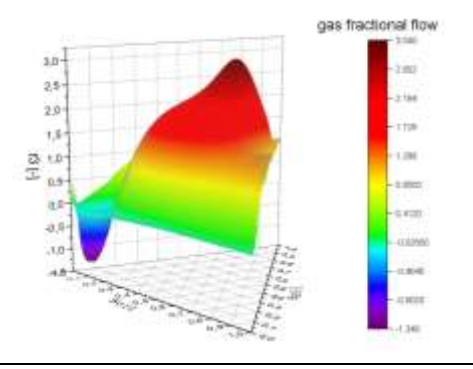
(b)		
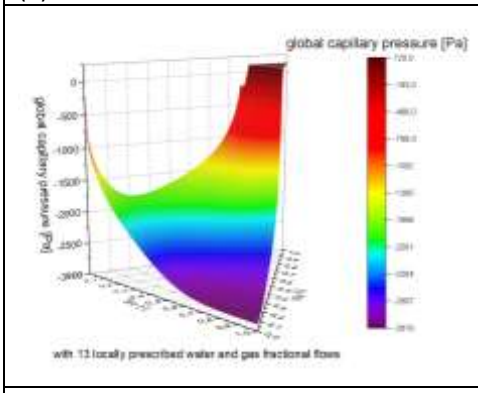	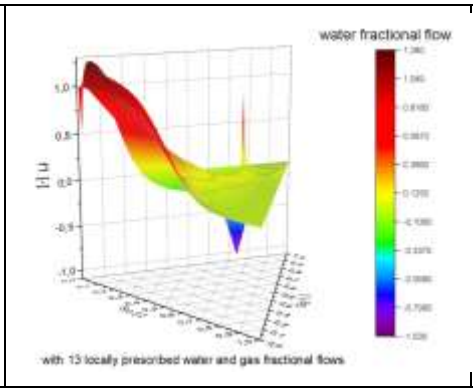	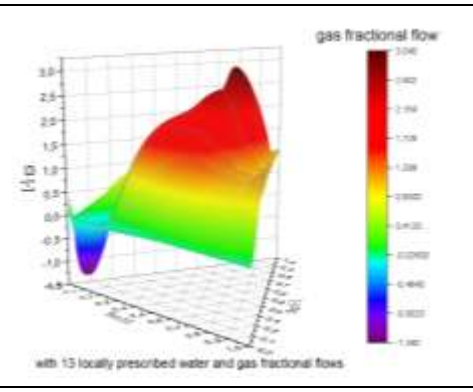

Fig. 21. Bentheimer sandstone: Global capillary pressure, water fractional flux, gas fractional flux predicted (a) and simulated (b) using 13 experimentally derived fractional flow of water and gas.

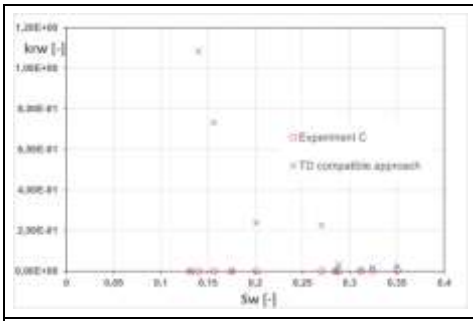	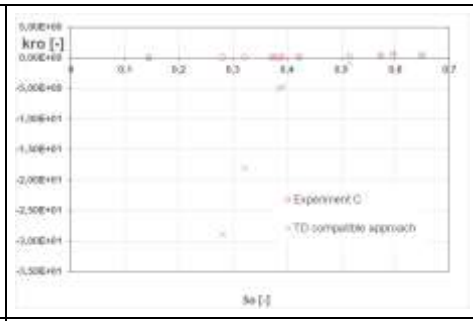	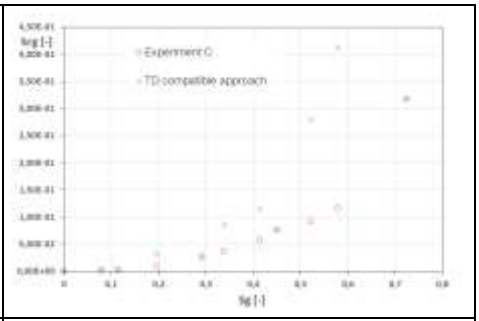
(a) RMSE= 0.1227; CRM=-289.09	(b) RMSE=3.1687; CRM=38.29	(c) RMSE=0.0329; CRM=-0.85

Fig. 22. Relative permeabilities measured from Alizadeh's DDI Experiment C compared to those predicted by the TD compatible model: (a) water relative permeability versus water saturation, (b) oil relative permeability versus oil saturation, and (c) gas relative permeability versus gas saturation.

4.2.3.2 Berea sandstone

The analyses of the two inequalities described by Equation 16 are presented in Appendix E. Both conditions are evaluated as functions of t and shown in form of a comparison of three curves (Fig. E.5). While condition (b) is respected for all saturation parameters t, condition (a) is only satisfied for t≤0.62. For t values higher than 0.62, $\beta^{23}(t)$ is higher than $\beta^{13}(t)$. Note that the irreducible water saturation (S_{wir}) in the two-phase water-gas system was quantified to 0.38. Here, the TD compatible model is not applicable for gas saturations higher than ($1-S_{wir}$). We then applied the same choices for this inner boundary (close to the gas summit) and solved the biharmonic problem of step 5 (Table 1) as described in section 4.2.3.1.

Fig. 23 illustrates the results of calculated distribution of the global capillary pressure and the derived fractional flows of water and gas, using 34 local experiment based water and gas fractional flows. The chosen 34 local points are the same as in the previous global mobilities studies.

Global capillary pressure	Water fractional flow	Gas fractional flow
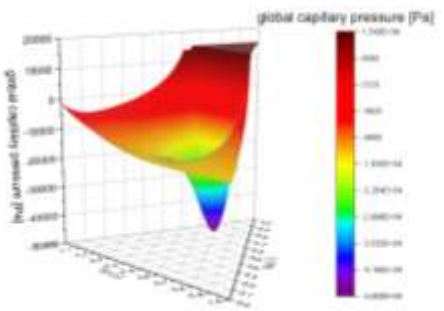	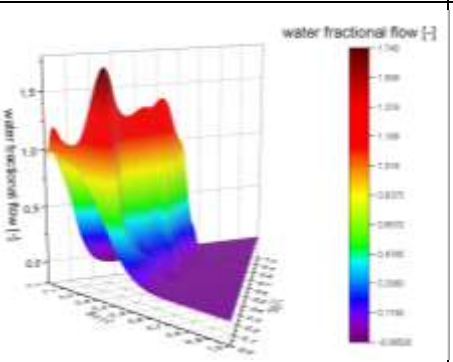	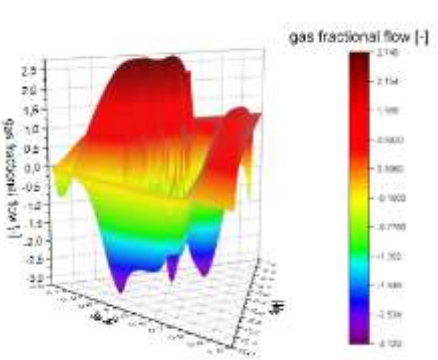

Fig. 23. Berea sandstone: Calculated global capillary pressure, water fractional flux, gas fractional flux using 34 experimentally derived fractional flow of water and gas.

Here the global capillary pressures prescribed along the three edges of the ternary diagram vary between -20000 and 15000 Pa due to the high capillarity of Berea sandstone. Compared to Bentheimer sandstone, the difference between the minimum and maximum value of P_c^g is approximately ten times higher than in the previous study. In contrast to Fig. 21, the obtained distribution shows a strong local decrease of P_c^g, funnel shaped, in the middle of the ternary diagram. This results in high negative values of gas fractional flow. In addition, as already observed for the Bentheimer sandstone, an elongated bump along the water-gas side appears when approaching the gas summit. The calculated distribution of water fractional flow is smoother than in the case of Bentheimer sandstone. However, the physical upper limit of 1 is exceeded (with a maximum value of 1.7) in regions along the water-gas side and close to the water summit.

Since the quantified gas fractional flows are significantly below or above the physical limits of 0 and 1, respectively, a further interpretation of the gas fraction in terms of gas relative permeabilities is not possible. Therefore, as in the case of Bentheimer sandstone, the relative oil permeabilities in the three-phase system is not likely to be determined. The only possible interpretation is therefore limited to the quantification of relative water permeabilities (using Equation 4) as the water fractions determined represent physical values, except for a small area in the diagram.

The calculated water relative permeabilities are compared with the experimental data of DDI Experiments 15 (Fig. 24) and Experiments 18 (Fig. 25). The detailed comparison of predicted water relative permeabilities for Experiments 16, 17, 19 and 25 with those experimentally measured is documented in Appendix E (Figs. E6 and E7).

Generally, the measured water relative permeabilities are largely overestimated by the TD compatible model. The majority of the predicted values clearly exceed the physical upper limit of 1, which is mainly due to the water fractional flow determined, some of which are two orders of magnitude higher than the experimental fractional water flows. This is clearly shown, for example, in the case of DDI experiment 15 (Fig. 24). In this case, the physical upper limit of the water fractional flow of 1 is not exceeded, but the water relative permeability clearly exceeds the maximum value of 1. For example, at a water saturation of 0.32, the water fractional flow is about 0.182, which highly overestimates the experimental value (f_1=0), and the calculated ratio of global mobility to water mobility (d/d_1) is about 27. The product of f_1 and (d/d_1) then gives the high, physically unrealistic numerical value of 4.92 for water relative permeability. As shown in Fig. 25, the predicted ratios of global mobility to the water mobility are relatively close to the experimentally determined ratios.

In the case of Experiment 18 the predicted water relative permeabilities are obviously below 1, but in addition, as in the other DDI experiments, the experimentally determined water relative permeabilities are clearly

exceeded (Fig. 25). The residual mass coefficient (CRM) calculated here is -439, which clearly demonstrates the overestimation of the measured values. It should be noted that the global mobilities estimated are rather similar to the measured values.

(a)

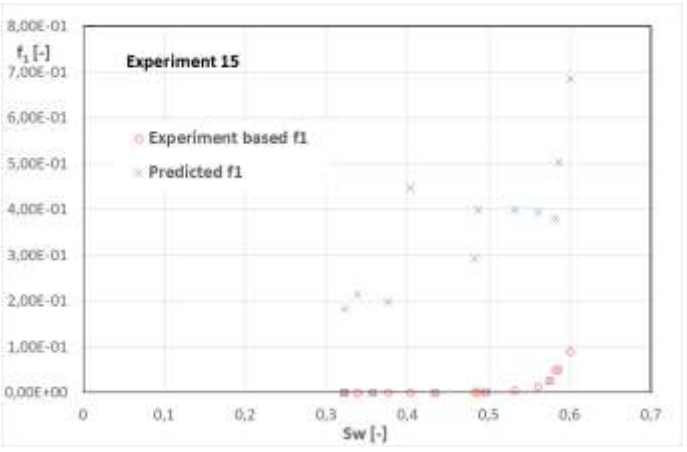

(b)

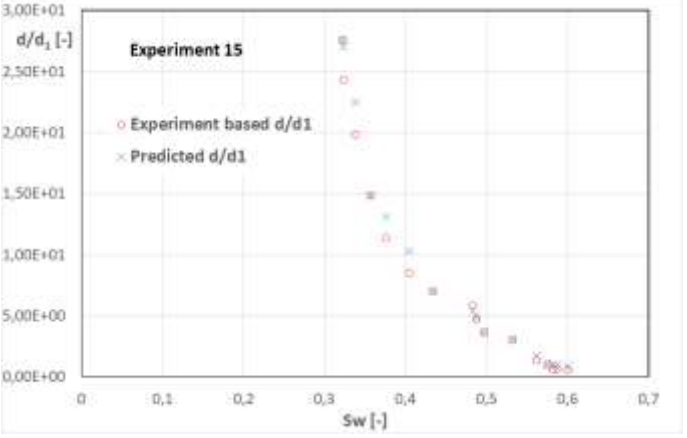

(c)

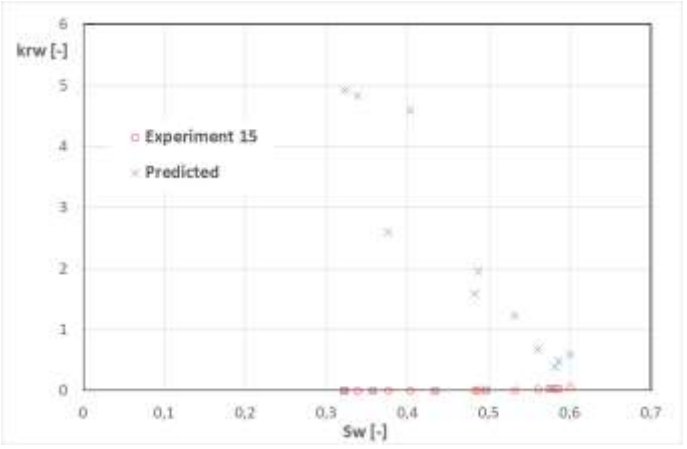

RMSE= 0,574; CRM=-129.54

Fig. 24. Fractional water flows (a), ratios of global mobility to water mobility (b) and water relative permeabilities (c) measured from Oak's DDI Experiment 15 compared to those predicted by the TD compatible model.

(a)

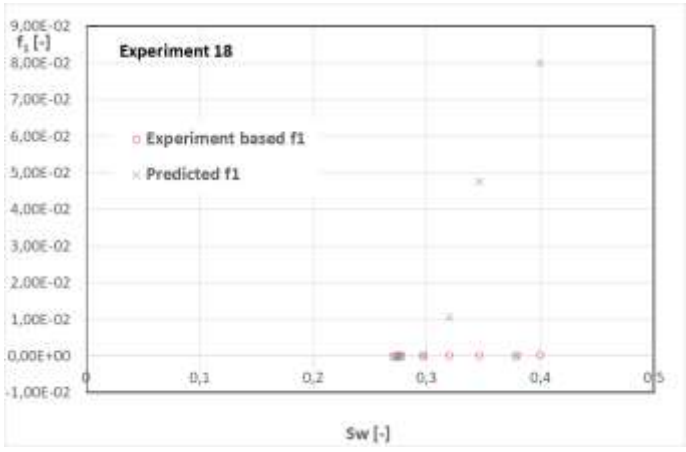

(b)

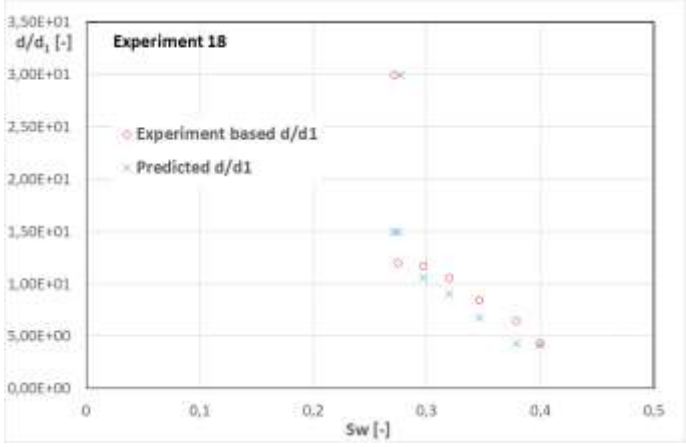

(c)

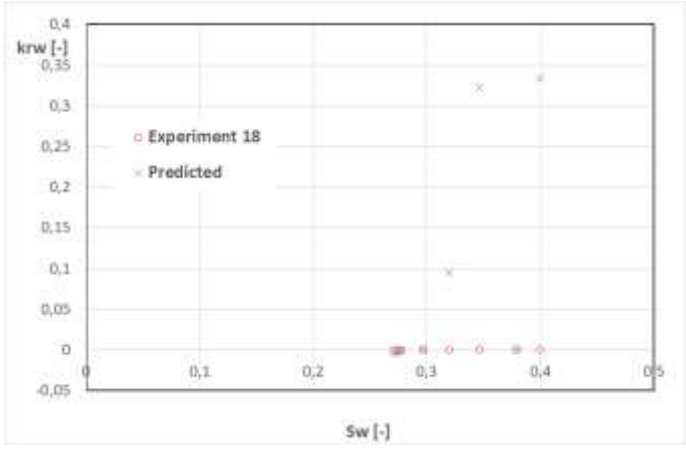

RMSE= 0.059; CRM=-493.09

Fig. 25. Fractional water flows (a), ratios of global mobility to water mobility (b) and water relative permeabilities (c) measured from Oak's DDI Experiments 18 compared to those predicted by the TD compatible model.

4.3 Parker-Lenhard model

4.3.1 Application to Bentheimer sandstone

Table 8 summarizes the model input parameter used for the application of the Parker-Lenhard model to the Bentheimer sandstone. They were obtained by nonlinear fit of the Van Genuchten (1980) model to Alizadeh's capillary pressure curve measured for soil sample B in a water-gas system (R-Squared (COD)=0.986) or by nonlinear fit of the Mualem-Van Genuchten model to Alizadeh's experimental water relative permeability-water saturation curve (R-Squared=0.994) (see Appendix F.1). Note, in the latter case, m was the only fit parameter as the irreducible water saturation S_{wi} was fixed and taken equal to the experimentally determined value.

Table 8. Model input parameter used for the prediction of DDI experiments performed on Bentheimer sandstone (Alizadeh, 2013).

Approach using	Run	S_{wi} [-]	m [-]	α [Pa^{-1}]
P_c-S_w	Option Pc-S	0.111	0.810	1.96×10^{-4}
k_{rw}-S_w	Option kr-S	0.234	0.972	-

Fig. 26 shows the comparison of relative permeabilities measured from Experiment C with those predicted by the Parker-Lenhard model for both modeling options. The detailed comparison of predicted k_r values (water, oil, gas) for Experiments A and D1 with those measured by Alizadeh (2013) is documented in Appendix F.

Globally, the relative permeabilities to water, oil and gas, predicted with both modeling options overestimate the measured k_r values (Fig. 26, Annexe F (Figs. F2 and F3)). The best prediction of the water relative permeability is achieved with option kr-S which results in lowest RMSE values and smallest negative coefficients of residual mass (CRM). Note that in the case of Experiment D1, which is conducted at irreducible water saturation, both modeling options satisfactorily predict the measured water relative permeabilities. The oil relative permeabilities predicted by modeling option Pc-S still overestimate the experimental data but are generally closer to the measured k_r values than modeling option kr-S. Surprisingly, the measured gas relative permeabilities are strongly overestimated by both modeling options. As shown in Figs. 26, F.2 and F.3, the predicted relative permeabilities to gas are rather close to each other and overvalue the experimentally quantified permeabilities, also for Experiment D1, by a factor of 2 to 3. This is even surprising as the oil relative permeability for Experiment D1 is satisfactorily predicted by both modeling options.

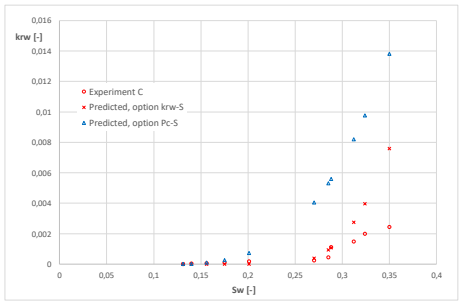

(a) Option kr-S : RMSE= 0.000516; CRM=-1.051

Option Pc-S : RMSE= 0.00113515; CRM=-4.887

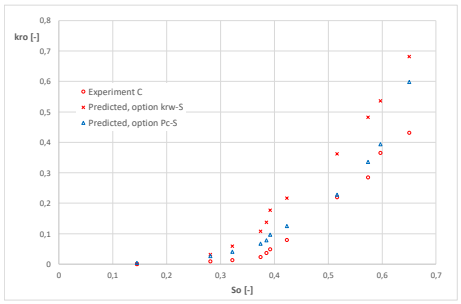

(b) Option kr-S : RMSE=0.04132; CRM=-0,849

Option Pc-S : RMSE= 0.018387; CRM=-0.321

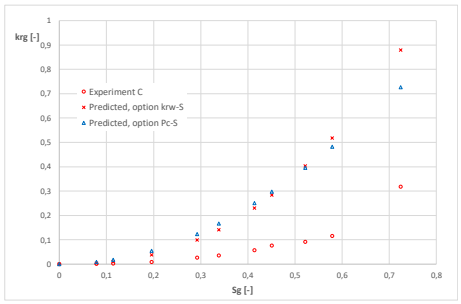

(c) Option kr-S : RMSE=0.074049; CRM=-2.553

Option Pc-S : RMSE=0,064833; CRM=-2.440

Fig. 26. Relative permeabilities measured from Alizadeh's DDI Experiment C compared to those predicted (using option kr-S and option Pc-S): (a) water relative permeability versus water saturation, (b) oil relative permeability versus oil saturation, and (c) gas relative permeability versus gas saturation.

4.3.2 Application to Berea Sandstone

Table 9 summarizes the model input parameter used for the application of the Parker-Lenhard model to the Berea sandstone. They were obtained by nonlinear fit of the Van Genuchten (1980) model to Oak's capillary pressure curve measured for soil sample 6 in a water-gas system (R-Square (COD)=0.995) or by nonlinear fit of

the Mualem-Van Genuchten model to Oak's experimental water relative permeability-water saturation curve (R-Square=0.972) (see Appendix F.2). Note, in the latter case, m was the only fit parameter as the irreducible water saturation Swi was fixed and taken equal to the experimentally determined value.

Table 9. Model input parameter used for the prediction of DDI experiments performed on Berea sandstone (Oak, 1990).

Approach using	Run	S_{wi} [-]	m [-]	α [Pa^{-1}]
P_c-S_w	Option Pc-S	0.147	0.324	8.05×10^{-5}
k_{rw}-S_w	Option kr-S	0.384	0.912	-

The numerical results obtained for the Berea sandstone are shown in Fig. 27 and in Appendix F2. Globally, using modeling option kr-S, the relative permeabilities for water, oil and gas are overestimated by both modeling options. Modeling option Pc-S underestimates the measured water relative permeabilities, and except for Experiments 19 and 25, also the oil relative permeability; whereas the gas relative permeability is globally overestimated. The water and gas relative permeabilities predicted by modeling option kr-S are closer to the measured k_r values than with modeling option Pc-S as underlined by the RMSE values. However, the oil relative permeabilites are better predicted with modeling option Pc-S than with modeling option krw. As shown in Fig. 27, in the case of Experiment 15, modeling option Pc-S strongly overestimates the measured gas relative permeability whereas the oil relative permeability is underestimated by the modeling approach. In the latter case, here a better prediction with lower RMSE is obtained than with modeling option kr-S. The quantified coefficient of residual mass (CRM) also indicates that the measured values are only slightly underestimated whereas a strong overestimation is observed with option kr-S. The detailed comparison of predicted k_r values (water, oil, gas) for Experiments 16-20, 25 with those measured by Oak (1990) is documented in Appendix F.

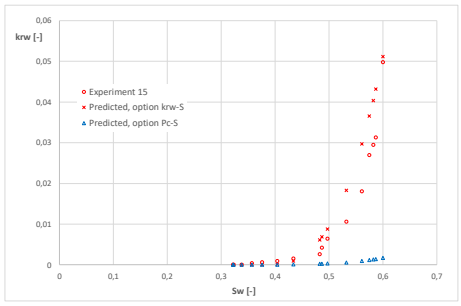

(a) Option kr-S : RMSE= 0.001495; CRM=-0.322

Option Pc-S : RMSE= 0.004477; CRM=0.957

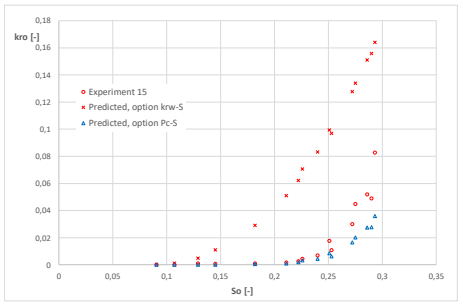

(b) Option kr-S : RMSE=0.017291; CRM=-3.073

Option Pc-S : RMSE= 0.004031; CRM=0.497

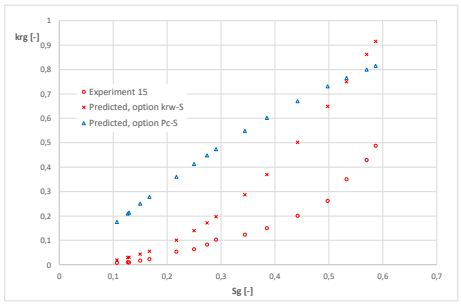

(c) Option kr-S : RMSE=0.058371; CRM=-1.156

Option Pc-S : RMSE=0.087431; CRM=-2.266

Fig. 27. Relative permeabilities measured from Oak's DDI Experiment 15 compared to those predicted (using option kr-S and option Pc-S): (a) water relative permeability versus water saturation, (b) oil relative permeability versus oil saturation, and (c) gas relative permeability versus gas saturation.

4.3.3 Global analysis of predicted three-phase relative permeabilities

For further investigation of the accuracy of the model, the three-phase relative permeabilities predicted by the model for each fluid phase are plotted against the measured relative permeabilities obtained for Berea and Bentheimer sandstone (Figs. 28-30). Each figure also contains a description of the quantified relative error as a function of the measured relative permeability in the three-phase system.

In the case of Berea sandstone, as shown by the cross-plot (Fig. 28), the water relative permeability is reasonably well predicted by model option kr-S. Globally, it slightly overestimates the measured kr values characterized by a relative error of about 0.13± 0.72. It is worthwhile to note that for relative permeabilities

higher than 0.04, the predicted values closely approaches the measured relative permeabilities. However, model option Pc-S strongly underestimates the measured water relative permeabilities (RE=-0.96±0.02) for the whole set of experimental data. In the case of Bentheimer sandstone, model option kr-S also seems as the better option to predict the measured water relative permeabilities. Here, both options overestimate the experimental data (RE=0.85±1.85 (kr-S), RE=4.72±3.86 (Pc-S)). The deviation from the 1:1 line is high for measured water relative permeabilities lower than 0.01; in the case of modeling option Pc-S the maximum relative error achieves values higher than 15.

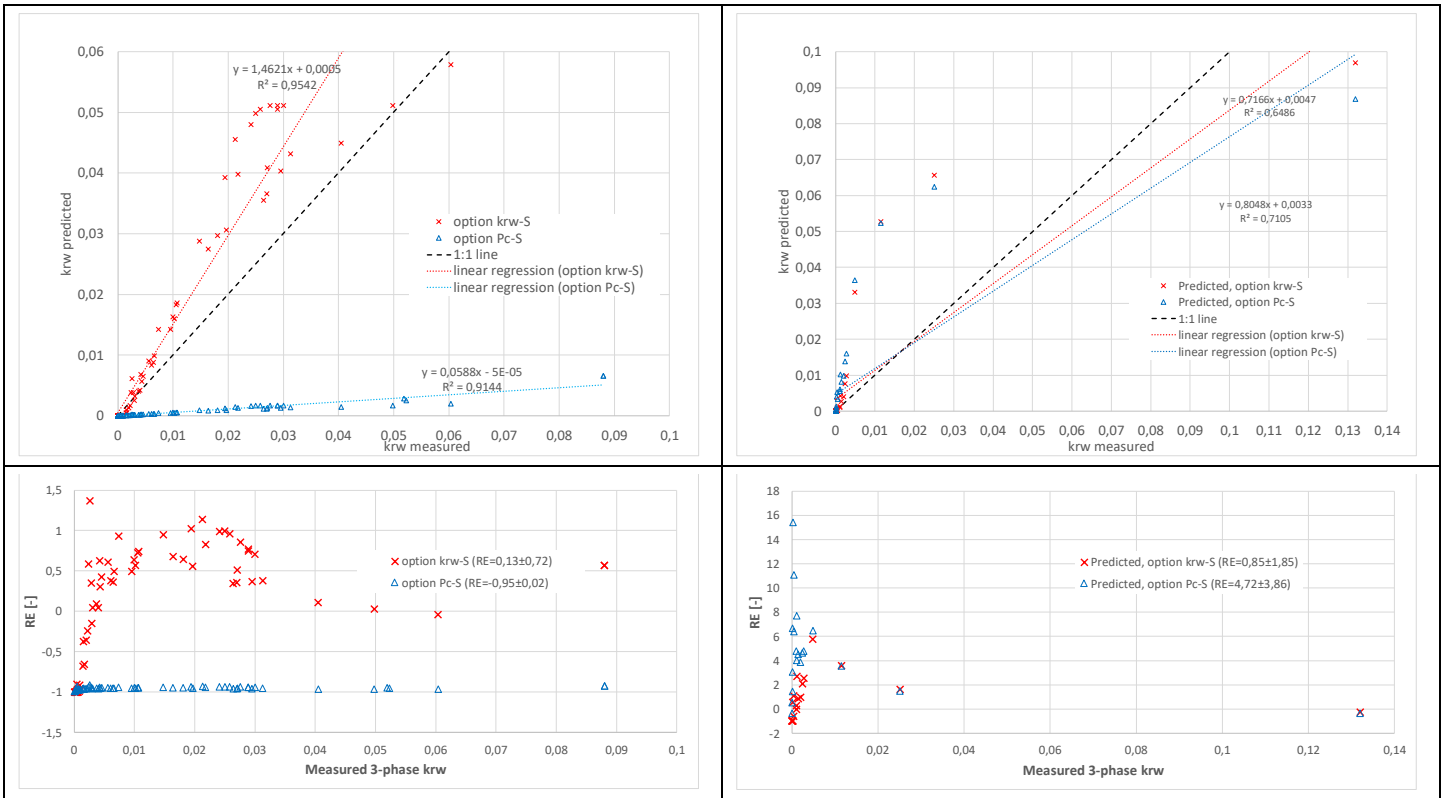

(a) (b)

Fig. 28. Cross-plot of the calculated three-phase water relative permeability against the measured three-phase water relative permeability and the associated relative error as function of measured water relative permeability: (a) Berea sandstone, (b) Bentheimer sandstone.

The oil relative permeabilities predicted for the Berea sandstone (Fig. 29) show the same general trend as observed for the water relative permeabilities: modeling option kr-S overestimates and modeling option Pc-S underestimates the measured relative oil permeabilities. However, here, modeling option kr-S strongly overestimates the experimental data characterized by a large spreading around a high mean relative error (RE=12.59±15.65) whereas modeling option Pc-S seems to be the best option for predicting the experimental data (RE=-0.16±0.90) even if the deviation from the 1:1 line increases with increasing measured oil relative permeabilities. In the case of Bentheimer sandstone, both modeling options again overestimate the measured oil relative permeabilities (RE=7.01±15.66 (kr-S), RE=3.80±7.59 (Pc-S)). It is worth noting here that the deviation of predicted oil relative permeabilities from the experimental data is also high for very low oil relative permeabilities (<0.01). They attain maximum relative errors of up to 80 and 40 for modeling option kr-S and modeling option Pc-S, respectively. Globally, the best results are obtained with modeling option Pc-S. It satisfactorily predicts the experimental data, as shown by the small deviations from the 1:1 line, when the measured relative permeabilities exceed 0.05.

Using the Parker-Lenhard model, the gas relative permeabilities predicted for Berea sandstone and Bentheimer sandstone strongly overestimate the measured gas relative permeabilities (Fig. 30). The relative errors of the prediction are quantified to 5.64±17.16 (kr-S) and 38.75±128.63 (Pc-S) for Berea sandstone, and 3.16±3.29 (kr-S) and 4.41±5.41 (Pc-S) for Bentheimer sandstone, respectively. As already mentioned before, the maximum relative errors appear for very low relative permeabilities (<0.01). In the case of Berea

sandstone, the maximum relative errors attain values of 1000 (option kr-S) and 100 (option Pc-S) whereas for Bentheimer sandstone achieve values of about 26 (option kr-S) and 14 (option Pc-S). Even for higher relative permeabilities measured for both sandstones, the predicted gas relative permeabilities overestimate globally the experimental data at least by a factor of 2.

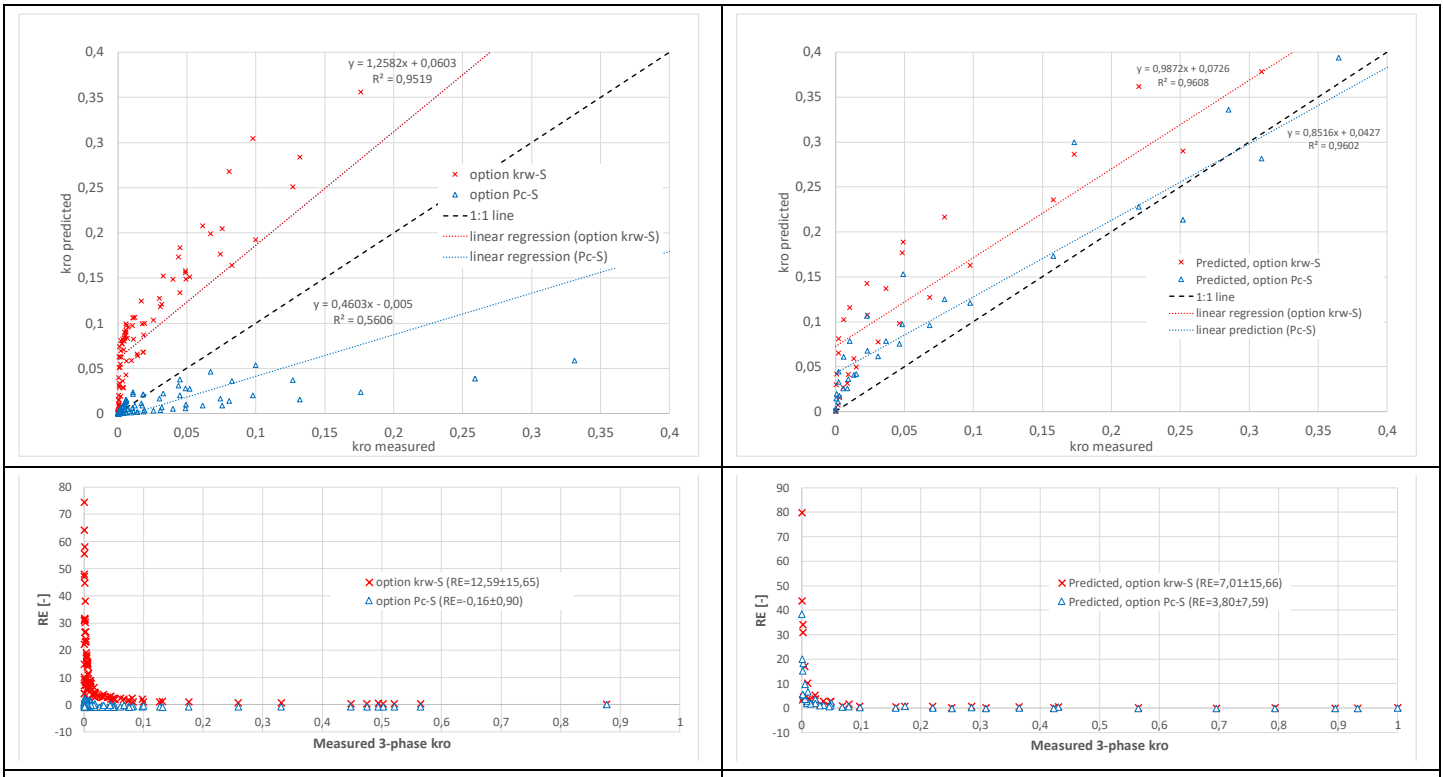

(a) (b)

Fig. 29. Cross-plot of the calculated three-phase oil relative permeability against the measured three-phase oil relative permeability and the associated relative error as function of measured oil relative permeability: (a) Berea sandstone, (b) Bentheimer sandstone.

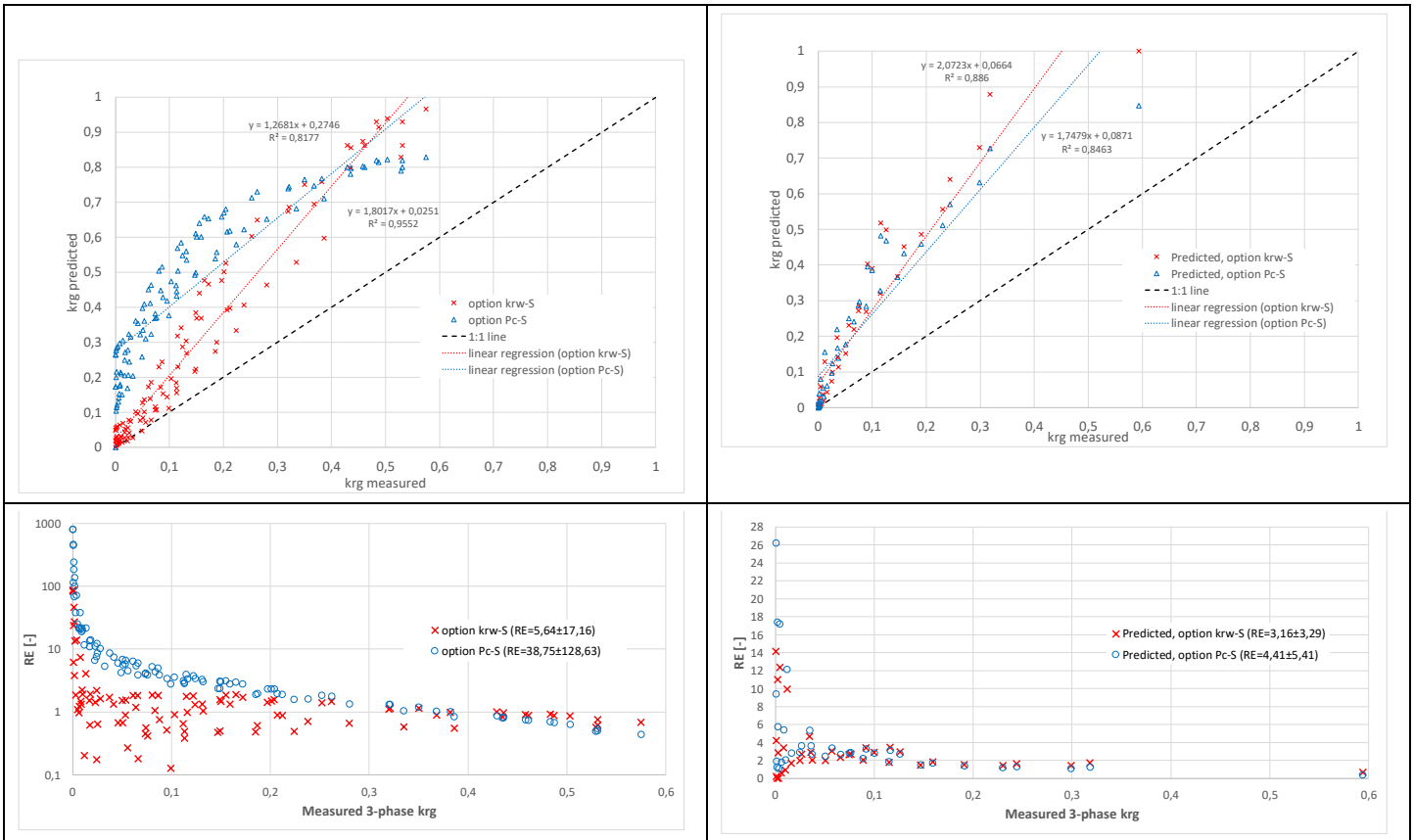

(a) (b)

Fig. 30. Cross-plot of the calculated three-phase gas relative permeability against the measured three-phase

gas relative permeability and the associated relative error as function of measured gas relative permeability: (a) Berea sandstone, (b) Bentheimer sandstone.

4.4 Stone's Model I

The numerical simulations performed with Stone's model I concern only the oil relative permeability in a three-phase system. Table 10 summarizes the model input parameter used for the application of Stone's model I to the Bentheimer sandstone and Berea sandstone. They were obtained by nonlinear fit of the Mualem-Van Genuchten model (Van Genuchten, 1980) to the experimental two-phase (gas-oil, oil-water) relative permeability-saturation curves measured for Bentheimer sandstone (Alizadeh, 2013) and Berea sandstone (Oak, 1990) (see Appendices C.1 and C.2).

Table 10. Model input parameter used for the prediction of DDI experiments performed on Bentheimer sandstone (Alizadeh, 2013) and Berea sandstone (Oak, 1990).

	Gas-Oil system		Oil-Water system		
Rock sample	S_{or} [-]	m_{og} [-]	S_{wi} [-]	m_{ow} [-]	$k_{row,max}$ [-]
Bentheimer sandstone	0.207	1.036	0.089	1.021	0.841
Berea sandstone	0.259	0.845	0.264	0.847	0.892

4.4.1 Application to Bentheimer sandstone

Fig. 31 shows the comparison of predicted oil relative permeability versus oil saturation with those measured in DDI Experiments A, C and D1 (Alizadeh, 2013). Here, the average model prediction errors are acceptable: the RMSE values vary between 0.0108 (Experiment A) to 0.0218 (Experiment C). Surprisingly, the oil relative permeabilities measured in Experiments C and D1 are reasonably well predicted by Stone's model I.

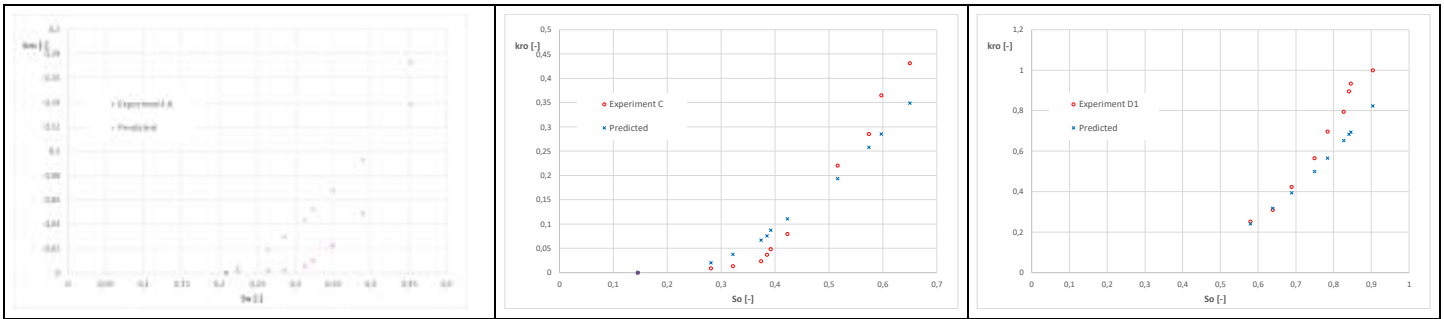

(a) RMSE= 0.0108; CRM=-0.685 | (b) RMSE=0.0132; CRM=0.018 | (c) RMSE= 0.0218; CRM= 0.103

Fig. 31. Oil relative permeabilities versus oil saturation measured on Bentheimer sandstone compared to those predicted by Stone's model I: (a) Experiment A, (b) Experiment C, and (c) Experiment D1.

Here, the coefficients of residual mass (CRM) range between -0.685 and 0.103. In the case of Experiment A, Stone's model overestimates globally the measured oil relative permeability, by up to a factor of 4 to 8 at oil saturations close to the residual oil saturation.

4.4.2 Application to Berea sandstone

Fig. 32 shows the comparison of predicted oil relative permeability versus oil saturation with those measured in DDI Experiments 15-20, and 25 (Oak, 1990). The agreement of the predicted relative oil permeabilities with the measurement results is relatively good for Experiments 15, 16, 17, and 20. Larger deviations are observed especially in Experiments 19 and 25. The reason for the strong underestimation of the measured oil permeabilities (CRM=1) is that the Stone 1 model sets the relative permeabilities for all oil saturations smaller than the residual saturations (S_{or}=0.259) to zero.

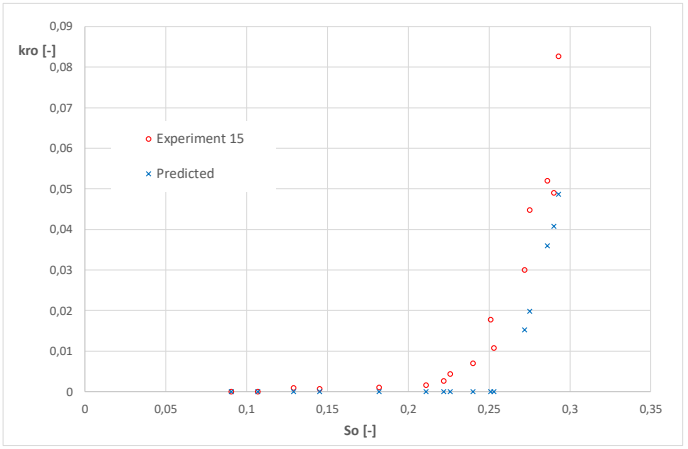

(a) RMSE= 0.0033; CRM= 0.474

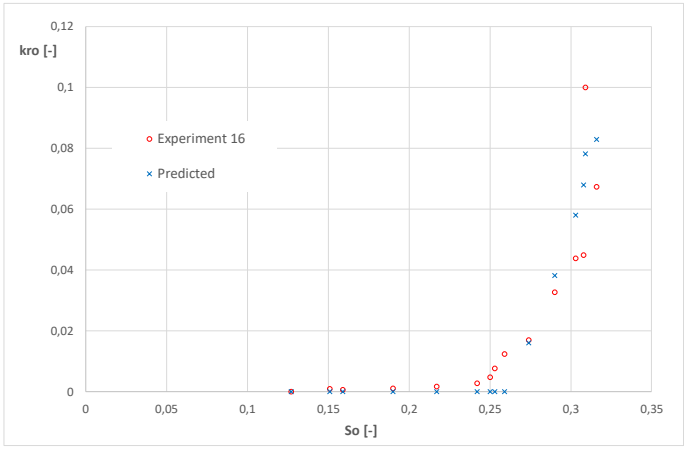

(b) RMSE= 0,0028; CRM= -0.011

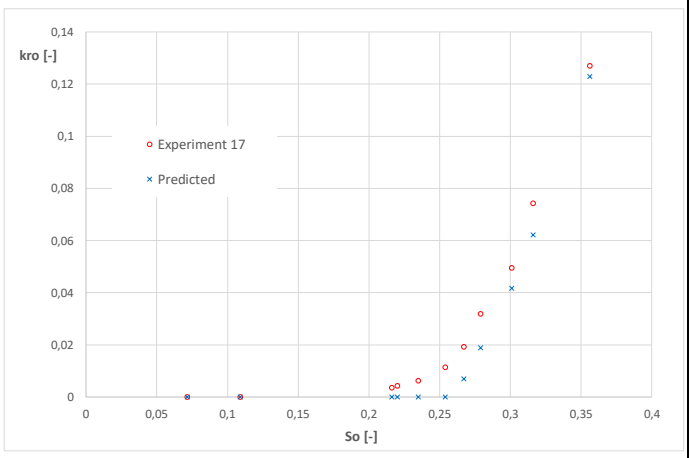

(c) RMSE= 0.0025; CRM= 0.228

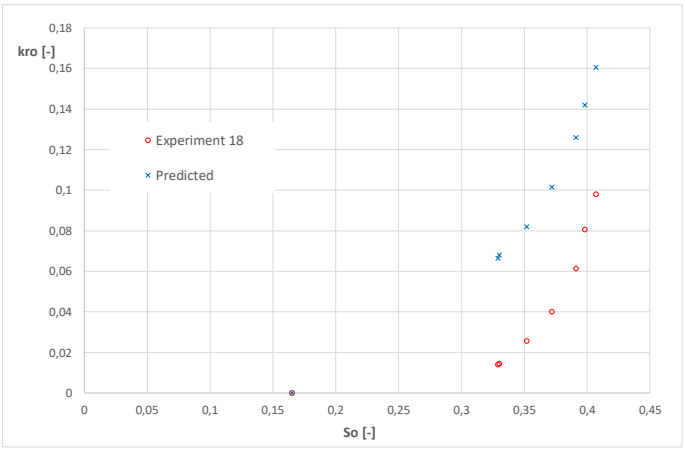

(d) RMSE= 0.0195; CRM= -1.232

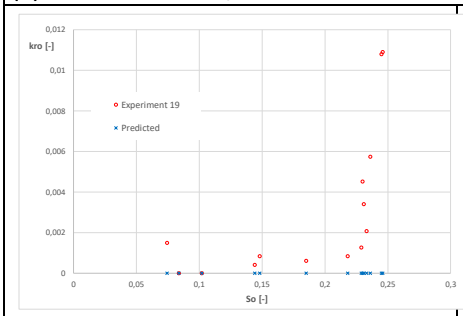

(e) RMSE= 0.0013; CRM= 1.000

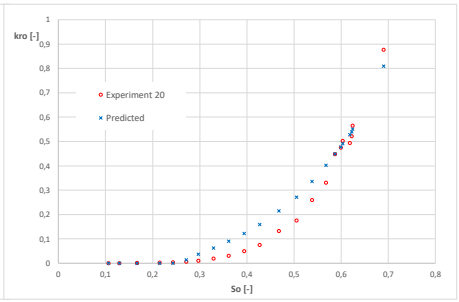

(f) RMSE= 0.0104; CRM= -0.116

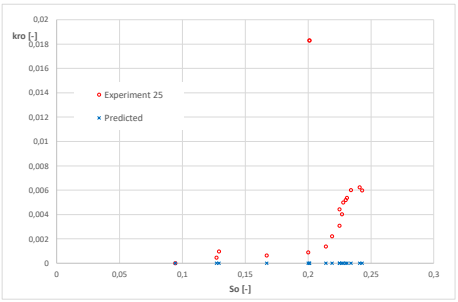

(g) RMSE=0.0017; CRM=1.0

Fig. 32. Oil relative permeabilities versus oil saturation measured on Berea sandstone compared to those predicted by Stone's model I: Experiments 15 (a), 16 (b), 17 (c), 18 (d), 19 (e), 20 (f) and 25 (g).

4.4.3 Cross-plot of oil relative permeabilities predicted by Stone's model I against the experimental three-phase k_r values measured on Berea and Bentheimer sandstone

For further investigation of the accuracy of Stone's model I, the three-phase oil relative permeability predicted by the model is plotted against the experimental oil relative permeability measured for Berea and Bentheimer sandstone (Fig. 33). The figure also contains a description of the quantified relative error as a function of the measured oil relative permeability in the three-phase system.

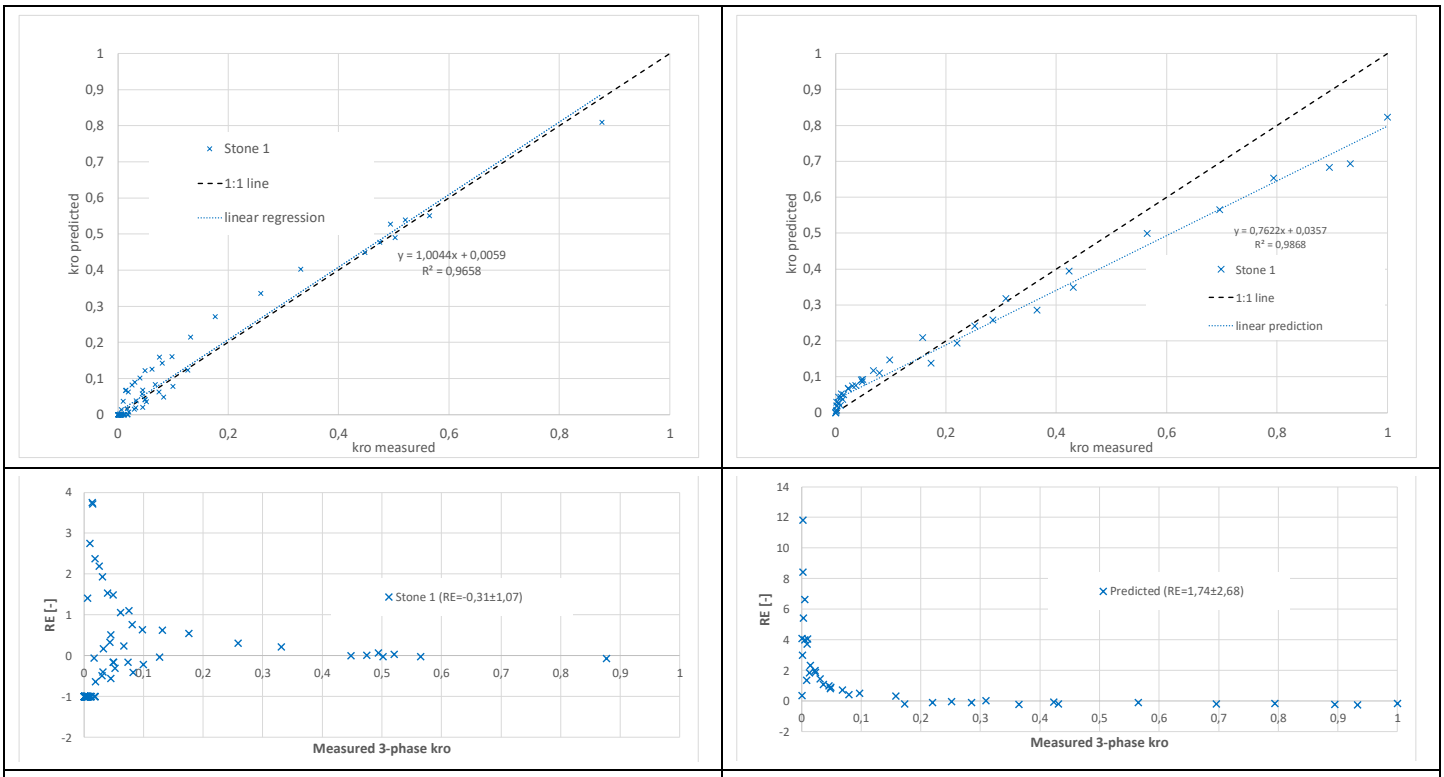

(a) (b)

Fig. 33. Cross-plot of the calculated three-phase oil relative permeability against the measured three-phase oil relative permeability and the associated relative error as function of measured oil relative permeability: (a) Berea sandstone, (b) Bentheimer sandstone.

In the case of Berea sandstone, as shown by the cross-plot (Fig. 33), the oil relative permeability is reasonably well predicted by Stone's model 1. Globally, it slightly underestimates the measured k_r values characterized by a relative error of about -0.31±1.07. The highest relative errors are observed for very low oil relative permeabilities, attaining a maximum relative error of about 4 at a measured relative permeability of 0.01. It is worthwhile to note that for relative permeabilities higher than 0.3, the predicted values closely approaches the measured relative permeabilities. Here, the scatterplot of predicted k_r values against the measured data can be described by a linear regression (R-squared=0.966) whose slope is close to one.

The oil relative permeabilities predicted for Bentheimer sandstone show a different behavior than Berea sandstone: here, the simulation based on Stone's model I significantly overestimates the measured relative oil permeabilities with a high average relative error and an associated large variance (RE=1.74± 2.68). Just as the Berea sandstone, the maximum relative errors appear at low values of measured oil relative permeability. However, for higher values of experimental relative permeability, for example above 0.2, the predicted oil relative permeabilities systematically underestimate the measured values by about 25% and are well described by the fitted straight line of linear regression (R-squared = 0.987).

5. Discussion

5.1 Global analysis of predicted three-phase relative permeabilities

For further evaluation of the accuracy of the 4 different models used to predict three-phase relative permeabilities measured in DDI experiments conducted on Bentheimer and Berea sandstones, the relative errors (RE) identified in the previous section are summarized in Table 11 individually for each fluid phase. In the following, the main results presented in Table 11 will be discussed with respect to each of the three phase relative permeabilities.

Table 11. Overview on the determined relative errors (RE) and uncertainty intervals (standard errors) of the mathematical models used for the prediction of the relative permeabilities in the 3-phase fluid system

		Mechanistic model	TD compatible model	Parker-Lenhard model		Stone's Model I
Water relative permeability	Berea sandstone	0.13±0.53	762±1774	kr-S	0.13±0.72	
				Pc-S	-0.96±0.02	
	Bentheimer sandstone	2.20±2.15	2102±6664	kr-S	0.85±1.85	
				Pc-S	4.72±3.86	
Oil relative permeability	Berea sandstone	3.25±4.75	not quantifiable	kr-S	12.95±15.65	-0.31±1.07
				Pc-S	-0.16±0.90	
	Bentheimer sandstone	1.27±2.78	not quantifiable	kr-S	7.01±15.66	1.74±2.68
				Pc-S	3.80±7.59	
Gas relative permeability	Berea sandstone	1.69±6.71	not quantifiable	kr-S	5.64±17.16	
				Pc-S	38.75±128.63	
	Bentheimer sandstone	0.21±0.53	1.39±2.97	kr-S	3.16±3.29	
				Pc-S	4.41±5.41	

5.1.1 Three-phase water relative permeability

In the case of Berea sandstone, the water relative permeability is reasonably well predicted by the mechanistic model. Globally, it slightly overestimates the measured k_r values. Nonetheless, for the Bentheimer sandstone, the predicted water relative permeabilities varies significantly from the experimental measurements. Except for a high measured water relative permeability, the mechanistic model largely overestimates the experimental data, up to a factor of 7 for low relative permeabilities. The average relative error is about 2.2 and the standard deviation of the relative error is 2.15.

The TD compatible model provided quantifiable results on water relative permeabilities. The water relative permeabilities measured on both Bentheimer sandstone and Berea sandstone are highly overestimated by the TD compatible model, with the corresponding relative errors being very large.

Using the Parker-Lenhard model, the water relative permeability measured for the Berea sandstone was reasonably well predicted by model option kr-S. Globally, it slightly overestimates the measured k_r values. It should be noted that for relative permeabilities higher than 0.04, the predicted values closely approaches the measured relative permeabilities. However, model option Pc-S strongly underestimates the measured water relative permeabilities for the entire set of experimental data. In the case of Bentheimer sandstone, model option kr-S also seems the better option to predict the measured water relative permeabilities. In this case, both options overestimate the experimental data. In the case of modeling option Pc-S, the maximum relative error achieves values higher than 15.

5.1.2 Three-phase oil relative permeability

Using the mechanistic model, the predicted oil relative permeabilities are partially acceptable. For measured oil relative permeability below 0.1, the predicted permeabilities are significantly higher than those observed, attaining k_r values 10 times or more. For measured oil relative permeabilities higher than 0.1, the oil relative permeabilities predicted by the mechanistic model are about 60 and 25% lower than the measured k_r values

in the case of Berea sandstone and Bentheimer sandstone, respectively. However, the relative errors were quantified to 3.25±4.75 for Berea sandstone and 1.27±2.78 for Bentheimer sandstone, respectively. The obtained global overestimate of measured oil relative permeabilities is clearly attributed to the weight of the large number of experimental data with oil relative permeabilities lower than 0.1.

The oil relative permeabilities predicted for the Berea sandstone using the Parker-Lenhard model show similar trend as those for the water relative permeabilities: modeling option kr-S overestimates and modeling option Pc-S underestimates the measured relative oil permeabilities. However, here, modeling option kr-S strongly overestimates the experimental data characterized by a large spreading around a high mean relative error whereas modeling option Pc-S seems as the best option for predicting the experimental data. In the case of Bentheimer sandstone, both modeling options again overestimate the measured oil relative permeabilities. It should be noted here that the deviation of predicted oil relative permeabilities from the experimental data is also high for very low oil relative permeabilities (<0.01). They attain maximum relative errors of up to 80 and 40 for modeling option kr-S and modeling option Pc-S, respectively. Globally, the best results are obtained with modeling option Pc-S.

It was shown that in the case of Berea sandstone, the oil relative permeability is reasonably well predicted by Stone's model 1. Globally, it slightly underestimates the measured k_r values. The highest relative errors are observed for very low oil relative permeabilities, attaining a maximum relative error of about 4 at a measured relative permeability of 0.01. The oil relative permeabilities predicted for Bentheimer sandstone show a different behavior than Berea sandstone: here, the simulation based on Stone's model I significantly overestimates the measured relative oil permeabilities with a high average relative error and an associated large variance. Just as the Berea sandstone, the maximum relative errors appear at low values of measured oil relative permeability.

5.1.3 Three-phase gas relative permeability

Using the mechanistic model, the predicted gas relative permeabilities underestimated the measured data of the Berea sandstone and Bentheimer sandstone by about 10 and 30%, respectively; but the average relative error of about 1.69±6.71 quantified for the experimental data of Berea sandstone does not provide the same conclusion. Apparently, the mechanistic model overestimates the low relative permeabilities measured in the experiment, even by factor of 10 and more. In the case of Bentheimer sandstone, the measured gas relative permeabilities are well represented by the model predictions. The maximum relative errors do not exceed 1.5 for the extremely low gas relative permeabilities measured in the experiment.

The TD compatible model provided only reliable predictions for the Bentheimer sandstone. The difficulties described in section 4.2, the very high capillarity of Berea sandstone, poses problems in the interpolation of the global capillary pressure and its derivatives with respect to water saturation (s_1) and gas saturation (s_3).

Using the Parker-Lenhard model, the gas relative permeabilities predicted for Berea sandstone and Bentheimer sandstone strongly overestimate the measured gas relative permeabilities. The maximum relative errors are observed for very low relative permeabilities (<0.01). In the case of Berea sandstone, the maximum relative errors attain values of 1000 (option kr-S) and 100 (option Pc-S) whereas for Bentheimer sandstone values of about 26 (option kr-S) and 14 (option Pc-S) are achieved. Even for higher relative permeabilities measured for both sandstones, the predicted gas relative permeabilities overestimate the experimental data globally by at least a factor of 2.

5.2 Existence of elliptic zones in the ternary diagram

The existence and importance of elliptic zones in a water-oil (NAPL)-gas ternary diagram when using the mechanistic model will be discussed. In Appendices G.4 and G.5, the results obtained with the Parker-Lenhard model and Stone's model I are presented. The percentage of saturation space covered by elliptic regions quantified for the three models are summarized in Table 12. It should be noted that the three fluid saturations

in the ternary diagram range from 0 to 1; few authors used effective saturations in their studies (e.g. Jackson and Blunt, 2002).

The starting point is the mass conservation equation for an incompressible, immiscible three-phase flow which can be written in terms of two saturation equations for water (α =1) and gas phases (α =3) (Eq. (G2), Appendix G). In the case of zero capillary pressure, the dimensionless system of saturation equations can be linearized in terms of two saturation gradients involving a Jacobian matrix J as follows:

$$\partial_{t_D} S_{1,3} + J \nabla_{z_D} S_{1,3} = 0 \text{ with } J = \begin{pmatrix} \frac{\partial f_1}{\partial s_1} & \frac{\partial f_1}{\partial s_3} \\ \frac{\partial f_3}{\partial s_1} & \frac{\partial f_3}{\partial s_3} \end{pmatrix}, \quad (19)$$

where z_D and t_D are the dimensionless distance and time (Appendix G), f_1 and f_3 are fractional flow functions of water and gaz, respectively, defined as:

$$f_1 = \frac{\lambda_1}{\lambda_t}(1 - \mathcal{N}_G((\rho_D - 1)k_{r2} + \rho_D \frac{\mu_2}{\mu_3} k_{r3})), \quad (20)$$

$$f_3 = \frac{\lambda_3}{\lambda_t}(1 + \mathcal{N}_G(\rho_D \frac{\mu_2}{\mu_1} k_{r1} + k_{r2})), \quad (21)$$

with the gravity number $\mathcal{N}_G = \frac{K(\rho_2 - \rho_3)g}{\mu_2 v_{tot}}$, $\rho_D = \frac{\rho_1 - \rho_3}{\rho_2 - \rho_3}$ is the density ratio, λ_α is the phase mobility and λ_t is the total mobility defined as $\lambda_t = \sum_\alpha k_{r\alpha} / \mu_\alpha$.

Eigenvalues $u_D^{\pm}$ of the Jacobian matrix J can then be expressed as follows:

$$u_D^{\pm} = \frac{1}{2}\left[\frac{\partial f_1}{\partial s_1} + \frac{\partial f_3}{\partial s_3} \pm \sqrt{\left(\frac{\partial f_1}{\partial s_1} - \frac{\partial f_3}{\partial s_3}\right)^2 + 4\frac{\partial f_1}{\partial s_3}\frac{\partial f_3}{\partial s_1}}\right] \quad (22)$$

The corresponding partial derivatives of fractional flow functions f_1 and f_3 are detailed in Appendix G. To compute elliptic regions that provide numerical instabilities, we analyzed the sign of the square root argument of Eq. (22). Within the ternary diagram, a large set of fluid saturations was studied in order to display complex eigenvalues that correspond to a negative square root argument. To validate our search algorithm of negative square root arguments of Eq. (22), we first used the model of Bell and compared the identified elliptic zones with those quantified by Jahanbakhshi et al. (2013) (Appendix G.3). Furthermore, the influence of gravity and total velocities on the extent of elliptic zones are synthetically discussed in Appendix G.

5.2.1 Bentheimer sandstone

The fluid properties of experiments conducted on Bentheimer sandstone (Table 2), the intrinsic permeability of the rock $K = 2.63 \times 10^{-12}$ m^2, and the quantified characteristic coefficients A_{ij} (summarized in Table 7) of the three modeling options (A, C, and AC) were used to study the possible existence of elliptic zones in the ternary diagram. In a first modeling step, gravity effects were neglected. The results obtained for options A, C and AC are shown on the left side of Fig. 34. In all three modeling options, there is a very small elliptic zone on the water-oil side with a percentage area of less than 1%. The double dependency on water and gas saturation, as in Stone's model, has often been pointed as proof for the existence of an elliptic zone modulo with certain constraints on viscosities (Trangenstein, 1989; Jackson and Blunt, 2002). Here, the elliptic region, however, is a narrow zone located near the water-oil edge with gas saturations below 5%, while the oil saturations range between 50% and 80%.

To study the influence of gravity on the extent and distribution of elliptic zones in the ternary diagram, we used a series of total velocities, which are in the range of total velocities applied in Alizadeh's DDI experiments. In all modeling options, when the total velocity is equal to 1.5×10^{-4} ms^{-1}, the area of the elliptic zone represents less than 1% of the total area of the ternary diagram. However, the further decrease of the total velocity significantly alters the area and form of the elliptic zone. For example, in modeling option C the elliptic zones are significantly larger with almost 30% of the total surface for a velocity that is ten times lower. Note that all three models are characterized by the occurrence of elliptic regions, where the directions associated with the eigenvectors coincide. For a velocity that is one hundred times lower, the elliptic zone will again

become smaller and occupy only 10% of the total area of the ternary diagram (Table 12). Modeling option C seems to generate larger elliptic zones located near the water-gas side than options A and AC, particularly when water saturation is greater than 50%.

In modeling option A, the elliptic zone appearing for a total velocity of 1.5×10^{-5} ms^{-1} is nearly the same as in modeling option AC; it represents about 20% of the total surface of the ternary diagram. Just as option C, with decreasing total velocity the elliptic zones are smaller; for a velocity that is ten times lower, the occupied surface attains about 15% of the total surface. It should be noted that the use of the mechanistic model leads to a plurality of elliptical zones, which was not the case when using Bell's model (Fig. G2, Appendix G) or was not observed in the Jackson and Blunt (2002) experiments on a pore-scale model manufactured with a bundle of cylindrical capillary tube. The number of elliptic zones, between two and three, is a function of the total velocities and is located in very different sectors of the ternary diagram. Note that in the case of very low total velocities (corresponding to high gravity numbers of 5) a large fraction is found in the region of irreducible water saturation.

<table>
<tr><td>without gravity</td><td colspan="3">with gravity at different total velocities</td></tr>
<tr><td>Option A</td><td colspan="3">Option A</td></tr>
<tr><td> 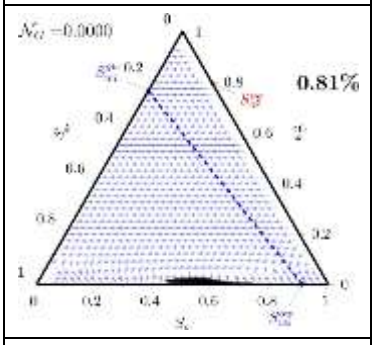
</td><td> 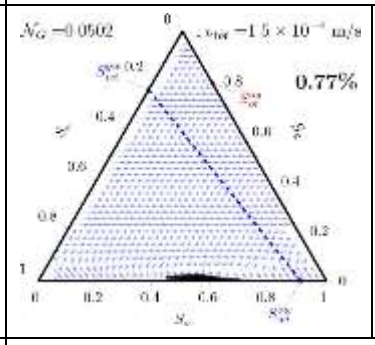
</td><td> 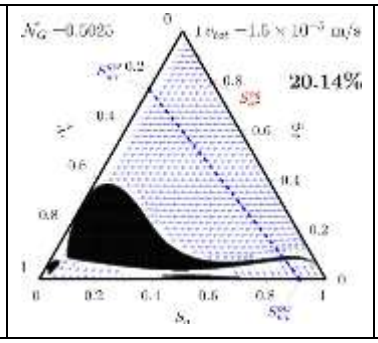
</td><td> 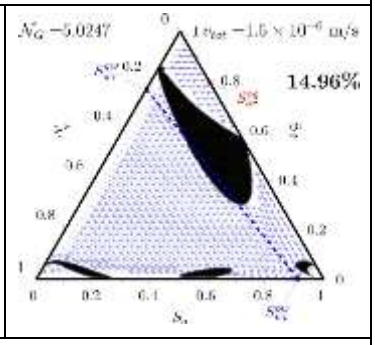
</td></tr>
<tr><td>Option C</td><td colspan="3">Option C</td></tr>
<tr><td> 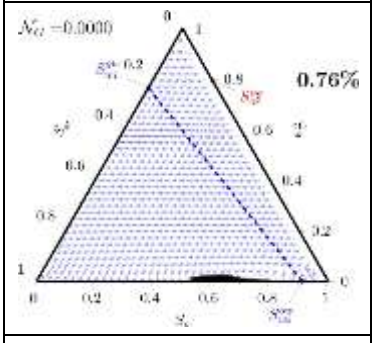
</td><td> 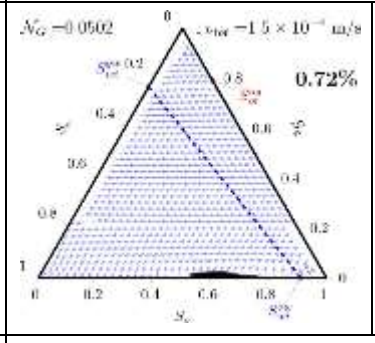
</td><td> 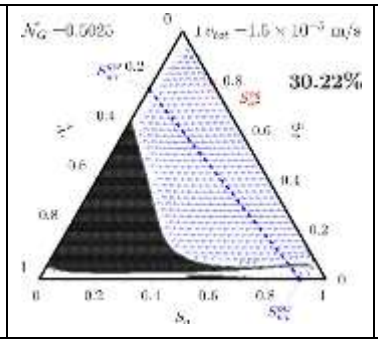
</td><td> 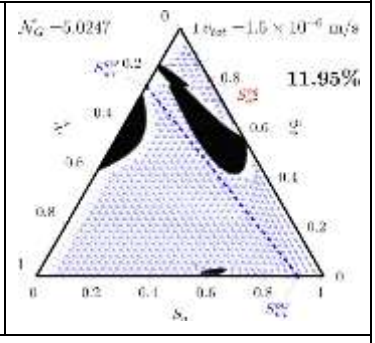
</td></tr>
<tr><td>Option AC</td><td colspan="3">Option AC</td></tr>
<tr><td> 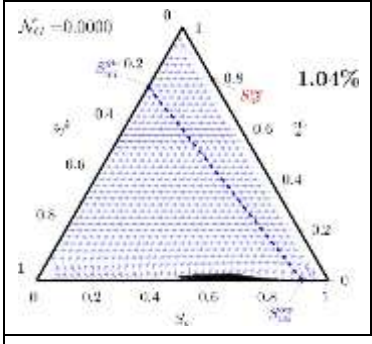
</td><td> 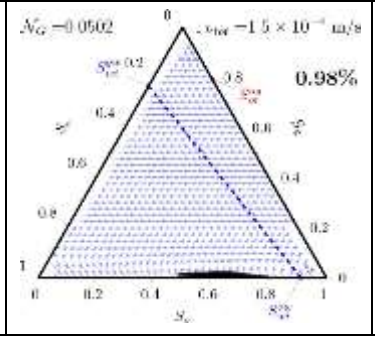
</td><td> 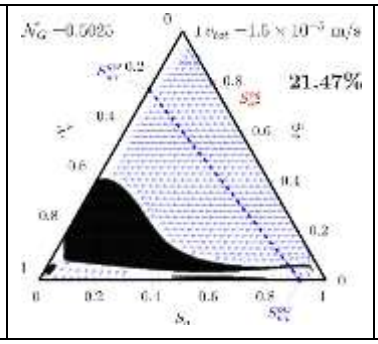
</td><td> 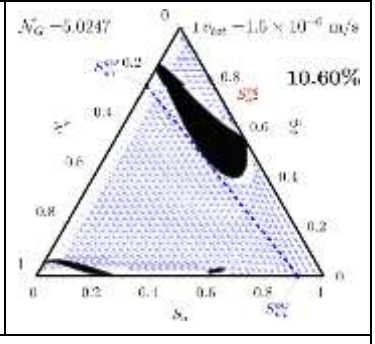
</td></tr>
</table>

Fig. 34. Bentheimer sandstone: influence of gravity and total velocity on the extent of elliptic regions in the ternary diagram. $\mathcal{N}_G$ is the dimensionless gravity number. The results show the percentage of saturation space covered by elliptic regions and the distribution of eigenvectors associated with fast rarefaction waves (blue arrows). Elliptic regions are depicted as the black areas. The dotted blue lines indicate the limits of irreducible water saturation.

Table 12: Percentage area of elliptical zones in the ternary diagram quantified for the mechanistic model, Parker-Lenhard model, and Stone's model I: (a) Bentheimer sandstone, (b) Berea sandstone.

(a) Bentheimer sandstone

Model	Option	Without gravity	With gravity, at different total velocities v_{tot}		
			1.5×10^{-4} ms^{-1}	1.5×10^{-5} ms^{-1}	1.5×10^{-6} ms^{-1}
Mechanistic model	A	0.81	0.77	20.14	14.96
	C	0.76	0.72	30.22	11.95
	AC	1.04	0.98	21.47	10.60
Parker-Lenhard Model	Pc-S	1.37	1.54	22.73	8.46
	kr-S	1.58	1.88	24.35	8.89
Stone's model I		1.38	22.63	10.76	31.50

(b) Berea sandstone

Model	Option	Without gravity	With gravity, at different total velocities v_{tot}		
			1.5×10^{-5} ms^{-1}	1.5×10^{-6} ms^{-1}	1.5×10^{-7} ms^{-1}
Mechanistic model		0.05	16.28	20.10	10.89
Parker-Lenhard Model	Pc-S	0.00	0.81	0.41	0.00
	kr-S	2.68	10.90	15.19	10.89
Stone's model I		0	1.22	43.44	31.50

5.2.2 Berea sandstone

A second study on the existence of elliptic zones was conducted with the mechanistic model using the experimental data of the Berea sandstone (Table 3) and the intrinsic permeability of the rock $K = 1.97 \times 10^{-13}$ m^2. The quantified characteristic coefficients A_{ij} summarized in Table 5 were used to study the possible existence of elliptic zones in the ternary diagram.

The results of the study are presented in Fig. 35 with the reference case without gravity. In the absence of gravity, elliptic zones are almost nonexistent compared to the zones identified for the Bentheimer sandstone (Fig. 34). Significant elliptic regions appear only for total velocities lower than 2×10^{-5} ms^{-1}. By decreasing the total velocity, the percentage area of saturation space covered by elliptic regions progressively increases up to about 42% at a total velocity of 5×10^{-6} ms^{-1}. A further decrease in total velocities will lead to a continuous reduction in the percentage area occupied by the elliptic regions which becomes stable around 10% for total velocities between 1.5×10^{-7} and 1.5×10^{-8} ms^{-1} (Fig. 34). Table 12 summarizes the percentage area covered by elliptic regions for total velocities of 1.5×10^{-5}, 1.5×10^{-6} and 1.5×10^{-7} ms^{-1}, which are in the range of total velocities applied in Oak's DDI experiments. It is worth noting that for gravity numbers lower than 0.5, the elliptic region is located at the water summit and forms a single patch. Increasing the gravity number will lead to an increase in the elliptic region accompanied by a separation of the single patch in two or more sub-areas. Up to a gravity number of about 1.11 (corresponding to a total velocity of about 9×10^{-6} ms^{-1}), the saturation space covered by elliptic zones is mainly located in the ternary diagram where water is mobile. The main part of the elliptic region is situated above the gravity number 3.3 in an irreducible water zone.

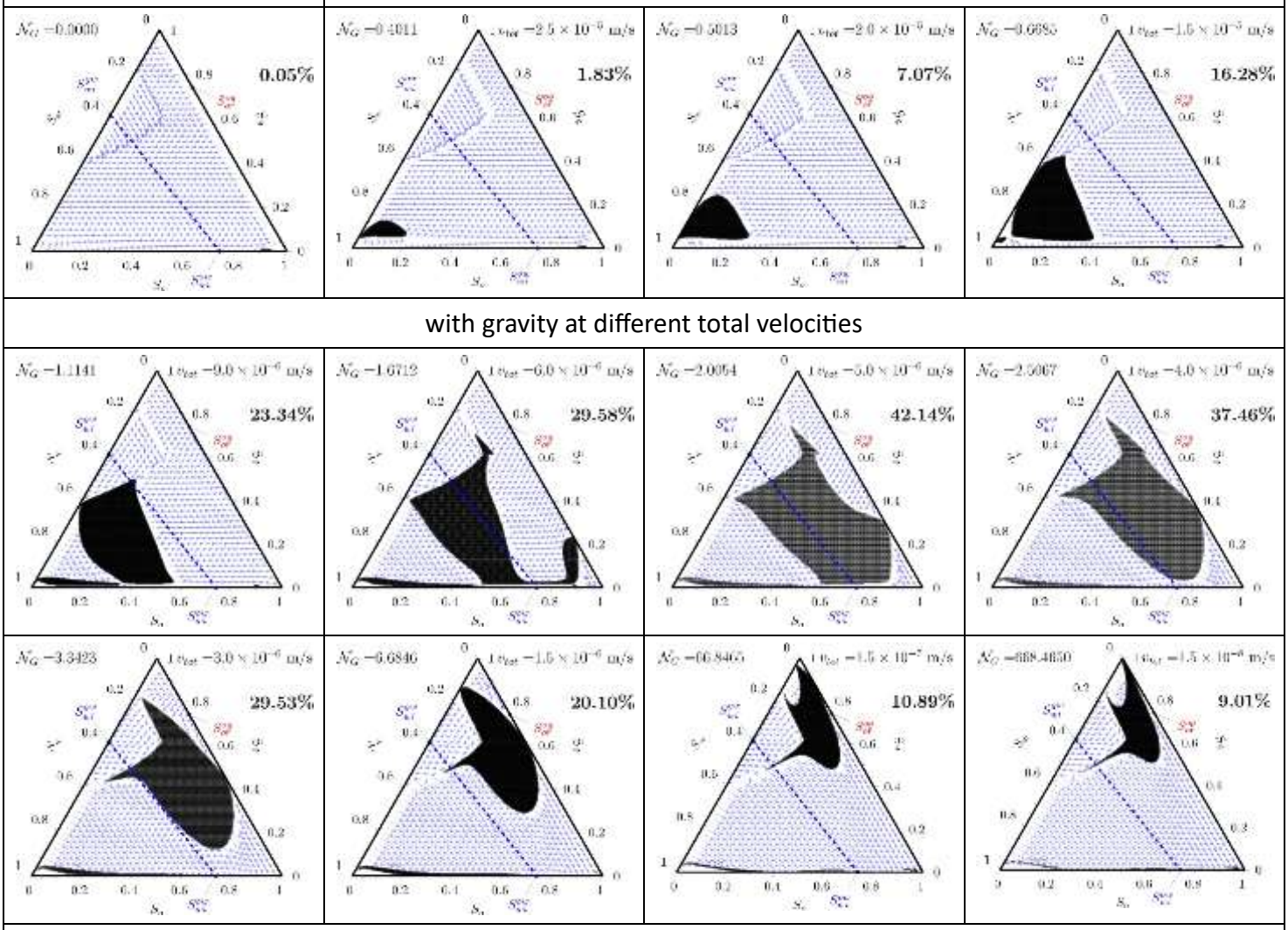

Fig. 35. Berea sandstone: influence of gravity and total velocity on the extent of elliptic regions in the ternary diagram. $\mathcal{N}_G$ is the dimensionless gravity number. The results show the percentage of saturation space covered by elliptic regions and the distribution of eigenvectors associated with fast rarefaction waves (blue arrows). Elliptic regions are depicted as the black areas. The dotted blue lines indicate the limits of irreducible water saturation.

6. Conclusions and future work

In this study, two recent and two classical models were evaluated against experimentally measured three-phase permeabilities. Experimental data generated on two different water-wet sandstones were selected from the literature to evaluate and compare the four mathematical models. Experimentally determined constitutive relationships in two-phase systems were used as input parameters to numerically predict relative permeabilities (k_r) in three-phase systems, and then the estimated results were compared with experimental three-phase permeabilities measured along decreasing water saturation/decreasing oil saturation/increasing gas saturation (DDI) paths.

Which models yield results that best match flow experiments?

Globally, the best prediction of the measured k_r values was obtained with the mechanistic model of Shahverdi and Sohrabi (2017). However, its implementation requires a preliminary calibration of the relative phase permeabilities in a three-phase system against experimental data along one DDI path to quantify the required six characteristic coefficients.

Our study showed that the Parker-Lenhard model provides very different predicted k_r values that are strongly dependent on the method used to determine the Van Genuchten parameter (m). Globally, the oil relative permeabilities predicted for the Berea sandstone using the Parker-Lenhard model shows the same general trend as observed for the water relative permeabilities: modeling option kr-S overestimates and modeling option Pc-S underestimates the measured relative oil permeabilities. Furthermore, using the Parker-Lenhard model, the gas relative permeabilities predicted for Berea sandstone and Bentheimer sandstone are significantly higher than the measured gas relative permeabilities.

In the case of Berea sandstone, the oil relative permeability is reasonably well predicted by Stone's model I. Nevertheless, the oil relative permeability expected for Bentheimer sandstone indicates a different behavior than Berea sandstone. In this case, the simulation based on Stone's model I significantly overestimates the measured relative oil permeabilities with a high average relative error and an associated large variance. Just as the Berea sandstone, the maximum relative errors appear at low values of measured oil relative permeability.

For the first time, the TD compatible model has been applied to detailed experimental three-phase data. Our study showed that the global mobilities predicted by C0 finite element interpolation significantly overestimate the experimentally quantified global mobilities. Prediction improved when experimental data were used to locally impose the global mobility. Our numerical study also revealed weaknesses in the TD compatible model. The main issue is the fulfillment of the required condition of fractional flows of water, oil and gas predicted by the PDE-TD interpolation algorithm, which should be bounded by the physical limits of 0 and 1 everywhere in the ternary diagram. This condition was respected in the case of negligible residual wetting phase saturation, low capillary porous medium and smooth variations of associated capillary pressure gradients, as shown in the study of di Chiara et al. (2010). In our case, however, it appears that the very high capillarity of both the Bentheimer and Berea sandstones contributes to numerically interpolated water and gas fractional flows in the ternary diagram that locally fall below the physical lower limit of 0 and exceed its upper limit of 1. This in turn leads to negative oil fractional flow and thus results in unphysical oil relative permeabilities.

What input data do the models require, and how burdensome are these requirements?

The least request of input data is required when using the Parker-Lenhard model and Stone's model I. The Parker-Lenhard model requires only Van Genuchten parameter m and the irreducible wetting fluid saturation to model the three-phase relative permeabilities of water, oil and gas. To quantify the oil relative permeability in a three-phase fluid system, Stone's model I uses as input data, the oil relative permeabilities in the two-phase gas-oil and oil-water systems, the irreducible water saturation, and residual oil saturation.

The use of the mechanistic model to predict three-phase relative permeabilities requires not only three two-phase relative permeabilities but also six coefficients that presumably take into account the interaction between various fluids, as well as fluid saturation distributions. It should be noted that at least one set of experimental three-phase relative permeability data (for one saturation path) for all three fluids is required to tune these characteristic coefficients. To reduce the degree of uncertainty, Shahverdi and Sohrabi (2017) suggested employing more measured data of three-phase relative permeabilities for calibration of the six characteristic coefficients. In the case of Bentheimer sandstone, using two experimental data sets instead of one for tuning the characteristic coefficients, only slightly improved the predicted k_r values. The use of different input data sets also revealed the absence of a unique solution for the calibration of these six characteristic coefficients. This resulted in different qualities in the subsequent prediction of the relative permeabilities.

To predict three-phase relative permeabilities using the TD compatible model, the user requires more input data than the other three models. It requires detailed information of the dynamic viscosities of the three fluid phases, the variation of gas density as a function of the gas pressure, as well as the two-phase relative permeabilities and capillary pressures known on the edges of the ternary diagram. Since capillary pressure

curves are not always available for all two-phase fluid pairs involved in flow experiments, at least the water retention curve measured in the water-gas system is required. The scaling approach (Parker et al, 1987) based on the interfacial tensions of the two-phase gas/water, gas/oil and oil/water systems may be used to parameterize the required capillary pressure curves in a water-oil and oil-gas system.

What are the models' computational requirements, both in deriving three-phase relative permeability functions and in using them in a flow simulator?

The most computational effort to assess three-phase relative permeabilities is required for the TD compatible model. The predicted three-phase relative permeabilities and global capillary pressures satisfy a so-called Total Differential (TD) compatibility-condition which guarantees strict hyperbolicity of the reformulated system (Chavent and Jaffré, 1986). Boundary conditions for global capillary pressure and global mobility are required such that the corresponding three-phase data are consistent with a given set of three two-phase data. The numerical construction of global capillary pressure and global mobility functions by C1 and C0 finite element is performed using bi-Laplacian and Laplacian interpolation. The TD-compatibility condition required for the two-phase data sets prescribed on the three edges of the ternary diagram is a nonlinear constraint on weighted means of the given two-phase relative permeability data set. This presents a certain weakness of this model in contrast to its strength of being free of elliptic zones in the saturation space. It should be emphasized that the three-phase data obtained with the TD compatible model allow the three-phase compressible global volumetric flow equation to be rewritten in a more suitable fractional form: the gradient-of-capillary-pressure coupling terms are eliminated from the formula for the global volumetric flow (Chavent, 2009). This may lead to a more efficient computing time compared to traditional pressure-saturation models.

The mechanistic model uses an arithmetic averaging relationship between two-phase and three-phase permeabilities. Here, the user must first tune the six characteristic coefficients using for example a commercial tool. Once quantified, the estimated characteristic coefficients can then be easily implemented in any flow simulator to model three-phase relative permeabilities for any other saturation path.

The least numerical effort to build up three-phase relative permeabilities is required for the Parker-Lenhard model and Stone's model I. In both cases, the mathematical functions using the two-phase relative permeabilities of water and gas as input data can be directly implemented in flow simulators, which is already the case for commercial flow simulators (e.g. MOFAT (US EPA,1991), Eclipse (Schlumberger, 2015)) for simulation of three-phase flow. It is noteworthy here that numerical issues may occur with Stone's model I when normalized water and gas saturations achieve high values close to the physical upper limit of 1.

Which models admit elliptic regions in saturation space?

To assess the presence of potential elliptic zones, in our study we tested the mechanistic model, the Parker-Lenhard model and Stone's model I in the case of Bentheimer and Berea sandstones. All three models admit elliptic zones. Gravitational effect causes multiple elliptic zones that depend on the total flux applied to the rock samples. The percentage area of elliptical zones in the ternary diagram quantified for Stone's model I was the highest and supports the results previously reported in the literature. Our numerical results showed that the Parker-Lenhard model produces a higher percentage area of elliptic zones than the mechanistic model. Note that in our study we neglected the capillarity of the porous media, which may dim the extent of potential elliptic zones. As complete datasets on capillary pressure-saturation curves are available for both sandstones, it could be interesting to implement the effect of capillarity in the evaluation of elliptic zones under the given experimental conditions.

In the case of the TD compatible model, our study revealed that the interpolation of the global capillary pressure and its derivatives exposes unphysical fractional phase flows; the Total Differential compatible

approach will not be verified everywhere within the ternary diagram. This could also be an indication of existing elliptic regions.

To build up a more robust TD compatible modeling approach and to obtain reliable physical values of predicted fractional flows in the 3-phase ternary diagram, further research steps are needed:

(i) To overcome the problem of overestimated global mobilities, a more promising solution could be used to solve the Poisson's equation instead of the Laplace equation. Since the Poisson's equation is the inhomogeneous equivalent form of Laplace's equation, the associated spatially variable source function could be quantified by an inverse modeling approach using a limited number of pilot points (on experiment based global mobilities), uniformly distributed in the ternary diagram. A non-linear least square method may be used to minimize the objective function of the inverse problem.

(ii) A similar inverse modeling approach could be used to improve the interpolation of the global capillary pressure (P_c^g) and its spatial derivatives on the ternary diagram. Step 5 of the PDE-TD-interpolation algorithm (Table 1) could be replaced by solving the inhomogeneous biharmonic equation. Here, the pilot points could include the experiment based fractional water and gas flows, and therefore reprocessed into spatial derivatives of P_c^g with respect to s_1 and s_3 using Equation 17.

In our study, measurements of three-phase relative permeabilities along DDI paths were compared with those predicted from four mathematical models. An open question is still the goodness of predicted relative permeabilities when increasing both the water and oil flux and decreasing the gas flux. This may also be part of further research work.

In addition, while not yet considered in this work, it would be interesting to assess the relative skills of the models tested, as described by e.g. Ranaee et al. (2016) using model identification criteria. This could be a way to take into account the complexity of a given model, at least in terms of the number of parameters involved and possibly also considering the level of uncertainty associated with parameter estimates (through the estimation of the covariance matrix). As an additional benefit, the use of these criteria yield the probability (posterior probability, conditional on the number of available data) associated with a given model, eventually leading to a multi-model framework. Further studies could also focus on the parameter identification as shown in the work of Ranaee et al. (2017).

Acknowledgment

This research was granted from January to August, 2019 by the French-American Fulbright commission and the Institute of International Education/Council for International Exchange of Scholars (IIE/CIES), US Department of State. Gerhard Schäfer is also grateful for the financial support by the University of Strasbourg during his sabbatical leave at the Center of Innovation for Flow through Porous Media, University of Wyoming and the administrative and technical support by the University of Wyoming.

Data availability statement

The data that support the findings of this study are available from the corresponding author upon reasonable request.

References

Alizadeh, A. H., 2013. Experimental Study of Three-Phase Flow in Porous Media, PhD dissertation, University of Wyoming, Laramie, Wyoming.

Alizadeh, A. H., Piri, M., 2014a. Three-phase flow in porous media: A review of experimental studies on relative permeability, Rev. Geophys. 52, doi:10.1002/2013RG000433.

Alizadeh, A. H., Piri, M., 2014b. The effect of saturation history on three-phase relative permeability: An experimental study, Water Resour. Res. 50, 1636–1664, doi:10.1002/ 2013WR014914.

Amaziane, B., Jurak, M., Vrbaski, A., 2012. Existence for a global pressure formulation of water-gas flow in porous media. Electronic Journal of Differential Equations, Texas State University, Department of Mathematics, 102, 1-22.

Baker, L.E., 1988. Three-phase Relative Permeability Correlations, Society of Petroleum Engineers. doi:10.2118/17369-MS

Bell, J. B., Trangenstein, J. A., Shubin, G. R., 1986. Conservation laws of mixed type describing three-phase flow in porous media, SIAM J. Appl. Math. 46, 1000-1017.

Blunt, M., Zhou, D., Fenwick, D., 1995. Three-phase flow and gravity drainage in porous media, Transport in Porous Media 20, 77–103.

Blunt, M.J., 2000. An Empirical Model for Three-phase Relative Permeability, Society of Petroleum Engineers. doi:10.2118/67950-PA.

Bohy, M., Dridi, L., Schäfer, G., Razakarisoa, O., 2006. Transport of a mixture of chlorinated solvent vapors in the vadose zone of a sandy aquifer, Vadose Zone Journal 5, 539-553.

Brusseau, M.L., 1992. Rate limited mass transfer and transport of organic solutes in porous media that contain immobile immiscible organic liquid, Water Resour. Res. 28, 33–45.

Benisch, K., Wang, W., Delfs, J.-O. D., Bauer, S., 2020. The OGS-Eclipse code for simulation of coupled multiphase flow and geomechanical processes in the subsurface, Computational Geosciences 24, 1315–1331. https://doi.org/10.1007/s10596-020-09951-8.

Celia, M.A., Bachu, S., Nordbotten, J.M., Bandilla, K.W., 2015. Status of CO2 Storage in Deep Saline Aquifers with Emphasis on Modeling Approaches and Practical Simulations", Special 50th Anniversary Issue of Water Resources Research, DOI 10.1002/2015WR017609.

Chatzis, I., Morrow, N. R., 1984. Correlation of capillary number relationships for sandstone, SPE Journal 24, 555–562, doi:10.2118/10114-PA.

Chavent, G., Jaffré, J., 1986. Mathematical Models and Finite Elements of Reservoir Simulation, North-Holland, Amsterdam. Elsevier Science publishers B.V.

Chavent, G., di Chiara Roupert, R., Schäfer, G., 2008. A fully equivalent global pressure formulation for three-phase compressible flows, in: Conference Scaling'Up 08, Dubrovnik, October 13–16, 2008.

Chavent, G., 2009. A fully equivalent global pressure formulation for three-phase compressible flow, Appl. Anal. 88, 1527–1541.

Cohen, R.M., Mercer, J.W., 1993. DNAPL site evaluation. C.K. Smoley (ed.) CRC Press, Boca Raton, FL.

Côme, J.M., Quintard, M., Schäfer, G., Mosé, R., Delaplace, P., Haeseler, F., 2008. Modélisation du devenir des composés organo-chlorés aliphatiques dans les aquifères – Guide méthodologique ADEME - Collection ADEME «Connaître pour Agir» - Programme R&D MACAOH (Modélisation, Atténuation, Caractérisation dans les Aquifères des Organo-Halogénés), 191 p.

Corey, A. T., Rathjens, C. H., Henderson, J. H., Wyllie, M. R. J., 1956. Three-Phase Relative Permeability. Society of Petroleum Engineers. doi:10.2118/737-G.

Cotel, S., Schäfer, G., Barthes, V., Baussand, P., 2011. Effect of density-driven advection on trichloroethylene vapor diffusion in a porous medium, Vadose Zone J. 10, 565-581, doi:10.2136/vzj2010.0032.

Delshad, M., Pope, G.A., 1989. Comparison of the three-phase oil relative permeability models, Transport in Porous Media 4, 59–83.

di Chiara Roupert, R., 2009. Développement d'un code de calcul multiphasique multiconstituants, PhD thesis, Université de Strasbourg.

di Chiara Roupert, R., Chavent, G., Schäfer, G., 2010a. Threephase compressible flow in porous media : total differential compatible interpolation of relative permeabilities, J. Comput. Phys. 229, 4762-4780.

di Chiara Roupert, R., Schäfer, G., Ackerer, P., Quintard, M., Chavent, G., 2010b. Construction of three-phase data to model multiphase flow in porous media: comparing an optimisation approach to the finite element approach, CR Geoscience 342, 855-863.

Dridi, L., Pollet, I., Razakarisoa, O., Schäfer, G., 2009. Characterisation of a DNAPL source zone in a porous aquifer using the Partitioning Interwell Tracer Test and an inverse modelling approach, Journal of Contaminant Hydrology 107, 22–44.

Eberhardt, C., Grathwohl, P., 2002. Time scales of organic contaminant dissolution from complex source zone: coal tar pools vs. blobs, J. Contam. Hydrol. 59, 45–66.

Fried, J.J., Muntzer, P., Zilliox, L., 1979. Groundwater pollution by transfer of oil hydrocarbons, Ground Water 17, 586–594.

Helland, J. O., Jettestuen, E., 2016. Mechanisms for trapping and mobilization of residual fluids during capillary-dominated three-phase flow in porous rock, Water Resour. Res., 52(7), 5376–5392, doi:10.1002/2016WR018912.

Helmig, R. Flemisch, B., Wolff, M., Ebigbo, A., Class, H., 2013. Model coupling for multiphase flow in porous media, Advances in Water Resources 51, 52-66.

Isaacson, E. L., Marchesin, D., Plohr, B. J., 1990. Transitional waves for conservation laws. SIAM journal on mathematical analysis 21(4), 837–866.

Jackson, M. D., Blunt, M. J., 2002. Elliptic regions and stable solutions for three-phase flow in porous media, Transport in porous media 48(3), 249–269.

Kennedy, C.A., Lennox, W.C., 1997. A pore-scale investigation of mass transport from dissolving DNAPL droplets, J. Contam. Hydrol. 24, 221–246.

Jahanbakhshi, S., Ghazanfari, M. H., Masih, M., 2013. Non-equilibrium model of three-phase flow in porous media in presence of capillary and gravity forces, Journal of Hydrology 478, 119-131.

Jellali, S., Muntzer, P., Razakarisoa, O., Schäfer, G., 2001. Large scale experiment on transport of trichlorethylene in a controlled aquifer, Transport in Porous Media 44(1), 145-163.

Jellali, S., Benremita, H., Muntzer, P., Razakarisoa, O., Schäfer, G., 2003. A large-scale experiment on mass transfer of trichlorethylene from the unsaturated zone of a sandy aquifer to its interfaces, Journal of Contaminant Hydrology 60 (1-2), 31-53

Leverett, M.C., Lewis, W.B., 1941. Steady Flow of Gas-oil-water Mixtures through Unconsolidated Sands, Society of Petroleum Engineers. doi:10.2118/941107-G.

Mendoza, C.A., Frind, E.O., 1990. Advective–dispersive transport of dense organic vapors in the unsaturated zone, 1. Model development, Water Resour. Res. 26, 379–387.

Mualem, Y., 1976. A new model for predicting the hydraulic conductivity of unsaturated porous media, Water Resources Research 12(3), 513–521.

Oak, M. J., 1990. Three·Phase Relative Permeability of Water-Wet Berea, paper SPE/DOE 20183 presented at the 1990 SPE/DOE Symposium on Enhanced Oil Recovery, Tulsa, April 22-25.

Oak, M. J., Baker, L. E., Thomas, D. C., 1990. Three-phase relative permeability of Berea sandstone, Journal of Petroleum Technology 42(8), 1054–1061.

Øren, P. E., Pinczewski, W. V., 1995. Fluid distribution and pore-scale displacement mechanisms in drainage dominated three-phase flow, Transp. Porous Med., 20, 105–133, doi:10.1007/BF00616927.

Pankow, J. F., Cherry, J.A., 1996. Dense Chlorinated Solvent and Other DNAPLs in Ground Water: History, Behavior and Remediation. Waterloo Press, Ontario, Canada, p. 260.

Parker, J. C., Lenhard, R. J., Kuppusamy, T., 1987. A Parametric Model for Constitutive Properties Governing Multiphase Flow in Porous Media. Water Resour. Res. 23(4), 618–624.

Parker, J.C., Lenhard, R. J., 1990. Determining three-phase permeability-saturation-pressure relations from two-phase system measurements, Journal of Petroleum Science and Engineering 4, 57-65.

Portois, C., Essouayed, E., Annable, M. D., Guiserix, N., Joubert, A., Atteia, O., 2018. Field demonstration of foam injection to confine a chlorinated solvent source zone, Journal of Contaminant Hydrology 214, 16–23, doi.org/10.1016/j.jconhyd.2018.04.003.

Qian, L., Chen, Y., Ouyang, D., Zhang, W., Han, L., Yan, J., Kvapil, P., Chen, M., 2020. Field demonstration of enhanced removal of chlorinated solvents in groundwater using biochar-supported nanoscale zero-valent iron, Science of the Total Environment 698, doi.org/10.1016/j.scitotenv.2019.134215.

Ranaee, E., Porta, G. M., Riva, M., Blunt, M. J., Guadagnini, A., 2015. Prediction of three-phase oil relative permeability through a sigmoid based model, J. Petrol. Sci. Eng. 126, 190–200, doi:10.1016/j.petrol.2014.11.034.

Ranaee, E., Riva, M., Porta, G. M., Guadagnini, A., 2016. Comparative assessment of three-phase oil relative permeability models, Water Resour. Res. 52, 5341-5356, doi:10.1002/2016WR018872.

Ranaee, E., Moghadasi, L., Inzoli, F., Riva, M., Guadagnini, A., 2017. Identifiability of parameters of three-phase oil relative permeability models under simultaneous water and gas (SWAG) injection, J. Petrol. Sci. Eng. 159, 1-10, doi:10.1016/j.petrol.2017.09.062.

Schlumberger, L., 2015. Eclipse 100 technical description and user manual. Technical Report.

Schneider, L., 2015. Développement d'un modèle numérique pour l'écoulement triphasique de fluides incompressibles, PhD thesis, Université de Strasbourg.

Schwille, F., 1988. Dense chlorinated solvents in porous and fractured media. Models experiments. Lewis Publishers, Boca Raton, FL, p.146. Pankow, J.J., translator.

Seyedabbasi, M. A., Newell, C. J., Adamson, D. T., Sale, T. C., 2012. Relative contribution of DNAPL dissolution and matrix diffusion to the long-term persistence of chlorinated solvent source zones, Journal of Contaminant Hydrology 134–135, 69–81, doi:10.1016/j.jconhyd.2012.03.010.

Shahverdi, H., Sohrabi, M., Jamiolahmady, M., 2011. A new algorithm for estimating three-phase relative permeability from unsteady-state core experiments, Transp. Porous Media 90 (3), 911–926. DOI 10.1007/s11242-011-9823-9.

Shahverdi, H., Sohrabi, M., 2017. A mechanistic model for prediction of three-phase flow in petroleum reservoirs, Journal of Petroleum Science and Engineering 157, 507–518.

Sleep, B.E., Sykes, J.F., 1992. The influence of infiltrating wetting fronts on transport of volatile organic compounds in variably saturated porous media. In: Weyer, K.U. (Ed.), Proceedings of the International Conference on Subsurface Contamination by Immiscible Fluids (International Association of Hydrology), Calgary, Alberta, Canada, April 18–20, 1990. A. A. Balkema, Rotterdam.

Stone, H.L., 1970. Probability model for estimating three-phase relative permeabilitiy, Journal of Petroleum Technology 22, 214–218.

Stone, H.L., 1973. Estimation of Three-Phase Relative Permeability and Residual Oil Data. J. Cdn. Pet. Tech. 12 .

US EPA, 1991. MOFAT: A Two-Dimensional Finite Element Program for Multi-Phase Flow and Multi-Component Transport, Program Documentation and User's Guide.Publication No. EPA/600/2-91/020.

Trangenstein, J. A., 1989. Three-phase flow with gravity, Contemp. Math 100, 147–159.

Van Dijke, M. I. J., Sorbie, K. S., 2002. The relation between interfacial tensions and wettability in three-phase systems: consequences for pore occupancy and relative permeability, J. Pet. Sci. Eng., 33, 39–48.

Van Genuchten, M.T., 1980. A closed-form equation for predicting the hydraulic conductivity of unsaturated soils, Soil Sci. Soc. Am. J. 44, 892–898.

APPENDICES

Appendix A. Two-phase constitutive relationships used in the study

A.1 Capillary pressure curves in two-phase systems: water-oil and oil-gas

The Van Genuchten (1980) model uses a simple analytical expression to describe the capillary pressure curves. In a two-phase water-gas system, the capillary pressure p_{cgw} (Pa) as function of the effective saturation of the wetting fluid phase (water) is described by

$$p_{cgw} = \frac{1}{\alpha}\left[S_{we}^{-\frac{1}{m}} - 1\right]^{1-m}, \text{ with } m = 1 - \frac{1}{n} \qquad \text{(A1)}$$

where α (Pa^{-1}) and n (-) are empirical parameters. Parameter n controls the "curvature" of the p_c-S function; α quantifies the " level " of the plateau of the capillary pressure.

The effective saturation S_{we} of the wetting fluid phase is defined by :

$$S_{we} = \frac{S_w - S_{wi}}{S_{max} - S_{wi}} \qquad \text{(A2)}$$

where S_{wi} is the irreducible saturation of the wetting fluid phase (here water) and S_m is the maximum saturation of the wetting fluid phase. During drainage of the porous medium, water is displaced for example by gas (or by a NAPL), the maximum saturation S_{max} is equal to 1.

On the other hand, when gas (or a NAPL) is displaced by water, in the case of imbibition, S_m is limited to values lower than 1 because the non wetting fluid phase will remain in the porous medium at residual saturation S_{nwr}. The maximum water saturation is therefore complementary to the residual saturation of the non wetting fluid phase : S_m=1-S_{gr} ; S_m=1-S_{or}.

In three-phase systems, for the interfaces oil/water and gas/oil, the capillary pressures p_{cow} and p_{cgo} are generally calculated from relation (A1) by applying a scaling approach based on the interfacial tensions of the two-phase system gas/water, gas/oil and oil/water (Parker et al, 1987):

$$p_{cow}(S_{we}) = \frac{1}{\beta_{ow}} p_{cgw}(S_{we}) \ , \qquad \text{(A3)}$$

where water is the wetting fluid phase

$$p_{cgo}(S_{we}) = \frac{1}{\beta_{go}} p_{cgw}(S_{we}) \ , \qquad \text{(A4)}$$

where oil is the wetting fluid phase.

$\beta_{ow} = \sigma_{gw}^0/\sigma_{ow}$ and $\beta_{go} = \sigma_{gw}^0/\sigma_{go}$ are the scaling factors for the fluid system oil/water and gas/oil; σ_{gw}^0, σ_{ow} and σ_{go} are the interfacial tension of fluid couples gas/water, oil/water and gas/oil.

A.2 Relative permeabilities in two-phase systems: water-gas, water-oil and oil-gas

In a two-phase water/gas system, using a modified Mualem-Van Genuchten (MVG) approach with a maximum value of the nonwetting fluid phase (here gas), the relative permeabilities are defined as:

$$k_{rw} = \sqrt{S_{we}}\left[1 - (1 - S_{we}^{1/m_{wg}})^{m_{wg}}\right]^2$$

$$k_{rg} = k_{rgw,max}\sqrt{1 - S_{we}}\left[1 - S_{we}^{1/m_{gw}}\right]^{2m_{gw}} \qquad \text{(A5)}$$

where $k_{rgw,max}$ is the maximum relative gas permeability achieved at irreducible water saturation S_{wi} in the gas/water system. m_{wg} and m_{gw} correspond to the MVG parameter for water and gas, respectively.

In a two-phase water/oil system, the relative permeabilities are then written as follows :

$$k_{rw} = \sqrt{S_{we}}\left[1 - (1 - S_{we}^{1/m_{wo}})^{m_{wo}}\right]^2$$

$$k_{row} = k_{row,max}\sqrt{1 - S_{we}}\left[1 - S_{we}^{1/m_{ow}}\right]^{2m_{ow}} \quad \text{(A6)}$$

where $k_{row,max}$ is the maximum relative oil permeability achieved at irreducible water saturation S_{wi} in the water/oil system. m_{wo} and m_{ow} correspond to the MVG parameter for water and gas, respectively.

In a two-phase oil/gas system, the corresponding relative permeabilities can be expressed by

$$k_{rg} = k_{rgo,max}\sqrt{1 - S_{oe}}\left[1 - S_{oe}^{1/m_{go}}\right]^{2m_{go}}$$

$$k_{rog} = \sqrt{S_{oe}}\left[1 - (1 - S_{oe}^{1/m_{og}})^{m_{og}}\right]^2 \quad \text{(A7)}$$

where $k_{rgo,max}$ is the maximum relative gas permeability achieved at residual oil saturation in the oil/gas system $S_{or.}$ m_{og} and m_{go} correspond to the MVG parameter for oil and gas, respectively. Here S_{oe} is the effective oil saturation defined by

$$S_{oe} = \frac{S_o - S_{or}}{1 - S_{or}} \quad \text{(A8)}$$

and S_o is the oil saturation.

Appendix B. Implementation of the mechanistic model of Shahverdi and Sohrabi (2017)

The three-phase relative permeabilities of the mechanistic model of Shahverdi and Sohrabi (2017) form a coupled nonlinear system of Eqs. (1) to (3) called Eqs. (B1) to (B3). We describe how the six two-phase relative permeabilities that appear in Eqs. (B1), (B2) and (B3), are expressed when using the Mualem-Van Genuchten model.

B.1 Three-phase relative permeability of the oil phase (k_{ro})

The three-phase relative permeability of the oil phase is expressed by

$$k_{ro} = \frac{S_{wo}}{S_{wo}+S_{go}} k_{row}(S_{ow}) + \frac{S_{go}}{S_{wo}+S_{go}} k_{rog}(S_{og}) \qquad \text{(B1)}$$

where :

$$S_{ow} = A_{ow}S_o \quad (B2a); \quad S_{og} = A_{og}S_o \ (B2b) \ ; \ S_{wo} = A_{wo}S_w \quad (B2c), \quad S_{go} = A_{go}S_g \ (B2d)$$

and becomes

$$k_{ro} = \frac{A_{wo}S_w}{A_{wo}S_w+A_{go}S_g} k_{row}(A_{ow}S_o) + \frac{A_{go}S_g}{A_{wo}S_w+A_{go}S_g} k_{rog}(A_{og}S_o) \qquad \text{(B3)}$$

Using the two-phase relative permeability of oil in a water-oil system, expressed by the ("modified") Mualem-Van Genuchten model:

$$k_{row} = k_{row,max}\sqrt{(1-S_{we})}\left[1-S_{we}^{1/m_{ow}}\right]^{2m_{ow}} = k_{row,max}\sqrt{\left[1-\left(\frac{S_w^{ow}-S_{wi}^{ow}}{1-S_{wi}^{ow}}\right)\right]}\left[1-\left(\frac{S_w^{ow}-S_{wi}^{ow}}{1-S_{wi}^{ow}}\right)^{1/m_{ow}}\right]^{2m_{ow}} \qquad \text{(B4)}$$

Since k_{row} has to be picked up at the representative two-phase saturation S_{ow}, using expression (B2a), Equation B4 can then be expressed as function of the oil saturation (S_o) in the three-phase system as follows:

$$k_{row} = k_{row,max}\sqrt{\left[1-\left(\frac{1-A_{ow}S_o-S_{wi}^{ow}}{1-S_{wi}^{ow}}\right)\right]}\left[1-\left(\frac{1-A_{ow}S_o-S_{wi}^{ow}}{1-S_{wi}^{ow}}\right)^{1/m_{ow}}\right]^{2m_{ow}} \qquad \text{(B5)}$$

Using the two-phase relative permeability of oil in an oil-gas system, expressed by the Mualem-Van Genuchten model:

$$k_{rog} = \sqrt{S_{oe}}\left[1-(1-S_{oe}^{1/m_{og}})^{m_{og}}\right]^2 = \sqrt{\left[\left(\frac{S_o^{og}-S_{or}^{og}}{1-S_{or}^{og}}\right)\right]}\left[1-(1-(\frac{S_o^{og}-S_{or}^{og}}{1-S_{or}^{og}})^{1/m_{og}})^{m_{og}}\right]^2 \qquad \text{(B6)}$$

Since k_{rog} has to be picked up at the representative two-phase saturation S_{og}, using expression (B2b), Eq. (B6) can then be expressed as function of the oil saturation (S_o) in the three-phase system as follows:

$$k_{rog} = \sqrt{\left[\left(\frac{A_{og}S_o-S_{or}^{og}}{1-S_{or}^{og}}\right)\right]}\left[1-(1-(\frac{A_{og}S_o-S_{or}^{og}}{1-S_{or}^{og}})^{1/m_{og}})^{m_{og}}\right]^2 \qquad \text{(B7)}$$

Finally, inserting Eqs. (B5) and (B7) in Eq. (B3), one obtains the final expression of the relative oil permeability in the three-phase system:

$$k_{ro} = \frac{A_{wo}S_w}{A_{wo}S_w+A_{go}S_g} kr_{ow,max}\sqrt{\left[1-\left(\frac{1-A_{ow}S_o-S_{wi}^{ow}}{1-S_{wi}^{ow}}\right)\right]}\left[1-\left(\frac{1-A_{ow}S_o-S_{wi}^{ow}}{1-S_{wi}^{ow}}\right)^{1/m_{ow}}\right]^{2m_{ow}} + \frac{A_{go}S_g}{A_{wo}S_w+A_{go}S_g}\sqrt{\left[\left(\frac{A_{og}S_o-S_{or}^{og}}{1-S_{or}^{og}}\right)\right]}\left[1-(1-(\frac{A_{og}S_o-S_{or}^{og}}{1-S_{or}^{og}})^{1/m_{og}})^{m_{og}}\right]^2 \qquad \text{(B8)}$$

Note that in Eq. (B8), one has to be respect the following constraints:

$$1-A_{ow}S_o-S_{wi}^{ow} \geq 0 \ ; \ A_{og}S_o-S_{or}^{og} \geq 0$$

B.2 Three-phase relative permeability of the water phase (k_{rw})

The three-phase relative permeability of the water phase is expressed by

$$k_{rw} = \frac{S_{ow}}{S_{ow}+S_{gw}} k_{rwo}(S_{wo}) + \frac{S_{gw}}{S_{ow}+S_{gw}} k_{rwg}(S_{wg}) \qquad \text{(B9)}$$

where :

$$S_{gw} = A_{gw}S_g \quad (B9a); \quad S_{wg} = A_{wg}S_w \; (B9b)$$

and becomes

$$k_{rw} = \frac{A_{ow}S_o}{A_{ow}S_o+A_{gw}S_g} k_{rwo}(A_{wo}S_w) + \frac{A_{gw}S_g}{A_{ow}S_o+A_{gw}S_g} k_{rwg}(A_{wg}S_w) \quad \text{(B10)}$$

Using the two-phase relative permeability of water in a water-oil system, expressed by the Mualem-Van Genuchten model:

$$k_{rwo} = \sqrt{S_{we}}\left[1-(1-S_{we}^{1/m_{wo}})^{m_{wo}}\right]^2 = \sqrt{\left[\left(\frac{S_w^{wo}-S_{wi}^{wo}}{1-S_{wi}^{wo}}\right)\right]}\left[1-(1-(\frac{S_w^{wo}-S_{wi}^{wo}}{1-S_{wi}^{wo}})^{1/m_{wo}})^{m_{wo}}\right]^2 \quad \text{(B11)}$$

Since k_{rwo} has to be picked up at the representative two-phase saturation S_{wo}, using expression (B2c), Eq. (B11) can then be expressed as function of the water saturation (S_w) in the three-phase system as follows:

$$k_{rwo} = \sqrt{\left[\left(\frac{A_{wo}S_w-S_{wi}^{wo}}{1-S_{wi}^{wo}}\right)\right]}\left[1-(1-(\frac{A_{wo}S_w-S_{wi}^{wo}}{1-S_{wi}^{wo}})^{1/m_{wo}})^{m_{wo}}\right]^2 \quad \text{(B12)}$$

Using the two-phase relative permeability of water in a water-gas system, expressed by the Mualem-Van Genuchten model:

$$k_{rwg} = \sqrt{S_{we}}\left[1-(1-S_{we}^{1/m_{wg}})^{m_{wg}}\right]^2 = \sqrt{\left[\left(\frac{S_w^{wg}-S_{wi}^{wg}}{1-S_{wi}^{wg}}\right)\right]}\left[1-(1-(\frac{S_w^{wg}-S_{wi}^{wg}}{1-S_{wi}^{wg}})^{1/m_{wg}})^{m_{wg}}\right]^2 \quad \text{(B13)}$$

Since k_{rwg} has to be picked up at the representative two-phase saturation S_{wg}, using expression (B9b), Equation B13 can then be expressed as function of the water saturation (S_w) in the three-phase system as follows:

$$k_{rwg} = \sqrt{\left[\left(\frac{A_{wg}S_w-S_{wi}^{wg}}{1-S_{wi}^{wg}}\right)\right]}\left[1-(1-(\frac{A_{wg}S_w-S_{wi}^{wg}}{1-S_{wi}^{wg}})^{1/m_{wg}})^{m_{wg}}\right]^2 \quad \text{(B14)}$$

Finally, inserting Eqs. (B12) and (B14) in Eq. (B10), one obtains the final expression of the relative water permeability in the three-phase system:

$$k_{rw} = \frac{A_{ow}S_o}{A_{ow}S_o+A_{gw}S_g}\sqrt{\left[\left(\frac{A_{wo}S_w-S_{wi}^{wo}}{1-S_{wi}^{wo}}\right)\right]}\left[1-(1-(\frac{A_{wo}S_w-S_{wi}^{wo}}{1-S_{wi}^{wo}})^{1/m_{wo}})^{m_{wo}}\right]^2 + \frac{A_{gw}S_g}{A_{ow}S_o+A_{gw}S_g}\sqrt{\left[\left(\frac{A_{wg}S_w-S_{wi}^{wg}}{1-S_{wi}^{wg}}\right)\right]}\left[1-(1-(\frac{A_{wg}S_w-S_{wi}^{wg}}{1-S_{wi}^{wg}})^{1/m_{wg}})^{m_{wg}}\right]^2 \quad \text{(B15)}$$

Note that in Eq. (B15), one has to be respect the following constraints:

$$A_{wo}S_w - S_{wi}^{wo} \geq 0 \; ; \; A_{wg}S_w - S_{wi}^{wg} \geq 0$$

B.3 <u>Three-phase relative permeability of the gas phase (k_{rg})</u>

The three-phase relative permeability of the gas phase is expressed by

$$k_{rg} = \frac{S_{wg}}{S_{og}+S_{wg}} k_{rgw}(S_{gw}) + \frac{S_{og}}{S_{og}+S_{wg}} k_{rgo}(S_{go}) \qquad \text{(B16)}$$

and takes the following form:

$$k_{rg} = \frac{A_{wg}S_w}{A_{og}S_o+A_{wg}S_w} k_{rgw}(S_{gw}) + \frac{A_{og}S_o}{A_{og}S_o+A_{wg}S_w} k_{rgo}(S_{go}) \quad \text{(B17)}$$

Using the two-phase relative permeability of gas in a water-gas system, expressed by the ("modified") Mualem-Van Genuchten model:

$$k_{rgw} = k_{rgw,max}\sqrt{(1-S_{we})}\left[1-S_{we}^{1/m_{gw}}\right]^{2m_{gw}} = k_{rgw,max}\sqrt{\left[1-\left(\frac{S_w^{gw}-S_{wi}^{gw}}{1-S_{wi}^{gw}}\right)\right]}\left[1-\left(\frac{S_w^{gw}-S_{wi}^{gw}}{1-S_{wi}^{gw}}\right)^{1/m_{gw}}\right]^{2m_{gw}} \quad \text{(B18)}$$

Since k_{rgw} has to be picked up at the representative two-phase saturation S_{gw}, using expression (B9a), Eq. (B18) can then be expressed as function of the gas saturation (S_g) in the three-phase system as follows:

$$k_{rgw} = k_{rgw,max}\sqrt{\left[1-\left(\frac{1-A_{gw}S_g-S_{wi}^{gw}}{1-S_{wi}^{gw}}\right)\right]}\left[1-\left(\frac{1-A_{gw}S_g-S_{wi}^{gw}}{1-S_{wi}^{gw}}\right)^{1/m_{gw}}\right]^{2m_{gw}} \quad \text{(B19)}$$

Using the two-phase relative permeability of gas in an oil-gas system, expressed by the ("modified") Mualem-Van Genuchten model:

$$k_{rgo} = k_{rgo,max}\sqrt{(1-S_{oe})}\left[1-S_{oe}^{1/m_{go}}\right]^{2m_{go}} = k_{rgo,max}\sqrt{\left[1-\left(\frac{S_o^{go}-S_{or}^{go}}{1-S_{or}^{go}}\right)\right]}\left[1-\left(\frac{S_o^{go}-S_{or}^{go}}{1-S_{or}^{go}}\right)^{1/m_{go}}\right]^{2m_{go}} \quad \text{(B20)}$$

Since k_{rgo} has to be picked up at the representative two-phase saturation S_{go}, using expression (B2d), Eq. (B20) can then be expressed as function of the gas saturation (S_g) in the three-phase system as follows:

$$k_{rgo} = k_{rgo,max}\sqrt{\left[1-\left(\frac{1-A_{go}S_g-S_{or}^{go}}{1-S_{or}^{go}}\right)\right]}\left[1-\left(\frac{1-A_{go}S_g-S_{or}^{go}}{1-S_{or}^{go}}\right)^{1/m_{go}}\right]^{2m_{go}} \quad \text{(B21)}$$

Finally, inserting Eqs. (B19) and (B21) in Eq. (B17), one obtains the final expression of the relative gas permeability in the three-phase system:

$$k_{rg} = \frac{A_{wg}S_w}{A_{og}S_o+A_{wg}S_w}k_{rgw,max}\sqrt{\left[1-\left(\frac{1-A_{gw}S_g-S_{wi}^{gw}}{1-S_{wi}^{gw}}\right)\right]}\left[1-\left(\frac{1-A_{gw}S_g-S_{wi}^{gw}}{1-S_{wi}^{gw}}\right)^{1/m_{gw}}\right]^{2m_{gw}} + \frac{A_{og}S_o}{A_{og}S_o+A_{wg}S_w}k_{rgo,max}\sqrt{\left[1-\left(\frac{1-A_{go}S_g-S_{or}^{go}}{1-S_{or}^{go}}\right)\right]}\left[1-\left(\frac{1-A_{go}S_g-S_{or}^{go}}{1-S_{or}^{go}}\right)^{1/m_{go}}\right]^{2m_{go}} \quad \text{(B22)}$$

Note that in Eq. (B22), one has to be respect the following constraints:

$$1-A_{gw}S_g-S_{wi}^{gw} \geq 0\ ;\ 1-A_{go}S_g-S_{or}^{go} \geq 0$$

Appendix C. Quantified MVG parameters of the experimental two-phase constitutive relationships

Table C1 and Table C2 summarize the Mualem-Van Genuchten (MVG) parameters quantified for the Bentheimer sandstone and Berea sandstone. The numerical values obtained by a nonlinear fit of the theoretical Pc-S and kr-S curves (Appendix A) against the experimentally observed curves using the NLFiT tool of Origin 2019 with the Levenberg-Marquardt iteration algorithm.

The tables specify uncertainty intervals (standard errors) associated with model parameter estimates. R-squared values are indicated as statistical measure when suitable to underline how close the experimental data are to the fitted curve.

Table C1. Bentheimer sandstone

Two-phase relative permeability curve		
Water-Oil system		
S_{wi} [-]	0.089	R-squared
m_{wo} [-]	0.876±0.013	0.9925
m_{ow} [-]	1.021±0.011	0.9939
$k_{row,max}$ [-]	0.841	
Water-Gas system		
S_{wi} [-]	0.234	R-squared
m_{wg} [-]	0.972±0.019	0.9941
m_{gw} [-]	1.150±0.014	0.9981
$k_{rgw,max}$ [-]	0.475	
Oil-Gas system		
S_{or} [-]	0.207	R-squared
m_{og} [-]	1.036±0.014	0.9971
m_{go} [-]	1.262±0.020	0.9954
$k_{rgo,max}$ [-]	0.657	

Two-phase capillary pressure curve		
Water-Gas system		
		R-squared
S_{wi} [-]	0.111±0.003	
m [-]	0.810±0.015	0.986
α [Pa^{-1}]	$1.96\times10^{-4}\pm1.02\times10^{-5}$	

Table C2. Berea sandstone

Two-phase relative permeability curve		
Water-Oil system		
S_{wi} [-]	0.264	R-squared
m_{wo} [-]	0.806±0.014	0.9926
m_{ow} [-]	0.847±0.013	0.9909
$k_{row,max}$ [-]	0.892	
Water-Gas system		
S_{wi} [-]	0.384	R-squared
m_{wg} [-]	0.912±0.030	0.9718
m_{gw} [-]	1.050±0.009	0.9965
$k_{rgw,max}$ [-]	0.727	
Oil-Gas system		
S_{or} [-]	0.259	R-squared
m_{og} [-]	0.845±0.022	0.9738
m_{go} [-]	0.813±0.009	0.9969
$k_{rgo,max}$ [-]	0.827	

Two-phase capillary pressure curve		
Water-Oil system		R-squared
S_{wi} [-]	0.100±0.106	
m [-]	0.299±0.119	0.9831
α [Pa^{-1}]	$2.56\times10^{-4}\pm2.82\times10^{-5}$	
Fixed S_{wi}=0.264	m=0.538±0.263 $\alpha= 8.01\times10^{-5}\pm2.1\times10^{-4}$	
Water-Gas system		R-squared
S_{wi} [-]	0.147±0.083	
m [-]	0.324±0.085	0.9949
α [Pa^{-1}]	$8.05\times10^{-5}\pm3.94\times10^{-5}$	
Oil-Gas system		R-squared
S_{or} [-]	0.149±0.044	
m [-]	0.392±0.090	0.9876
α [Pa^{-1}]	$1.29\times10^{-4}\pm8.07\times10^{-5}$	
Fixed S_{wi}=0.259	m=0,491±0,504 $\alpha= 1.33\times10^{-4}\pm7.0\times10^{-4}$	

Appendix D. Comparison of predicted k_r values (water, oil, gas) for Oak's DDI Experiments 17 and 18 with the findings of Shahverdi and Sohrabi (2017)

Figs. D1 – D3 and Figs. D4 –D6 present the detailed comparison of relative permeabilities for water, oil and gas of Oak's DDI experiments 17 and 18 using the mechanistic model. Here we compare our numerical results obtained with those referenced in Shahverdi and Sohrabi (2017).
To quantify the goodness of the prediction of the measured k_r values, the root mean square error (RMSE) and the coefficient of residual mass (CRM) are indicated.

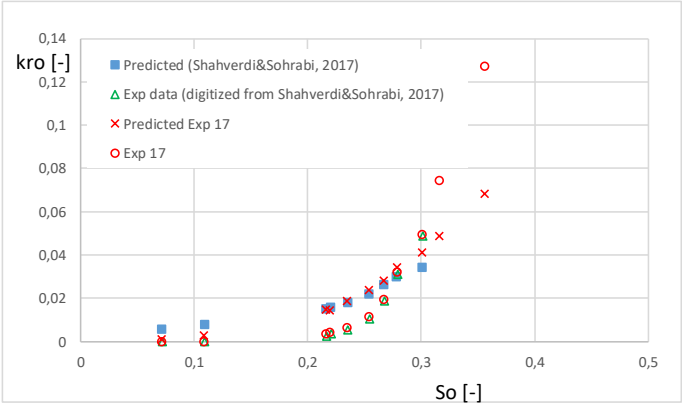

Predicted (Shahverdi&Sohrabi,2017)	RMSE= 0.0103	CRM= -0.454
Predicted Exp 17	RMSE= 0.0079	CRM= 0.097

Fig. D1. Comparison of three-phase oil relative permeability as function of oil saturation measured from Oak's DDI Experiment 17 (G2) and that predicted with the mechanistic model.

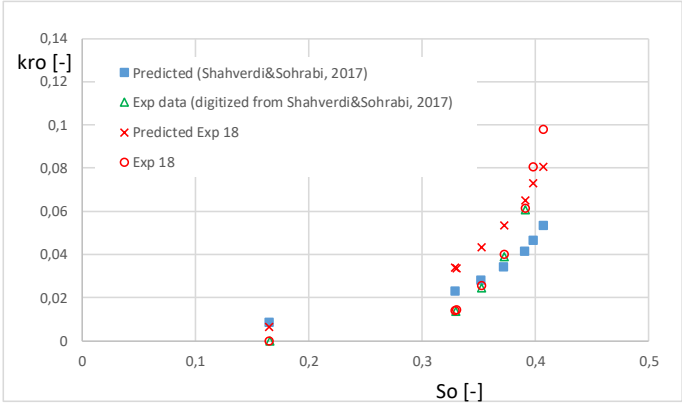

Predicted (Shahverdi&Sohrabi,2017)	RMSE= 0.0106	CRM= 0.0187
Predicted Exp 18	RMSE= 0.0144	CRM= -0.164

Fig. D4. Comparison of three-phase oil relative permeability as function of oil saturation measured from Oak's DDI Experiment 18 (G3) and that predicted with the mechanistic model.

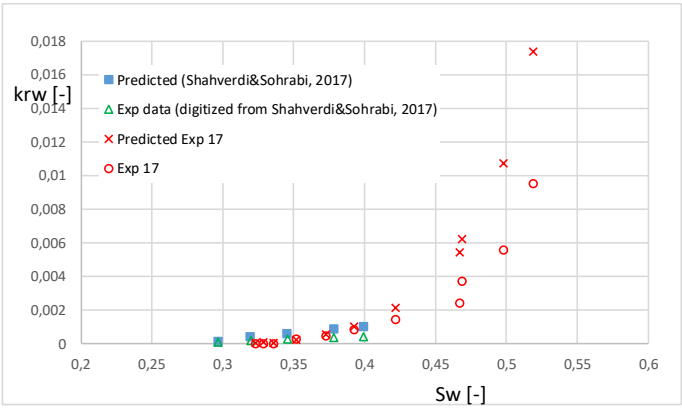

Predicted (Shahverdi&Sohrabi,2017)	RMSE= 0.0004	CRM= -1.280
Predicted Exp 17	RMSE= 0.0031	CRM= -0.808

Fig. D2. Comparison of three-phase water relative permeability as function of water saturation measured from Oak's DDI Experiment 17 (G2) and that predicted with the mechanistic model.

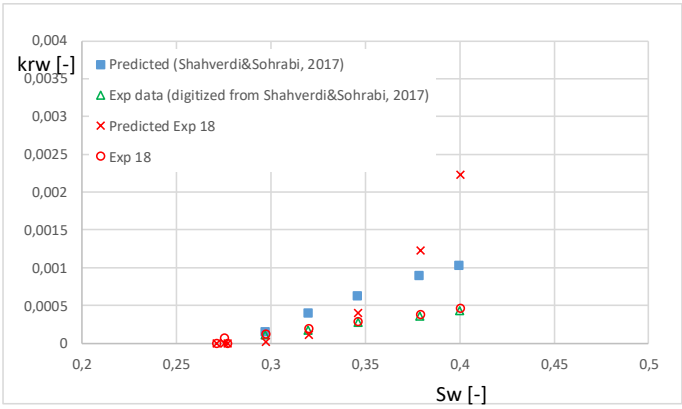

Predicted (Shahverdi&Sohrabi,2017)	RMSE= 0.0004	CRM= -1.314
Predicted Exp 18	RMSE= 0.0007	CRM= -1.646

Fig. D5. Comparison of three-phase water relative permeability as function of water saturation measured from Oak's DDI Experiment 18 (G3) and that predicted with the mechanistic model.

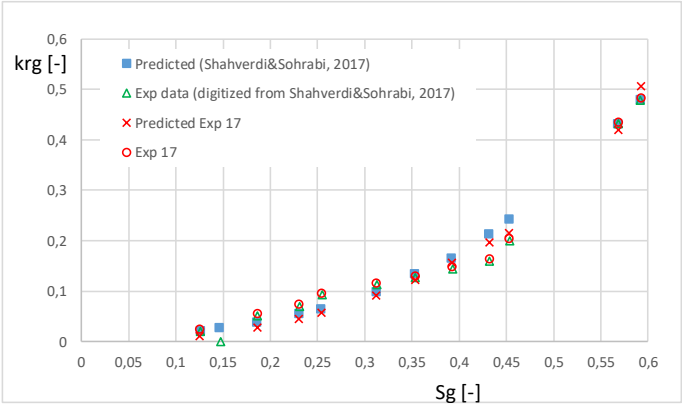

Predicted (Shahverdi&Sohrabi,2017)	RMSE= 0.0249	CRM= -0.049
Predicted Exp 17	RMSE= 0.0230	CRM= 0.043

Fig. D3. Comparison of three-phase gas relative permeability as function of gas saturation measured from Oak's DDI Experiment 17 (G2) and that predicted with the mechanistic model.

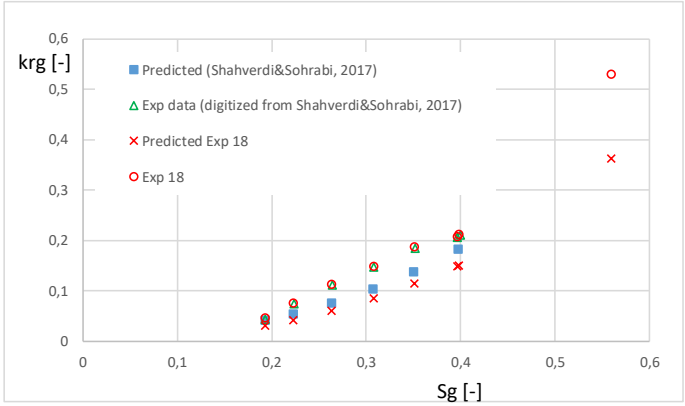

Predicted (Shahverdi&Sohrabi,2017)	RMSE= 0.0323	CRM= 0.389
Predicted Exp 18	RMSE= 0.0778	CRM= 0.346

Fig. D6. Comparison of three-phase gas relative permeability as function of gas saturation measured from Oak's DDI Experiment 18 (G3) and that predicted with the mechanistic model.

Appendix E. Boundary conditions and numerical results of the TD compatible model

E.1 Boundary conditions: tangential and normal derivatives of global capillary pressure P_c^g

Let $\vec{\tau}$ and $\vec{n}$ be the tangential and normal unit vectors on $\partial\mathbb{T}$ (Fig. E1) defined by:

$$\begin{cases} \overrightarrow{\tau_{12}} = \overrightarrow{\imath_1} \;\; ; & \overrightarrow{n_{12}} = \dfrac{\sqrt{3}}{3}(\overrightarrow{\imath_1} - 2\overrightarrow{\imath_3}) & on\ \partial\mathbb{T}_{12}\ (water - oil\ edge)\ , \\ \overrightarrow{\tau_{13}} = \overrightarrow{\imath_3} - \overrightarrow{\imath_1} \;\; ; & \overrightarrow{n_{13}} = \dfrac{\sqrt{3}}{3}(\overrightarrow{\imath_1} + \overrightarrow{\imath_3}) & on\ \partial\mathbb{T}_{13}\ (water - gas\ edge), \\ \overrightarrow{\tau_{32}} = \overrightarrow{\imath_3} \;\; ; & \overrightarrow{n_{32}} = \dfrac{\sqrt{3}}{3}(\overrightarrow{\imath_3} - 2\overrightarrow{\imath_1}) & on\ \partial\mathbb{T}_{13}\ (gas - oil\ edge)\ , \end{cases} \qquad \text{(E1)}$$

where $\overrightarrow{\imath_1}$and $\overrightarrow{\imath_3}$ are the unit vectors of the (Os_1,Os_3) system of non-orthogonal axis.

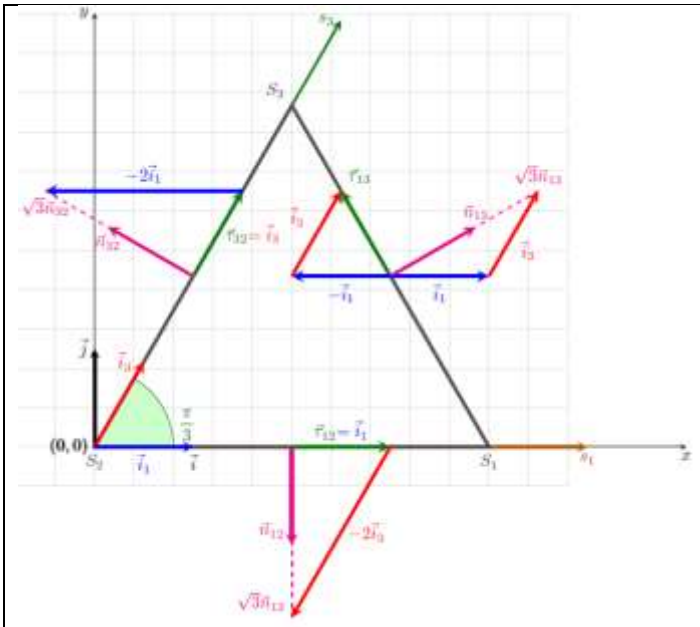

Fig. E1. Definition of tangential and normal unit vectors on $\partial\mathbb{T}$. Note that the summit of oil (S_2=1) is chosen as the origin of the orthogonal (Ox,Oy) and non-orthogonal (Os_1, Os_3) system.

The global capillary pressure P_c^g being function of s_1 and s_3, the tangential and normal derivatives of P_c^g on $\partial\mathbb{T}$, $\frac{\partial P_c^g}{\partial \tau}$ and $\frac{\partial P_c^g}{\partial n}$, are then given by :

$$\begin{cases} \dfrac{\partial P_c^g}{\partial \tau} = \dfrac{\partial P_c^g}{\partial s_1} \;\; ; & \dfrac{\partial P_c^g}{\partial n} = \dfrac{\sqrt{3}}{3}\left(\dfrac{\partial P_c^g}{\partial s_1} - 2\dfrac{\partial P_c^g}{\partial s_3}\right) & on\ \partial\mathbb{T}_{12}\ (water - oil\ edge)\ , \\ \dfrac{\partial P_c^g}{\partial \tau} = \dfrac{\partial P_c^g}{\partial s_3} - \dfrac{\partial P_c^g}{\partial s_1} \;\; ; & \dfrac{\partial P_c^g}{\partial n} = \dfrac{\sqrt{3}}{3}\left(\dfrac{\partial P_c^g}{\partial s_1} + \dfrac{\partial P_c^g}{\partial s_3}\right) & on\ \partial\mathbb{T}_{13}\ (water - gas\ edge), \\ \dfrac{\partial P_c^g}{\partial \tau} = \dfrac{\partial P_c^g}{\partial s_3} \;\; ; & \dfrac{\partial P_c^g}{\partial n} = \dfrac{\sqrt{3}}{3}\left(\dfrac{\partial P_c^g}{\partial s_3} - 2\dfrac{\partial P_c^g}{\partial s_1}\right) & on\ \partial\mathbb{T}_{13}\ (gas - oil\ edge)\ , \end{cases} \qquad \text{(E2)}$$

In order to perform C1 finite element interpolation in the orthogonal (Ox,Oy) system, the non-orthogonal vectors $\overrightarrow{\imath_1}$ and $\overrightarrow{\imath_3}$ must be projected on the unit vectors of the (Ox,Oy) system, $\vec{\imath}$ and $\vec{\jmath}$, as follows:

$$\begin{cases} \overrightarrow{\imath_1} = \vec{\imath} \\ \overrightarrow{\imath_3} = \frac{1}{2}\vec{\imath} + \frac{\sqrt{3}}{2}\vec{\jmath} \end{cases} \qquad \text{(E3)}$$

We can then re-write the tangential derivatives of P_c^g in terms of x and y derivatives and the normal derivatives of P_c^g as follows:

$$\begin{cases} \frac{\partial P_c^g}{\partial x} = \frac{\partial P_c^g}{\partial s_1} \;\; ; \;\; \frac{\partial P_c^g}{\partial y} = 0 \;\; ; \;\; \frac{\partial P_c^g}{\partial n} = \frac{\sqrt{3}}{3}\frac{\partial P_c^g}{\partial s_1} \quad on\ \partial\mathbb{T}_{12}\ (water - oil\ edge)\ , \\ \frac{\partial P_c^g}{\partial x} = \frac{1}{2}\frac{\partial P_c^g}{\partial s_3} - \frac{\partial P_c^g}{\partial s_1} \;\; ; \;\; \frac{\partial P_c^g}{\partial y} = \frac{\sqrt{3}}{2}\frac{\partial P_c^g}{\partial s_3} \;\; ; \;\; \frac{\partial P_c^g}{\partial n} = \frac{\sqrt{3}}{3}\left(\frac{\partial P_c^g}{\partial s_1} + \frac{\partial P_c^g}{\partial s_3}\right) \quad on\ \partial\mathbb{T}_{13}\ (water - gas\ edge), \\ \frac{\partial P_c^g}{\partial x} = \frac{1}{2}\frac{\partial P_c^g}{\partial s_3} \;\; ; \;\; \frac{\partial P_c^g}{\partial y} = \frac{\sqrt{3}}{2}\frac{\partial P_c^g}{\partial s_3} \quad \frac{\partial P_c^g}{\partial n} = \frac{\sqrt{3}}{3}\frac{\partial P_c^g}{\partial s_3} \quad on\ \partial\mathbb{T}_{13}\ (gas - oil\ edge)\ . \end{cases} \qquad \text{(E4)}$$

Note that the normal derivatives in Eq. (E4) are slightly modified with regard to Eq. (E2) as $\frac{\partial P_c^g}{\partial s_1} = 0$ and $\frac{\partial P_c^g}{\partial s_3} = 0$ on the gas-oil and the water-oil edge, respectively. After C1 finite interpolation of P_c^g on the whole ternary diagram, the numerical solutions in terms of x- and y- derivatives of P_c^g are projected along ($\overrightarrow{\iota_1}$, $\overrightarrow{\iota_3}$) to compute the corresponding derivatives such as:

$$\begin{cases} \frac{\partial P_c^g}{\partial s_1} = \frac{\partial P_c^g}{\partial x} - \frac{\sqrt{3}}{3}\frac{\partial P_c^g}{\partial y} \\ \frac{\partial P_c^g}{\partial s_3} = \frac{2\sqrt{3}}{3}\frac{\partial P_c^g}{\partial y} \end{cases} , \qquad \text{(E5)}$$

which are then used for computation of the water fractional flow (f_1) and gas fractional flow (f_3) as described in Eq. (17).

E.2 Results of the TD compatible model

E.2.1 Bentheimer sandstone

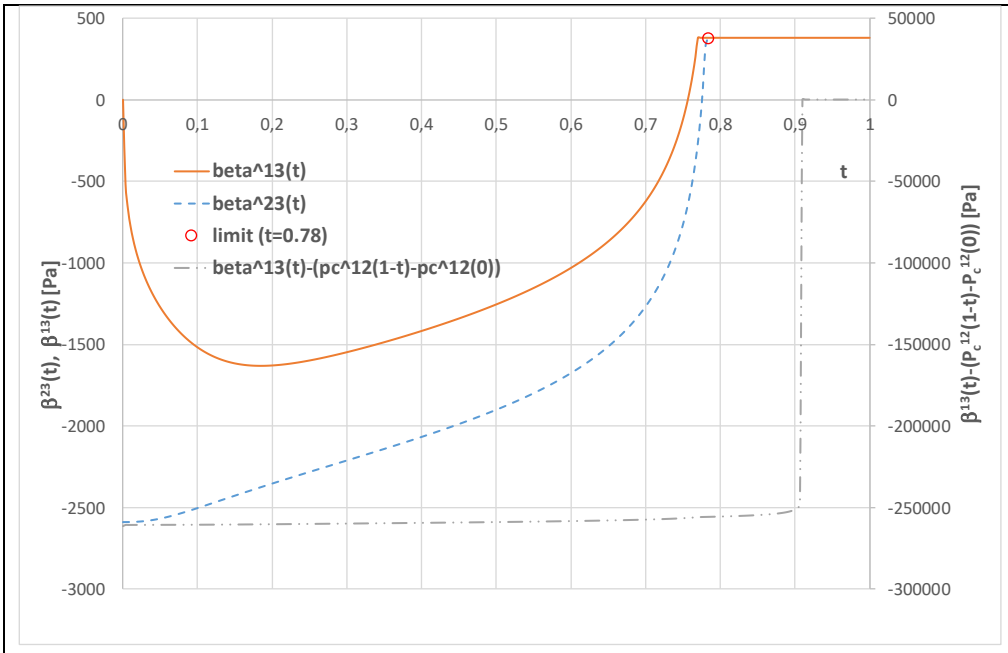

Type (a) of inequalities

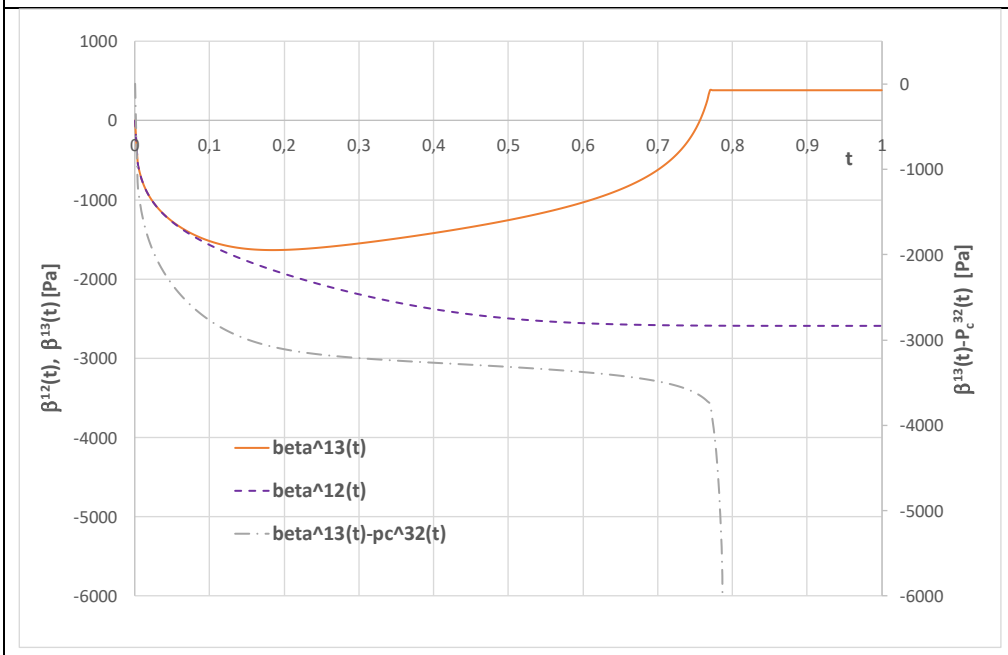

Type (b) of inequalities

Fig. E2. Verification of the TD compatible condition expressed by Eq. (16) in the case of Bentheimer sandstone.

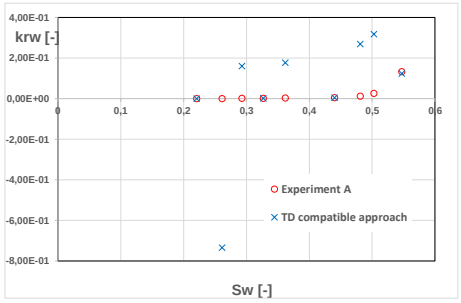

(a) RMSE=0.0961 ; CRM=-0.78

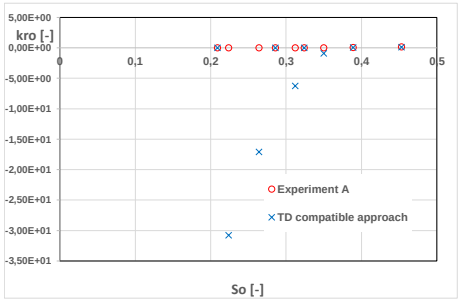

(b) RMSE=3.9749; CRM=206.75

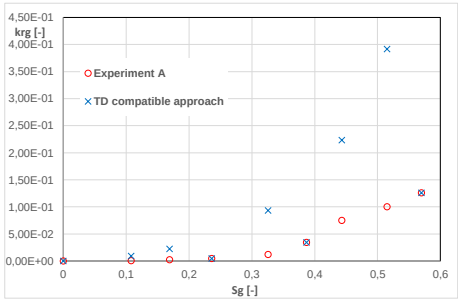

(c) RMSE= 0.0375; CRM=-1.55

Fig. E3. Relative permeabilities measured from Alizadeh's DDI Experiment A compared to those predicted with the TD compatible model: (a) water relative permeability versus water saturation, (b) oil relative permeability versus oil saturation, and (c) gas relative permeability versus gas saturation. The goodness of the prediction of the measured k_r values is indicated by the root mean square error (RMSE) and the coefficient of residual mass (CRM).

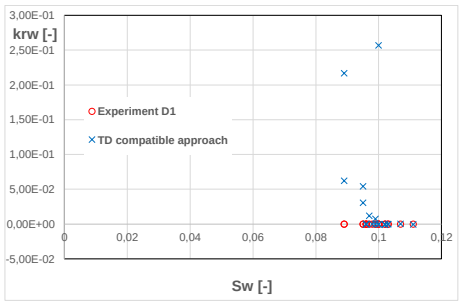

(a) RMSE= 0.0174 ; CRM= -

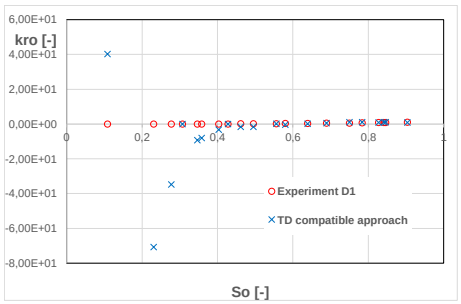

(b) RMSE= 4.471; CRM=14.15

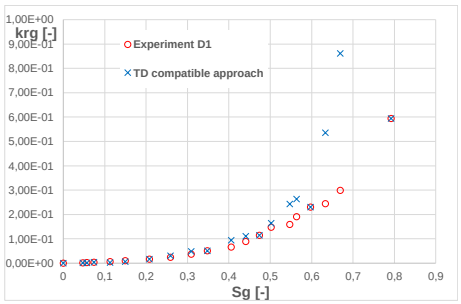

(c) RMSE=0.0322; CRM=-0.48

Fig. E4. Relative permeabilities measured from Alizadeh's DDI Experiment D1 compared to those predicted with the TD compatible model: (a) water relative permeability versus water saturation, (b) oil relative permeability versus oil saturation, and (c) gas relative permeability versus gas saturation. The goodness of the prediction of the measured k_r values is indicated by the root mean square error (RMSE) and the coefficient of residual mass (CRM).

E.2.2 Berea sandstone

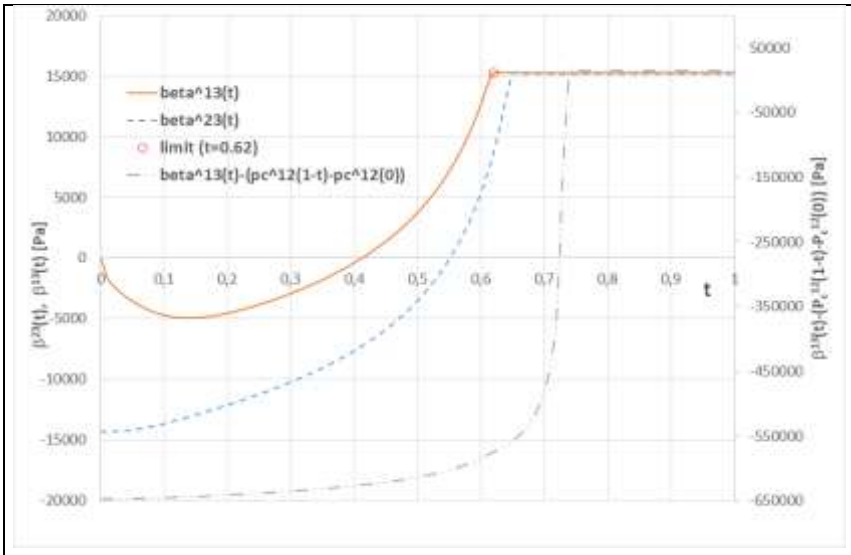

Type (a) of inequalities

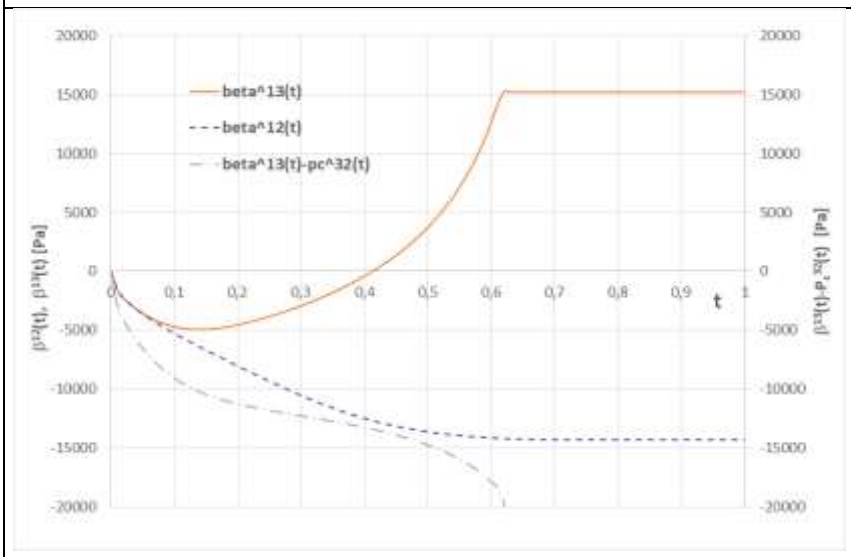

Type (b) of inequalities

Fig. E5. Verification of the TD compatible condition expressed by Eq. (16) in the case of Berea sandstone.

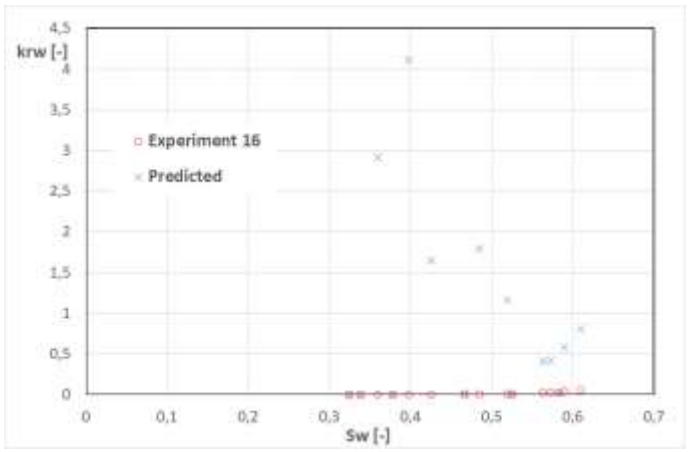

RMSE=0.388; CRM=-67.52

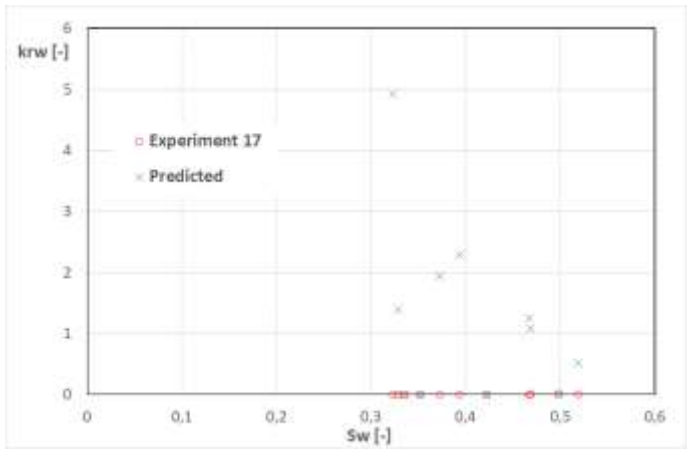

RMSE=0.562; CRM=-551.09

Fig. E6. Water relative permeabilities measured from Oak's DDI Experiments 16 and 17 compared to those predicted with the TD compatible model. The goodness of the prediction of the measured k_r values is indicated by the root mean square error (RMSE) and the coefficient of residual mass (CRM)

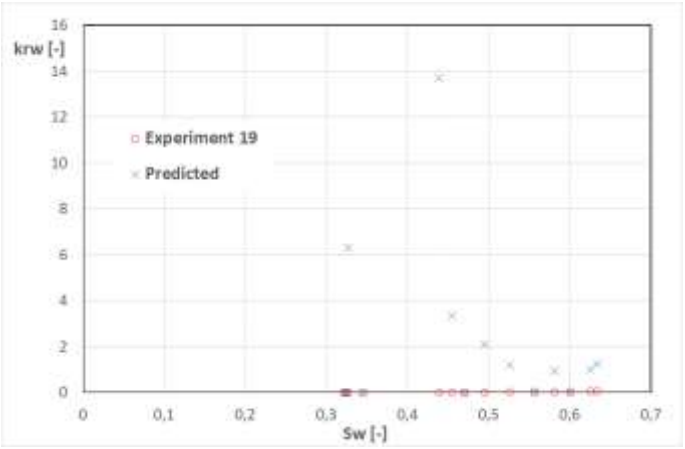

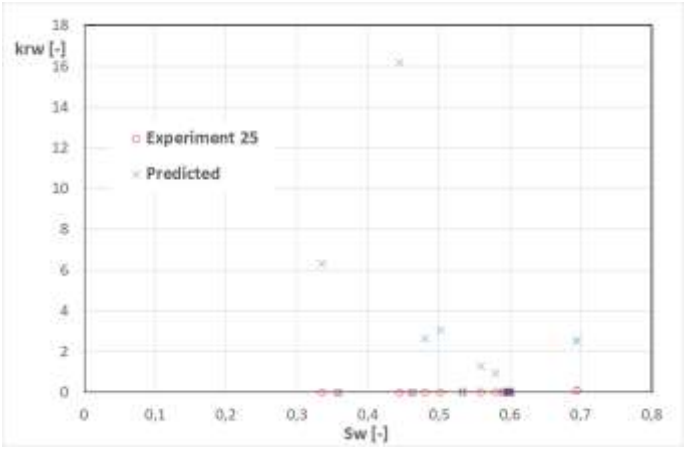

RMSE=1.124; CRM=-152.30	RMSE=1.013; CRM=-83.74

Fig. E7. Water relative permeabilities measured from Oak's DDI Experiments 19 and 25 compared to those predicted with the TD compatible model. The goodness of the prediction of the measured k_r values is indicated by the root mean square error (RMSE) and the coefficient of residual mass (CRM).

Appendix F. Parker-Lenhard model applied to Bentheimer sandstone (Alizadeh's DDI Experiments A and D1) and Berea sandstone (Oak's DDI Experiments 16-20 and 25)

F.1 Bentheimer sandstone

F.1.1 Input parameters determined for modeling options Pc-S and kr-S

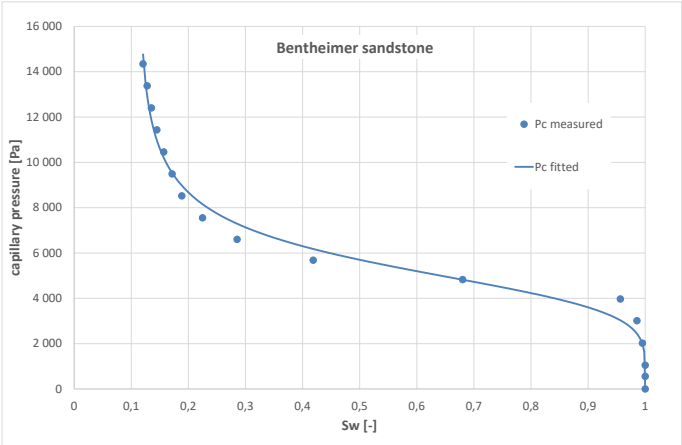

(a)

Option Pc-S; Calibrated model parameters (R-squared= 0.986):

S_{wi}=0.111±0.003; m=0.810±0.015; α=1.96×10^{-4}±1.02×10^{-5} Pa^{-1}

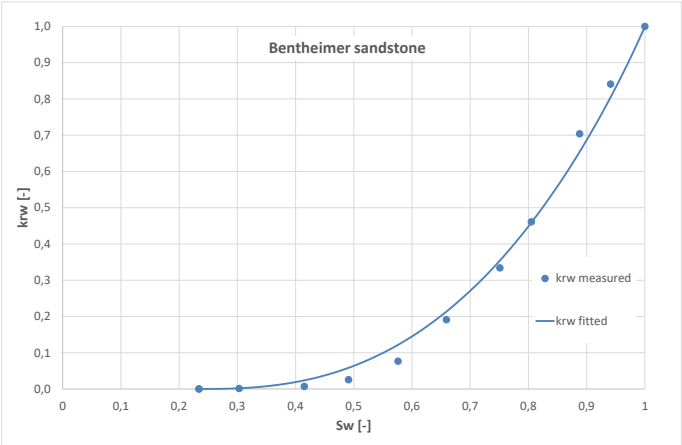

(b)

Option kr-S ; S_{wi}=0.234 (fixed)

Calibrated model parameter R-squared=0.994): m=0.972±0.019

Fig. F1. Measured and fitted two-phase constitutive relationships from the Alizadeh experiment on Bentheimer sandstone (Alizadeh and Piri, 2014b): (a) capillary pressure (in water-gas system) as function of water saturation, and (b) water-gas relative permeability versus water saturation.

F.1.2 Comparison of predicted k_r values (water, oil, gas) with those measured in DDI Experiments A and D1

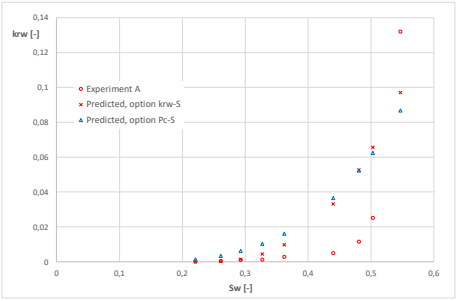

(a) Option kr-S : RMSE= 0.008187 ; CRM=-0.475

Option Pc-S : RMSE= 0.008882; CRM=-0.536

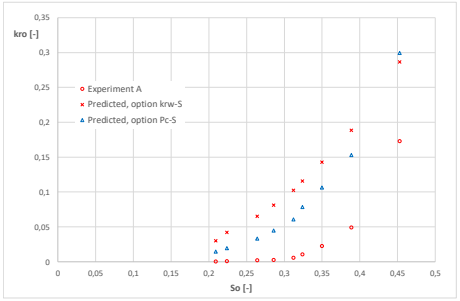

(b) Option kr-S : RMSE= 0.031406 ; CRM=-2.957

Option Pc-S : RMSE= 0.023534; CRM=-2.043

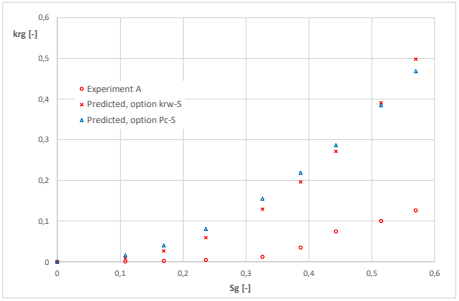

(c) Option kr-S : RMSE= 0.061391; CRM=-3.461

Option Pc-S : RMSE=0.061387; CRM=-3.660

Fig. F2. Relative permeabilities measured from Alizadeh's DDI Experiment A compared to those predicted (using option kr-S and option Pc-S): (a) water relative permeability versus water saturation, (b) oil relative permeability versus oil saturation, and (c) gas relative permeability versus gas saturation. The goodness of the prediction of the measured k_r values is indicated by the root mean square error (RMSE) and the coefficient of residual mass (CRM).

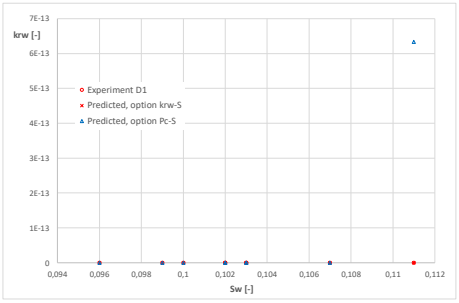	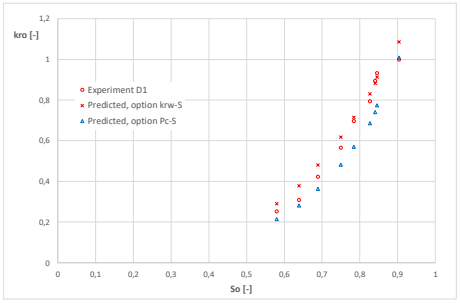	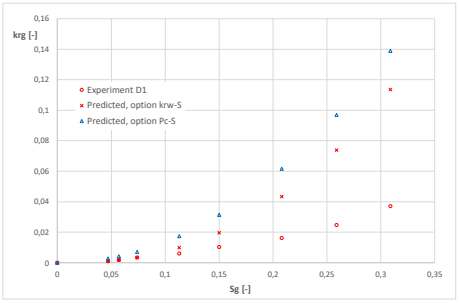
(a) Option kr-S : RMSE= 0;	(b) Option kr-S : RMSE=0.010435; CRM=-0.116	(c) Option kr-S : RMSE=0.048802; CRM=-1.389
Option Pc-S : RMSE= 3.1685E-14;	Option Pc-S : RMSE= 0.015410; CRM=0.083	Option Pc-S : RMSE=0.041904; CRM=-1.279

Fig. F3. Relative permeabilities measured from Alizadeh's DDI Experiment D1 compared to those predicted (using option kr-S and option Pc-S): (a) water relative permeability versus water saturation, (b) oil relative permeability versus oil saturation, and (c) gas relative permeability versus gas saturation. The goodness of the prediction of the measured k_r values is indicated by the root mean square error (RMSE) and the coefficient of residual mass (CRM).

F.2 Berea sandstone

F.2.1 Input parameters determined for modeling options Pc-S and kr-S

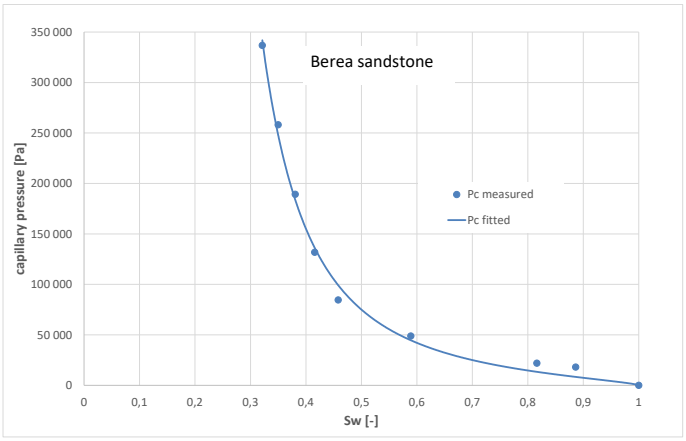	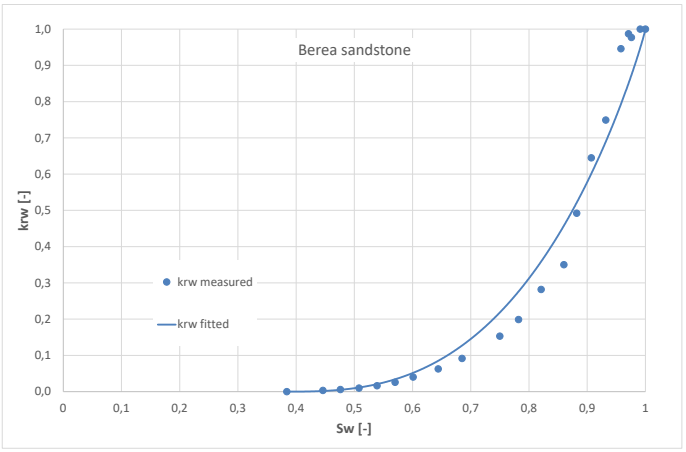
(a) Option Pc-S; Calibrated model parameters (R-squared= 0.995): S_{wi}=0.147±0.083; m=0.324±0.085; α=8.05×10^{-5}±3.94×10^{-5} Pa^{-1}	(b) Option kr-S ; S_{wi}=0.384 (fixed) Calibrated model parameter R-squared=0.972): m=0.912±0.03

Fig. F4. Measured and simulated two-phase constitutive relationships from Oak's experiment on Berea sandstone: (a) capillary pressure (in water-gas system) as function of water saturation, and (b) water-gas relative permeability versus water saturation

F.2.2 Comparison of predicted k_r values (water, oil, gas) with those measured in DDI Experiments 16-20 and 25

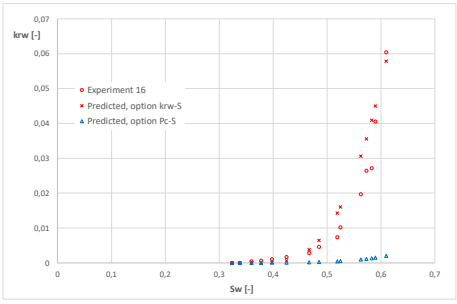	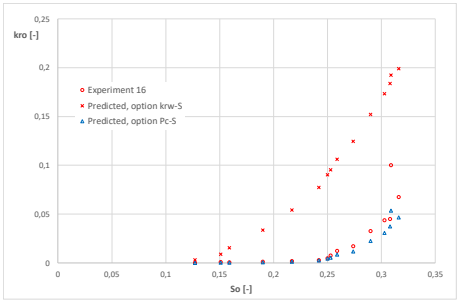	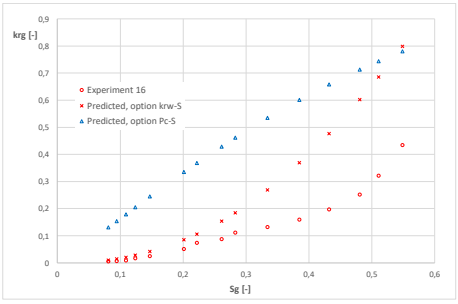
(a) Option kr-S : RMSE= 0.001502; CRM=-0.238	(b) Option kr-S : RMSE=0.023208; CRM=-3.473	(c) Option kr-S : RMSE=0.049039; CRM=-1.042
Option Pc-S : RMSE=0.005484; CRM=0.959	Option Pc-S : RMSE=0.003651; CRM=0.336	Option Pc-S : RMSE=0.085323; CRM=-2.473
Fig. F5. Relative permeabilities measured from Oak's DDI Experiment 16 compared to those predicted (using option kr-S and option Pc-S): (a) water relative permeability versus water saturation, (b) oil relative permeability versus oil saturation, and (c) gas relative permeability versus gas saturation. The goodness of the prediction of the measured k_r values is indicated by the root mean square error (RMSE) and the coefficient of residual mass (CRM).		

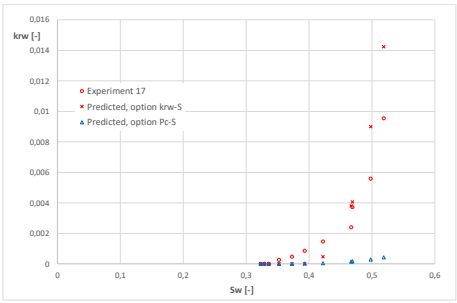	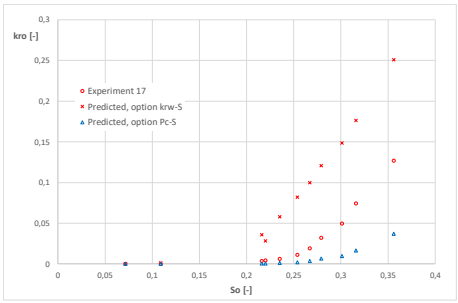	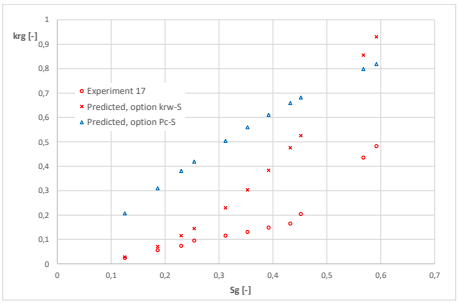
(a) Option kr-S : RMSE=0.000559; CRM=-0.300	(b) Option kr-S : RMSE=0.022128; CRM=-2.061	(c) Option kr-S : RMSE=0.074934; CRM=-1.103
Option Pc-S : RMSE=0.001043; CRM=0.952	Option Pc-S : RMSE=0.010788; CRM=0.765	Option Pc-S : RMSE=0.113529; CRM=-2.076
Fig. F6. Relative permeabilities measured from Oak's DDI Experiment 17 compared to those predicted (using option kr-S and option Pc-S): (a) water relative permeability versus water saturation, (b) oil relative permeability versus oil saturation, and (c) gas relative permeability versus gas saturation. The goodness of the prediction of the measured k_r values is indicated by the root mean square error (RMSE) and the coefficient of residual mass (CRM).		

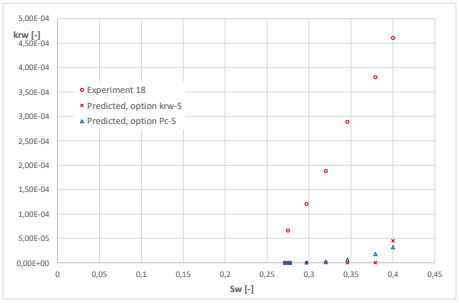	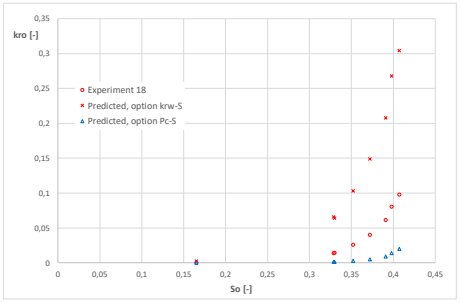	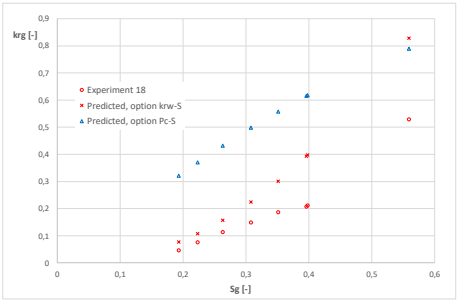
(a) Option kr-S : RMSE=8.43E-05; CRM=0.970	(b) Option kr-S : RMSE=0.043684; CRM=-2.484	(c) Option kr-S : RMSE=0.053159; CRM=-0.635
Option Pc-S : RMSE=8.37E-05; CRM=0.960	Option Pc-S : RMSE=0.015502; CRM=0.840	Option Pc-S : RMSE=0.120104; CRM=-1.767

Fig. F7. Relative permeabilities measured from Oak's DDI Experiment 18 compared to those predicted (using option kr-S and option Pc-S): (a) water relative permeability versus water saturation, (b) oil relative permeability versus oil saturation, and (c) gas relative permeability versus gas saturation. The goodness of the prediction of the measured k_r values is indicated by the root mean square error (RMSE) and the coefficient of residual mass (CRM).

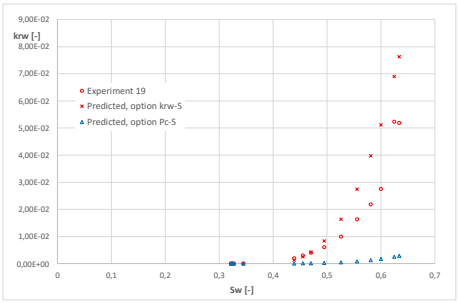	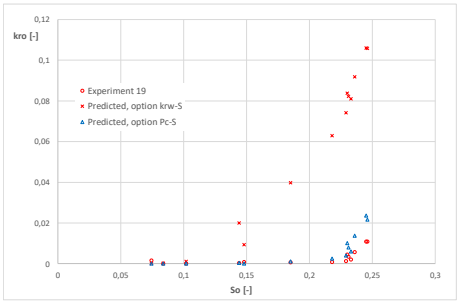	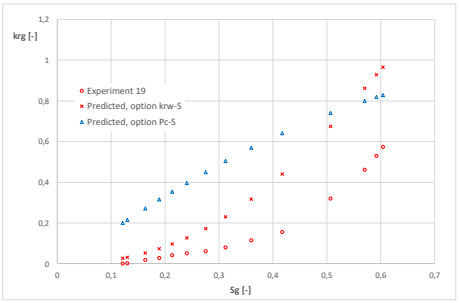
(a) Option kr-S : RMSE= 0.003131; CRM=-0.520	(b) Option kr-S : RMSE=0.016810; CRM=-16.682	(c) Option kr-S : RMSE=0.062688; CRM=-1.050
Option Pc-S : RMSE=0.005702; CRM=0.947	Option Pc-S : RMSE=0.001476; CRM=-1.131	Option Pc-S : RMSE=0.092081; CRM=-1.913

Fig. F8. Relative permeabilities measured from Oak's DDI Experiment 19 compared to those predicted (using option kr-S and option Pc-S): (a) water relative permeability versus water saturation, (b) oil relative permeability versus oil saturation, and (c) gas relative permeability versus gas saturation. The goodness of the prediction of the measured k_r values is indicated by the root mean square error (RMSE) and the coefficient of residual mass (CRM).

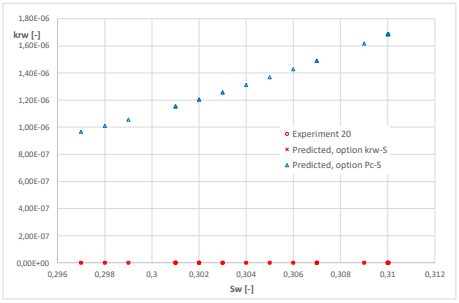	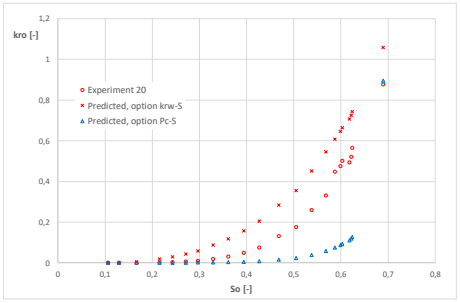	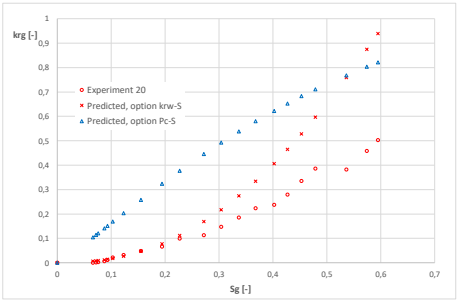
(a) Option kr-S : RMSE= 0	(b) Option kr-S : RMSE=0.029328; CRM=-0.509	(c) Option kr-S : RMSE=0.037443; CRM=-0.663
Option Pc-S : RMSE=2.95E-07	Option Pc-S : RMSE=0.048195; CRM=0.665	Option Pc-S : RMSE=0.058860; CRM=-1.562

Fig. F9. Relative permeabilities measured from Oak's DDI Experiment 20 compared to those predicted (using option kr-S and option Pc-S): (a) water relative permeability versus water saturation, (b) oil relative permeability versus oil saturation, and (c) gas relative permeability versus gas saturation. The goodness of the prediction of the measured k_r values is indicated by the root mean square error (RMSE) and the coefficient of residual mass (CRM).

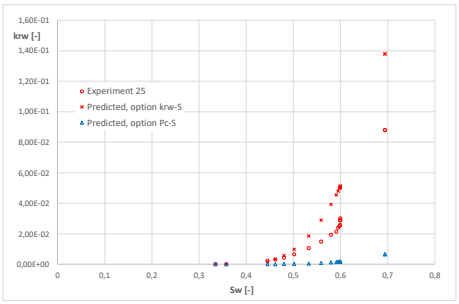	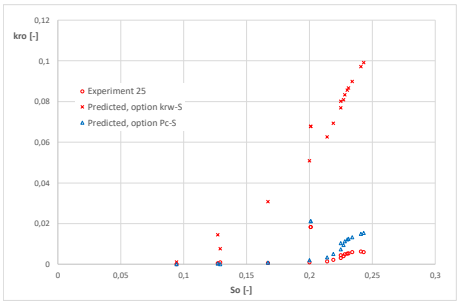	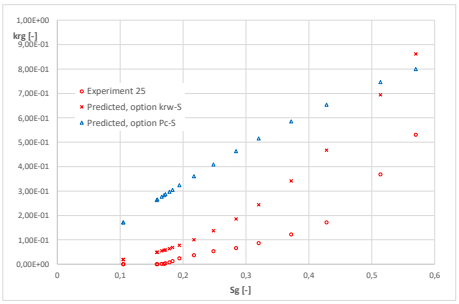
(a) Option kr-S : RMSE=0.005394; CRM=-0.732	(b) Option kr-S : RMSE=0.015422; CRM=-12.024	(c) Option kr-S : RMSE=0.036230; CRM=-1.383
Option Pc-S : RMSE=0.007509; CRM=0.933	Option Pc-S : RMSE=0.001209; CRM=-0.821	Option Pc-S : RMSE=0.077116; CRM=-3.816

Fig. F10. Relative permeabilities measured from Oak's DDI Experiment 25 compared to those predicted (using option kr-S and option Pc-S): (a) water relative permeability versus water saturation, (b) oil relative permeability versus oil saturation, and (c) gas relative permeability versus gas saturation. The goodness of the prediction of the measured k_r values is indicated by the root mean square error (RMSE) and the coefficient of residual mass (CRM).

Appendix G. Study of the occurrence of elliptic zones

G.1 Basic equations

The three-phase flow of immiscible phases is describe using the Darcy-Muskat law for the velocity of phase α:

$$v_\alpha = -\frac{Kk_{r\alpha}}{\mu_\alpha}(\nabla P_\alpha - \rho_\alpha \boldsymbol{g}) \qquad \text{(G1)}$$

where K is the absolute permeability [L^2], P_α is the pressure of the phase α [MLT^{-2}], ρ_α is the density [ML^{-3}], μ is the dynamic viscosity [MLT^{-1}], $\boldsymbol{g}$ [$L.T^{-2}$]is the gravity vector and $k_{r\alpha}$ is the relative permeability [-].

Conservation equations for an incompressible, immiscible three-phase flow can be written in terms of two saturation equations for water (α =1) and gas phases (α =3):

$$\partial_{t_D} S_\alpha + \partial_{z_D} f_\alpha = 0 \text{ with } \alpha = 1,3, \qquad \text{(G2)}$$

where S_α is the saturation of phase α, f_α is the fractional flow of phase α, z_D and t_D are the dimensionless distance and time, respectively such as:

$$z_D = z/L \quad and \quad t_D = \int_0^t \frac{v_{tot}}{\phi L} dt \qquad \text{(G3)}$$

where z is the depth [L], L the total length of the system [L], ϕ is the porosity [-] and $v_{tot} = v_1 + v_2 + v_3$ is the total volumetric flow rate of all three phases [LT^{-1}].

G.2 Linearized fractional flow equations for saturation

In the case of zero capillary pressure, the dimensionless system of saturation yields fractional flow functions of water and gaz, f_1, f_3, respectively:

$$f_1 = \frac{\lambda_1}{\lambda_t}(1 - \mathcal{N}_G((\rho_D - 1)k_{r2} + \rho_D \frac{\mu_2}{\mu_3} k_{r3})), \qquad \text{(G4)}$$

$$f_3 = \frac{\lambda_3}{\lambda_t}(1 + \mathcal{N}_G(\rho_D \frac{\mu_2}{\mu_1} k_{r1} + k_{r2})), \qquad \text{(G5)}$$

with the gravity number $\mathcal{N}_G = \frac{K(\rho_2 - \rho_3)g}{\mu_2 v_{tot}}$, $\rho_D = \frac{\rho_1 - \rho_3}{\rho_2 - \rho_3}$ is the density ratio, λ_α [$M^{-1}L^{-1}T$] is the phase mobility and λ_t [$M^{-1}L^{-1}T$] is the total mobility defined as

$\lambda_t = \sum_\alpha k_{r\alpha} / \mu_\alpha$.

The dimensionless system is linearized in terms of two saturation gradients involving a Jacobian matrix J as follows:

$$\partial_{t_D} S_{1,3} + J \nabla_{z_D} S_{1,3} = 0 \text{ with } J = \begin{pmatrix} \frac{\partial f_1}{\partial s_1} & \frac{\partial f_1}{\partial s_3} \\ \frac{\partial f_3}{\partial s_1} & \frac{\partial f_3}{\partial s_3} \end{pmatrix}. \qquad \text{(G6)}$$

From a numerical point of view, solutions of the following Riemann problem at $t_D = 0$:

$$\begin{aligned} z_D \le 0 \quad & (S_1 = S_1^L \ ; \ S_3 = S_3^L) \\ z_D > 0 \quad & (S_1 = S_1^R \ ; \ S_3 = S_3^R) \end{aligned} \qquad \text{(G7)}$$

depend on a dimensionless wave velocity $u_D = \frac{z_D}{t_D}$ yielding rarefaction and sock patterns which are the eigenvalues $u_D^\pm$ of the Jacobian matrix J :

$$u_D^\pm = \frac{1}{2}\left[\frac{\partial f_1}{\partial s_1} + \frac{\partial f_3}{\partial s_3} \pm \sqrt{\left(\frac{\partial f_1}{\partial s_1} - \frac{\partial f_3}{\partial s_3}\right)^2 + 4\frac{\partial f_1}{\partial s_3}\frac{\partial f_3}{\partial s_1}}\right] \qquad \text{(G8)}$$

with the corresponding partial derivatives of fractional flow functions f_1:

$$\frac{\partial f_1}{\partial s_{1,3}} = \frac{1}{\mu_1\mu_2\mu_3\lambda_t^2 v_{tot}}\left(-\frac{\partial \lambda_t}{\partial s_{1,3}}(\mu_2\mu_3 k_{r1} v_{tot} + gK[\mu_2 k_{r1}k_{r3}(\rho_3-\rho_1) + \mu_3 k_{r1}k_{r2}(\rho_2-\rho_1)]\right.$$
$$+\frac{\partial k_{r1}}{\partial s_{1,3}}(\mu_2\mu_3\lambda_t v_{tot} + gK[\mu_2 k_{r3}\lambda_t(\rho_3-\rho_1) + \mu_3 k_{r2}\lambda_t(\rho_2-\rho_1)])$$
$$\left.+\frac{\partial k_{r2}}{\partial s_{1,3}} gK[\mu_3 k_{r1}\lambda_t(\rho_2-\rho_1)] + \frac{\partial k_{r3}}{\partial s_{1,3}} gK[\mu_2 k_{r1}\lambda_t(\rho_3-\rho_1)]\right) \quad \text{(G9)}$$

and f_3:

$$\frac{\partial f_3}{\partial s_{1,3}} = \frac{1}{\mu_1\mu_2\mu_3\lambda_t^2 v_{tot}}\left(-\frac{\partial \lambda_t}{\partial s_{1,3}}(\mu_1\mu_2 k_{r3} v_{tot} + gK[\mu_1 k_{r2}k_{r3}(\rho_2-\rho_3) + \mu_2 k_{r1}k_{r3}(\rho_1-\rho_3)]\right.$$
$$+\frac{\partial k_{r3}}{\partial s_{1,3}}(\mu_1\mu_2\lambda_t v_{tot} + gK[\mu_1 k_{r2}\lambda_t(\rho_2-\rho_3) + \mu_2 k_{r1}\lambda_t(\rho_1-\rho_3)])$$
$$\left.+\frac{\partial kr_2}{\partial s_{1,3}} gK[\mu_1 k_{r3}\lambda_t(\rho_2-\rho_3)] + \frac{\partial k_{r1}}{\partial s_{1,3}} gK[\mu_2 k_{r3}\lambda_t(\rho_1-\rho_3)]\right) \quad \text{(G10)}$$

where $\frac{\partial \lambda_t}{\partial s_{1,3}} = \sum_\alpha \frac{1}{\mu_\alpha}\frac{\partial k_{r\alpha}}{\partial s_{1,3}}$.

When the eigenvalues $u_D^{\pm}$ are real and distinct, the system (G6) is hyperbolic. In this case, there are two real eigenvectors $\overrightarrow{v_D^{\pm}}(v_{D,1}^{\pm}, v_{D,3}^{\pm})$ that correspond to the direction of admissible changes in fluid saturation and identify so-called fast and slow rarefaction curves. The components of the eigenvectors are expressed as

$$v_{D,1}^{\pm} = dS_1 = \frac{\partial f_1}{\partial S_3} \;\; ; \; v_{D,3}^{\pm} = dS_3 = u_D^{\pm} - \frac{\partial f_1}{\partial S_1} \quad \text{(G11)}$$

The fast rarefaction characterized by the eigenvector $\overrightarrow{v_D^{+}}$ represents situations in which gas or/and water saturations increase in three-phase systems (Jackson and Blunt, 2002).

When Eq. (G8) gives a real wave velocity, some values of saturations called *umbilic point* (Jackson and Blunt, 2002) give the same value: $u_D^{\pm} = u_D^{+} = u_D^{-}$. The resulting system is therefore non-strictly hyperbolic and very sensitive to the initial condition (Isaacson et al., 1990). The square root in Eq. (G8) is then always positive. In the elliptic region, wherein $u_D^{\pm}$ are complex and conjugates, a linearized analysis shows that the system is unstable (e.g., Jahanbakhsi et al. (2013), Bell et al. (1986)). In the presence of capillarity, the diffusive term becomes dominant at high frequencies. However, at low frequencies, the diffusive term would not be sufficient to remove instabilities.

It has been shown that inside the elliptic region, equilibrium formulation yields unstable and oscillatory solutions. When the initial and injected state for saturation is inside the elliptic region, the solution exhibits oscillatory behavior, growing in magnitude showing that the system is unstable (Trangenstein, 1989). A non-equilibrium approach was developed (Jahanbakhsi et al., 2013) using relaxation strategies (Barenblatt's model) which leads to high order terms involving cross derivatives. When both, S_L and S_R are outside the elliptic region, the solution is stable and the existence of the elliptic zone does not affect the results. When initial and injected states are on the opposite sides of the elliptic region, solutions are oscillatory and not completely stabilized.

G.3 Test of implemented algorithm to identify elliptic zones : the study case of Bell

In order to investigate three-phase relative permeability behavior on ternary diagram $\mathbb{T}$, a first set of functions is used from Bell (1986):

$$k_{r1}(s_1) = 1.09 s_1^{1.516687} - 0.09 s_1^{4.51668}$$

$$k_{r2}(s_1, s_3) = \frac{1 - s_1 - s_3}{(1 - s_1)(1 - s_3)} k_{r12}(s_1) k_{r23}(s_3)$$

$$k_{r3}(s_3) = 0.525 s_3^{1.02} + 0.475 s_3^{3.62} \quad \text{(G12)}$$

To quantify the three-phase oil relative permeability (kr_2), the two-phase relative permeability functions k_{r12} and k_{r23} from the water/oil and oil/gas side are expressed by :

$$k_{r12}(s_1) = 1.95(1 - s_1)^{8.28} - 0.95(1 - s_1)^{11.284}$$

$$k_{r23}(s_3) = 1.19(1 - s_3)^{2.006} - 0.19(1 - s_3)^{2.024} \quad \text{(G13)}$$

Bell's model is a synthetic set of relative permeabilities known to maximize the elliptic region on $\mathbb{T}$. Water viscosity is μ_1=0.8 cP, gas viscosity is μ_3=0.05 cP and three different oil viscosities are investigated from 0.1 cP to 5 cP without gravity effect (Fig. G1).

(a) Jahanbakhshi et al. (2013)	(b) Our study
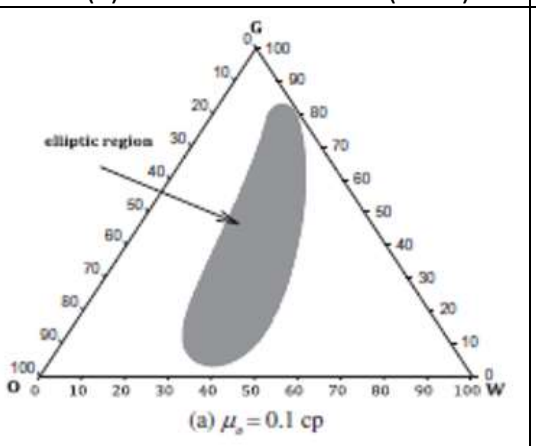	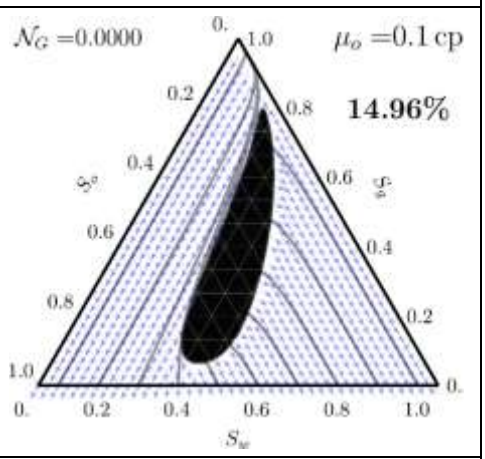
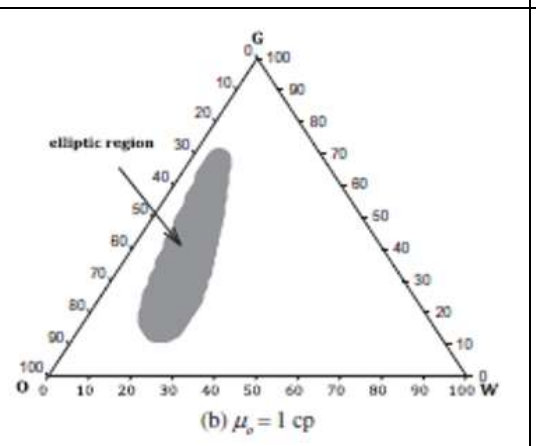	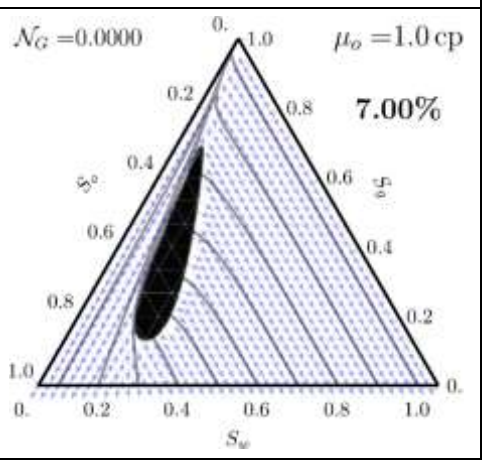
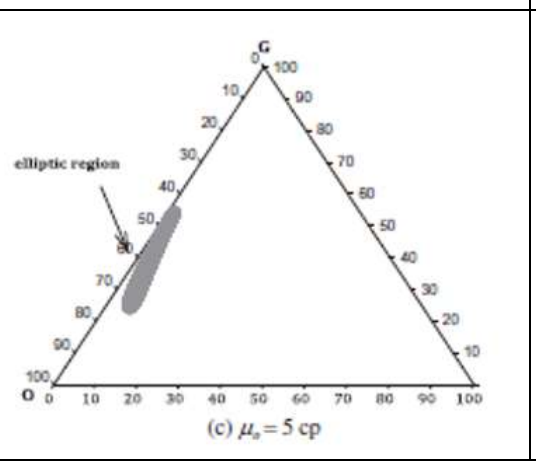	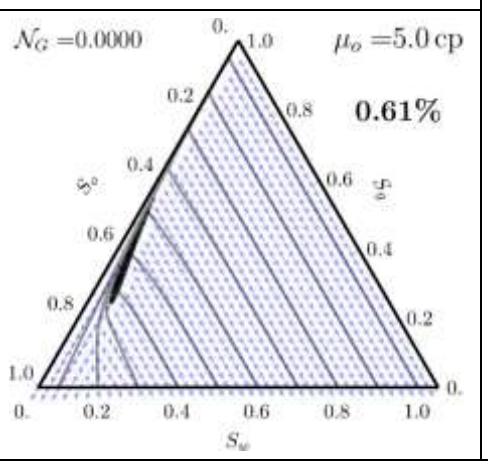

Fig. G1. Comparison of elliptic zones without gravity using Bell's model and 3 different oil viscosities documented by Jahanbakhshi et al. (2013) and quantified with the search algorithm used in our study. Elliptic regions are depicted as the black areas. The results of our study show the percentage of saturation space covered by elliptic regions, the distribution of eigenvectors associated with fast rarefaction waves (blue arrows) and the curves in the hyperbolic part are solution paths corresponding to the eigenvalues u_D^+

(grey lines).

When reducing the oil viscosity from 5 cP to 0.1 cP, the elliptic region produces a larger instability area. The largest zone for μ_2=0.1 cP almost occupies 15% of the whole ternary surface, parallelly oriented to the gas-oil side compared to 7% obtained for $\mu_2 = 1$ cP. The lower the oil viscosity is the larger the extent of the elliptic area.

When including gravity, another elliptic region appears whose extent strongly depend on the absolute value of total velocity. Fig. G2 shows the influence of gravity associated with different orders of magnitude of total velocity, varying from 10^{-2} ms^{-1} to 10^{-7} ms^{-1}. As reference is used here the case without gravity and a fixed oil viscosity fixed of 1 cp. When the total velocity is 10^{-2} ms^{-1}, the elliptic zone decreases slightly while its area remains close to 7% of the total ternary surface. The further decrease of the total velocity results in a significant decrease of the elliptic area to about 2% of the total ternary surface and a displacement of the elliptic zone towards the oil vertex. Overly, the decrease of total velocity has a stabilizing and antagonistic effect in contrast to the oil viscosity. However, both parameters appear in the denominator of the gravity number $\mathcal{N}_G$ (Eqs. (G4) and (G5)).

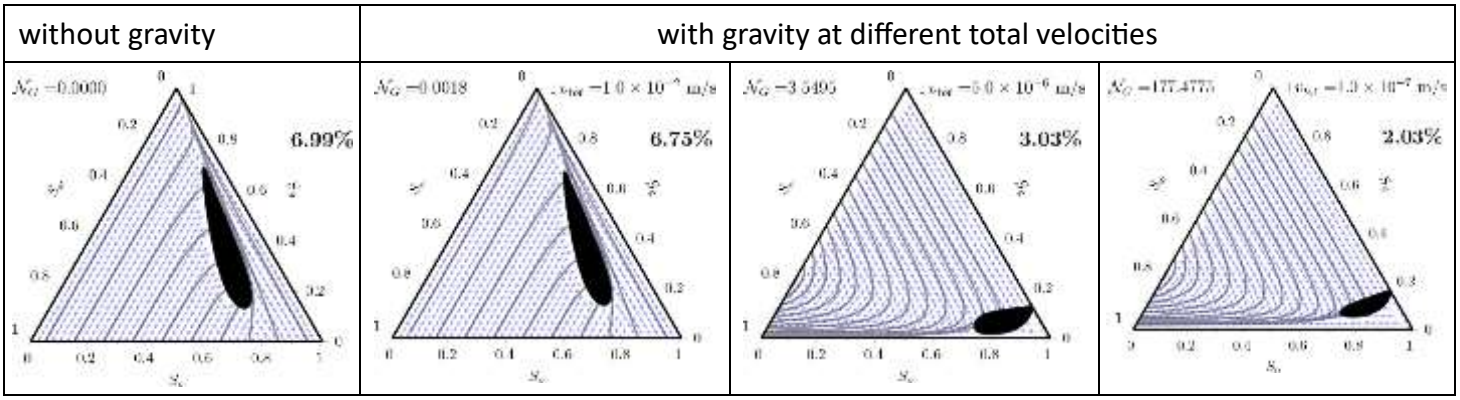

Fig. G2. Extent of elliptic zones with Bell's synthetic model using an oil viscosity of 1 cp: study case without gravity (left) and with gravity effect and different total velocities (right). $\mathcal{N}_G$ is the dimensionless gravity number. Elliptic regions are depicted as the black areas. The results of our study show the percentage of saturation space covered by elliptic regions, the distribution of eigenvectors associated with fast rarefaction waves (blue arrows) and the curves in the hyperbolic part are solution paths corresponding to the eigenvalues u_D^+ (grey lines).

G.4 Parker-Lenhard model: quantification of elliptic regions

The occurrence of elliptic regions was assessed for the Parker-Lenhard model in the same way as described for the mechanistic model. The numerical results obtained for the Bentheimer sandstone and Berea sandstone are described below.

G.4.1 Bentheimer sandstone

The study on the occurrence of elliptic regions was conducted with the Parker-Lenhard model using the experimental data of the Bentheimer sandstone (Table 2), the intrinsic permeability of the rock $K = 2.63 \times 10^{-12}$ m^2 and the model input parameter of modeling options Pc-S and kr-S (Table 9). The numerical results obtained are shown in Fig. G3.

without gravity	with gravity at different total velocities		
Option Pc-S	Option Pc-S		
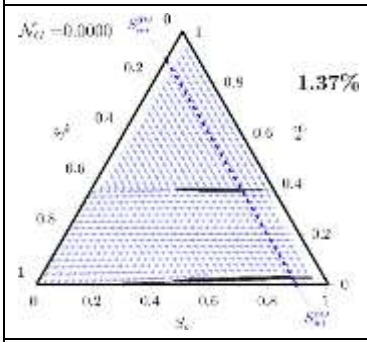	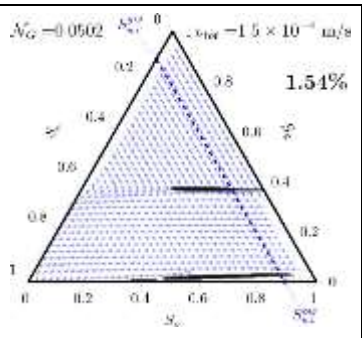	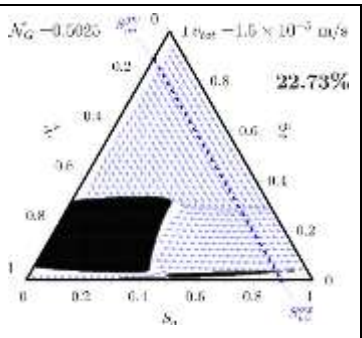	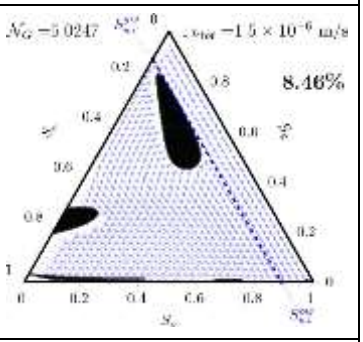
Option kr-S	Option kr-S		
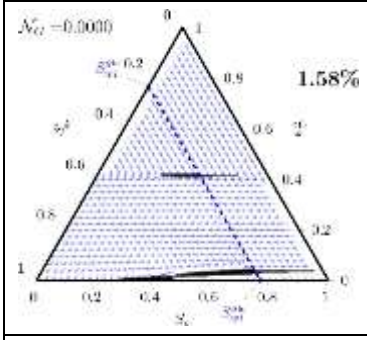	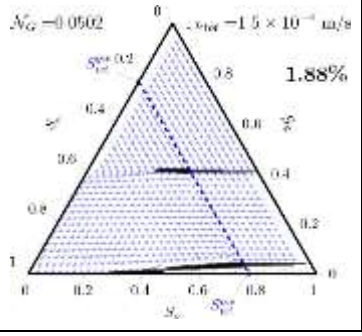	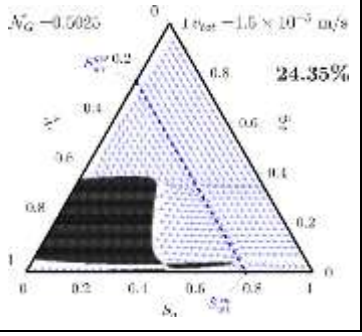	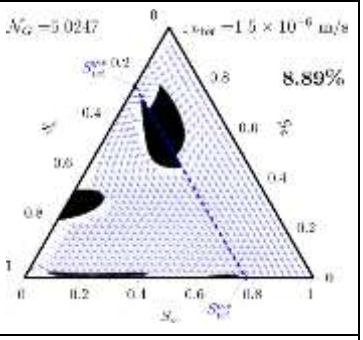

Fig. G3. Bentheimer sandstone: influence of gravity and total velocity on the extent of elliptic regions in the ternary diagram. $\mathcal{N}_G$ is the dimensionless gravity number. The results show the percentage of saturation space covered by elliptic regions and the distribution of eigenvectors associated with fast rarefaction waves (blue arrows). Elliptic regions are depicted as the black areas. The dotted blue lines indicate the limits of irreducible water saturation.

G.4.2 Berea sandstone

The study on the occurrence of elliptic regions was conducted with the Parker-Lenhard model using the experimental data of the Berea sandstone (Table 3), the intrinsic permeability of the rock $K = 1.97 \times 10^{-13}$ m^2 and the model input parameter of modeling options Pc-S and kr-S (Table 9). The numerical results obtained are shown in Fig. G4.

without gravity	with gravity at different total velocities		
Option Pc-S	Option Pc-S		
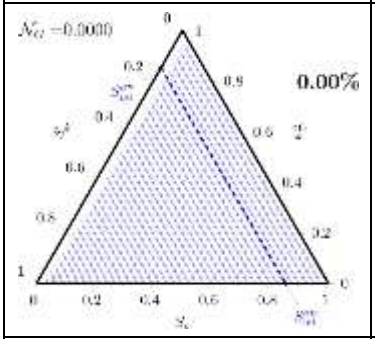	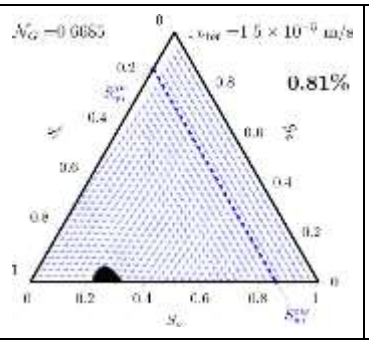	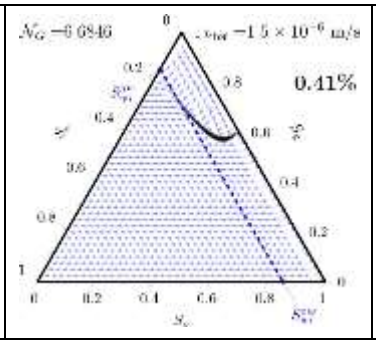	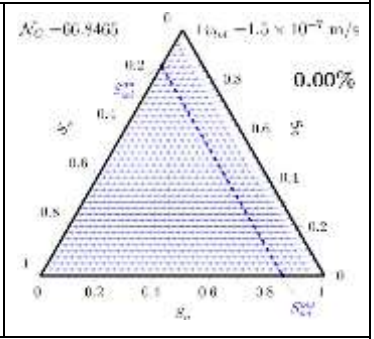
Option kr-S	Option kr-S		
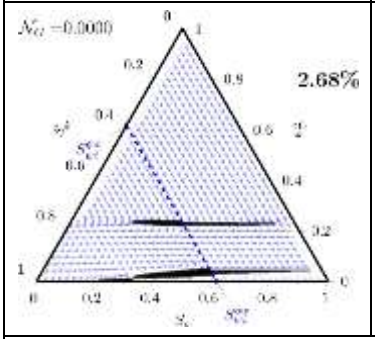	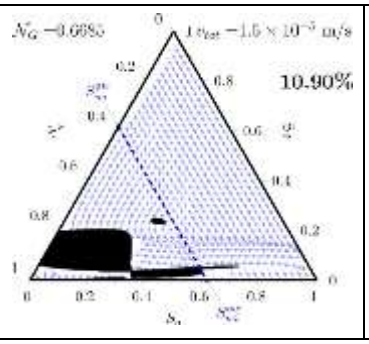	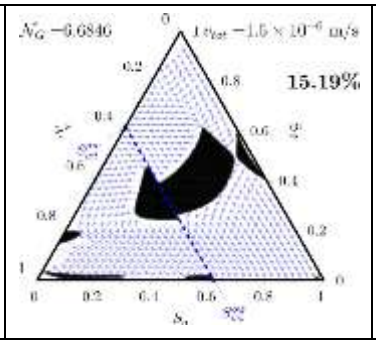	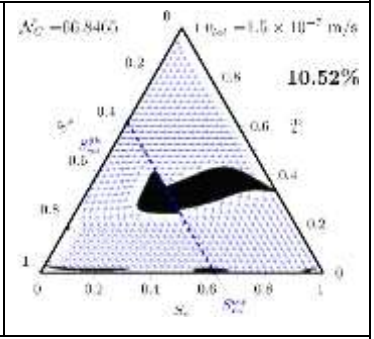

Fig. G4. Berea sandstone: influence of gravity and total velocity on the extent of elliptic regions in the ternary diagram. $\mathcal{N}_G$ is the dimensionless gravity number. The results show the percentage of saturation space covered by elliptic regions and the distribution of eigenvectors associated with fast rarefaction waves (blue arrows). Elliptic regions are depicted as the black areas. The dotted blue lines indicate the limits of irreducible water saturation.

G.5 Stone's model I: quantification of elliptic zones

The occurrence of elliptic regions was assessed for the Stone's model I in the same way as described for the mechanistic model. The numerical results obtained for the Bentheimer sandstone and Berea sandstone are presented below. To study the existence of possible elliptic regions, we required a relative permeability model for water and gas in the water-oil-gas saturation space. We therefore used the water relative permeability and gas relative permeability expression described by the Lenhard-Parker model (Eqs. (5) and (7)). The Van Genuchten parameter m and the irreducible water saturation in a water-gas system Swi was adopted from modeling option Pc-S (Table 9).

G.5.1 Bentheimer sandstone

The study on the occurrence of elliptic regions was conducted with Stone's model I using the experimental data of the Bentheimer sandstone (Table 2), the intrinsic permeability of the rock $K = 2.63 \times 10^{-12}$ m^2, and the model input parameter used for the prediction of DDI experiments performed on Bentheimer sandstone (Table 10).

The numerical results obtained are shown in Fig. G5.

without gravity	with gravity at different total velocities		
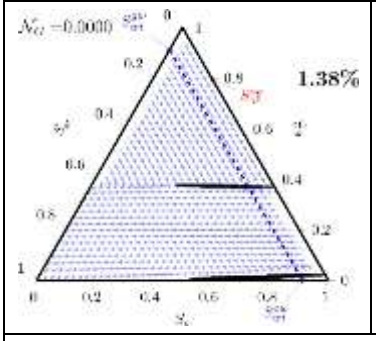	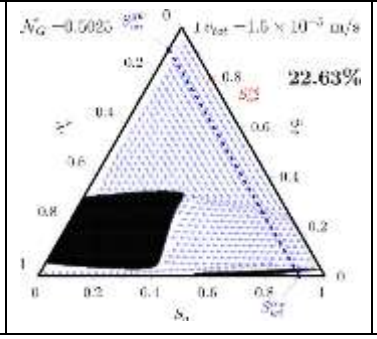	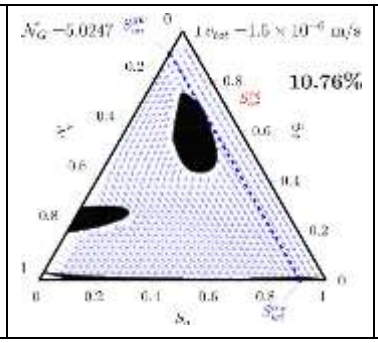	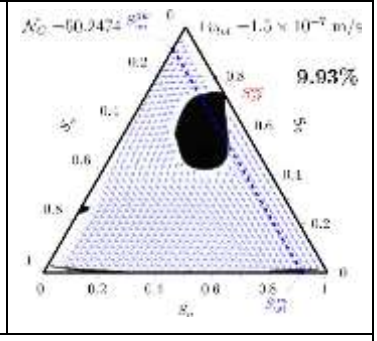

Fig. G5. Bentheimer sandstone: influence of gravity and total velocity on the extent of elliptic regions in the ternary diagram. $\mathcal{N}_G$ is the dimensionless gravity number. The results show the percentage of saturation space covered by elliptic regions and the distribution of eigenvectors associated with fast rarefaction waves (blue arrows). Elliptic regions are depicted as the black areas. The dotted blue lines indicate the limits of irreducible water saturation.

G.5.2 Berea sandstone

The study on the occurrence of elliptic regions was conducted with Stone's model I using the experimental data of the Berea sandstone (Table 3), the intrinsic permeability of the rock $K = 1.97 \times 10^{-13}$ m^2 and the model input parameter used for the prediction of DDI experiments performed on Berea sandstone (Table 10). The numerical results obtained are shown in Fig. G6.

without gravity	with gravity at different total velocities		
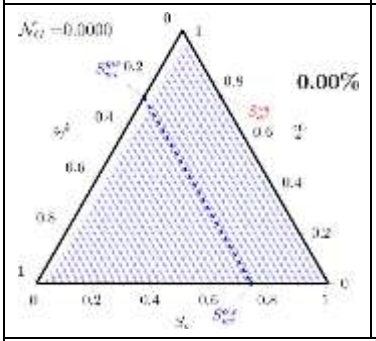	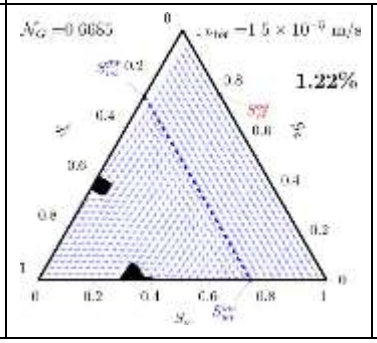	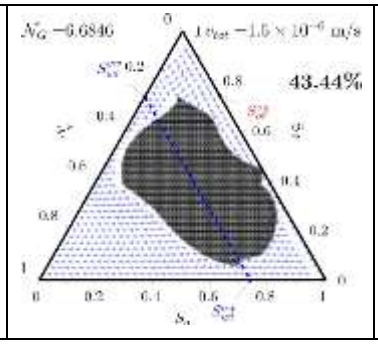	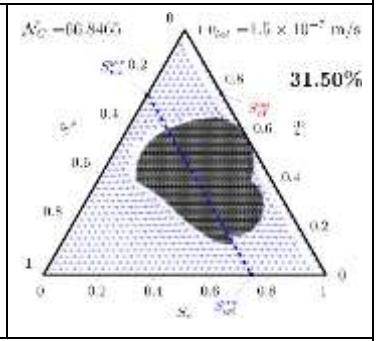

Fig. G6. Berea sandstone: influence of gravity and total velocity on the extent of elliptic regions in the ternary diagram. $\mathcal{N}_G$ is the dimensionless gravity number. The results show the percentage of saturation space covered by elliptic regions and the distribution of eigenvectors associated with fast rarefaction waves (blue arrows). Elliptic regions are depicted as the black areas. The dotted blue lines indicate the limits of irreducible water saturation.